INFLUENCE OF PRE-EXISTING STRIKE-SLIP FAULTS ON FAULT DEVELOPMENT DURING A SUBSEQUENT PHASE OF EXTENSION

By

CHRISTIAN SATRIANTA PUTRA GINTING

A thesis submitted to the

Graduate School-New Brunswick

Rutgers, The State University of New Jersey

in partial fulfillment of requirements

for the degree of

Master of Science

Graduate Program in Geological Sciences

written under the direction of

Dr. Martha Oliver Withjack

Dr. Roy W. Schlische

and approved by

_____

_____

_____

New Brunswick, New Jersey

October, 2013

ABSTRACT OF THE THESIS

Influence of Pre-Existing Strike-Slip Faults on Fault Development During a Subsequent Phase of Extension

By Christian Putra

Thesis Directors:

Dr. Martha Oliver Withjack

Dr. Roy W. Schlische

The goal of this study is to investigate how high-angle strike-slip faults affect deformation patterns during a subsequent phase of extension. To accomplish this goal, I use scaled experimental (analog) models with wet clay and two phases of deformation, an initial strike-slip phase and subsequent extensional phase. In Series 1 models, the extension direction varies during the second phase. In Series 2 models, the degree of the strike-slip-fault development varies during the first phase. The first-phase, right-lateral strike-slip deformation consists of subvertical Riedel shears, right-lateral R-shears and left-lateral R'-shears that strike ~15° and ~85°, respectively, relative to the trend of the deformation zone. In Series 1 models, the maximum extension direction relative to the strike of the pre-existing R- and R'-shears controls the likelihood of reactivation, the sense of slip on the reactivated faults, and the orientation of new normal faults. Pre-existing faults that are closer to being subperpendicular to the extension direction are more likely to be reactivated as high-angle normal faults. Additionally, some of the pre-existing R-shears are reactivated as tension gashes. Pre-existing faults that are closer to

being subparallel to the extension direction are more likely to be reactivated as oblique-slip/strike-slip faults. Series 2 models show that new faults increasingly become more parallel to the orientation of R-shears as the pre-existing R-shears become better developed. In both Series 1 and 2 models, new faults commonly interact with pre-existing faults by cutting across, initiating at, and/or intersecting them. A pre-existing high-angle fault population can inhibit the development of new faults. A layered model shows that more faults cut the bottom of the clay than cut the top of the clay, suggesting that many faults nucleate at the base of the clay and propagate upward to the top of the clay. The reactivation of the pre-existing high-angle faults during a subsequent episode of extension and the interactions between pre-existing high-angle faults and new faults are comparable to those observed in the Suez rift system.

ACKNOWLEDGMENTS

I would like to express my gratitude to my advisors, Martha Oliver Withjack and Roy W. Schlische, for their full support both technically and mentally since the beginning of my life in graduate school. I would like to thank Karen Bemis for insightful discussions and conversations. This research would not be possible without the help of the work-study students (especially Jason, Sean, Christina, Hinal, and Bianca) who assisted me during most of laboratory experiments. I thank all the Earth and Planetary Sciences faculty and staff for their friendliness and assistance. I would also like to thank all my friends at Rutgers University in particular, all my friends in Highland Park, New Brunswick, Princeton, Manhattan, Brooklyn, Queens, and people I met all over this country in general. Thank you for all stories we have created and the life we have shared. I really appreciate ExxonMobil Oil Indonesia for giving me the opportunity to do this research at Rutgers University.

Table of Contents

LIST OF TABLES

LIST OF FIGURES

1. INTRODUCTION

Several experimental modeling studies have investigated the reactivation of gently dipping reverse faults during extension (negative inversion) and the reactivation of moderately dipping normal faults during subsequent extension (e.g., Faccenna et al., 1994; Eisenstadt and Withjack, 1995; Henza et al., 2010, 2011). However, no previous modeling studies have investigated whether very high-angle faults are reactivated during subsequent extension.

Field studies in rift basins suggest that, in some cases, high-angle faults are reactivated and influence the development of new normal faults. For example, in the Suez rift, McClay and Khalil (1998) and Younes and McClay (2002) infer that pre-existing strike-slip shear zones are reactivated during rifting (Fig. 1). Specifically, the pre-existing zones of weakness that strike subperpendicular and highly oblique to the extension direction are reactivated during rifting as normal faults and/or oblique-slip faults.

This study uses experimental models to study the reactivation of pre-existing, high-angle faults during a subsequent phase of extension and to address several critical questions:

1. What stress states (i.e., σ_1 vertical and σ_1 horizontal) promote the reactivation of steeply dipping faults?
2. What is the style of reactivation?
3. Are pre-existing faults sites of nucleation of new normal faults? Alternatively, do they inhibit the propagation of new normal faults?
4. How do the second-phase fault patterns in models with a pre-existing fault population compare to those in models without a pre-existing fault population?

5. How does the degree of development of the pre-existing fault population affect deformation patterns during the subsequent phase of extension?

I address these questions by running two series of scaled experimental (analog) models. In all models, high-angle, strike-slip faults develop during the first phase of deformation. In Series 1 models, the extension direction varies during the second phase. In Series 2 models, the magnitude of the first-phase displacement/strain varies, leading to a variation in the degree of development of strike-slip faults.

2. EXPERIMENTAL APPROACH

2.1. Modeling Materials

In experimental modeling, wet clay and dry sand are the most common modeling materials because the deformation patterns produced by these materials are similar to those in nature (e.g., Eisenstadt and Withjack, 1995; Withjack et al., 2007). I select wet clay as the modeling material for two main reasons: 1) faults in wet clay are more likely to be reactivated than those in dry sand (Eisenstadt and Sims, 2005) and 2) compared to dry sand, the ductility of wet clay allows a more detailed view of fault interactions and development.

In the experiments in this study, a homogenous layer of wet clay overlies a layer of silicone polymer. The wet clay is similar to that used in previous experimental modeling studies (e.g., Clifton et al., 2000; Schlische et al., 2002; Eisenstadt and Sims, 2005; Withjack and Schlische, 2006; Henza et al., 2010). It consists of kaolinite and approximately 40% water by weight (Withjack and Callaway, 2000). Its particle size is less than 0.005 mm (Withjack et al., 2007), and its density is ~1.65 g cm^{-3}, depending on

the water content (Sims, 1993; Eisenstadt and Sims, 2005). The coefficient of internal friction of wet clay is approximately 0.6, and its angle of internal friction is approximately 30° (e.g., Eisenstadt and Sims, 2005). The PDMS (polydimethysiloxane) silicone polymer serves to decouple the clay from the base of the apparatus, distributing the deformation; it also allows the base of the clay layer to move vertically. The density of the silicone polymer is ~1 g/cm^3 and its viscosity is ~10^4-10^5 Pa s (Weijermars, 1986).

2.2. Scaling

Wet clay has mechanical properties that allow geometric and dynamic similarity with natural structures (Vendeville et al., 1995; Withjack and Callaway, 2000; Eisenstadt and Sims, 2005; Withjack and Schlische, 2006; Withjack et al., 2007). It satisfies the dynamic similarity between the models and natural prototypes by fulfilling two conditions (e.g., Withjack and Jamison, 1986; Withjack and Callaway, 2000; Schlische et al., 2002; Henza et al., 2010). First, the coefficient of internal friction of wet clay and that of the natural prototype (i.e., rock) is similar (~0.6 for wet clay vs. 0.55 to 0.85 for sedimentary rocks; e.g., Handin, 1966; Byerlee, 1978). Second, wet clay obeys the scaling relationship:

$$C^* = \rho^* \bullet L^* \bullet g^* \qquad (1)$$

in which C^*, ρ^*, L^*, and g^* are the model to nature ratios of cohesion, density, length, and gravity, respectively. The value of ρ^* in the models is 0.7 and g^* is 1. Therefore, the cohesive strength of the wet clay and the dimensions of the model must scale by the same factor relative to those parameters of the natural prototype. The cohesive strength of wet clay (54-130 Pa; Eisenstadt and Sims, 2005) is 10^4 to 10^5 times less than that of

sedimentary rocks (~1 to 10 MPa; Handin, 1966). Thus, 1 cm in our models is equivalent to 100-1000 m in nature.

2.3. Experimental Setup

The modeling apparatus consists of two basal plates: a fixed plate overlapping a mobile plate (Fig. 2). A layer of silicone polymer, 18 cm wide and 51 cm long, overlies the two plates; the polymer is 0.9 cm thick above the fixed plate and 0.6 cm thick above the mobile plate. A single layer of wet clay, up to 4 cm thick, 61 cm wide, and 61 cm long overlies the two overlapping plates and silicone polymer (Fig. 2b). To study the geometry of faults in cross section, I also prepared a model with multi-colored layers, each with identical mechanical properties.

Most models have two phases of deformation (Table 1). During the strike-slip phase (1^{st} phase), the mobile plate moves at a rate of 4 cm h^{-1} in a right-lateral sense (Fig. 2c). In the Series 1 models, the total displacement is 5 cm, and in the Series 2 models, the displacement ranges from 0 to 5 cm. During the second phase of deformation, the mobile plate moves away from basal fixed plate with various displacement directions for a total of 5 cm (Series 2; Figs. 2c and 3). The displacement direction is given by α, which is the angle measured clockwise from the trend of the deformation zone and the displacement direction of the mobile plate (Withjack and Jamison, 1986). During the second phase, α ranges from 30° to 150°. I also prepared single-phase models without an initial strike-slip phase of deformation for comparison with the two-phase models of Series 1.

2.4. Model Analysis

Photographs of the top surface of the model (taken every 0.1 cm with multiple lighting directions) document deformation through time during the first phase (strike-slip) and second phase (extension) of deformation. (Fig. 4) To avoid edge effects, I analyzed an area in the central part of the model. During the strike-slip phase of deformation, displacement of superficial markers on the top surface, the presence of push-up and pull-apart structures between en-echélon fault segments, and the presence of releasing structures at fault terminations (e.g., horsetail splays) indicate the sense of slip on faults. During the second phase of deformation, fault scarps indicate the dip direction of the faults. I fit fault segments with straight lines to record all fault-segment orientations at the end of each phase of deformation (Fig. 4). Fitting lines to fault segments results in several distinct segments with several distinct orientations, whereas a tip-to-tip line yields one fault with one orientation. Several previous studies also used the fault segmentation method of analysis (e.g., Withjack and Jamison, 1986; Schlische et al., 2002; Henza et al., 2010, 2011).

3. EXPERIMENTAL OBSERVATIONS

3.1. Series 1: Two-Phase Models with Variable Directions of Second-Phase Extension

3.1.1. Strike-slip phase of deformation

During the strike-slip phase of deformation (1st phase), the basal mobile plate moves in a right-lateral sense relative to the fixed plate. In all experiments, a long zone of deformation (approximately 61 cm by 10 cm) develops above the silicone polymer and

the overlapping plates (Fig. 5). The observable deformation occurs only in a narrow zone directly above the edge of the upper plate. The deformation consists of two sets of faults, both with en-échelon segments. In one set, fault segments strike 10°-20° clockwise relative to the long axis of the deformation zone (NNE-striking fault segments). In the second set, fault segments strike 80°-90° clockwise relative to the long axis of the deformation zone (E-striking fault segments). Thus, the angle between the two fault sets is approximately 70°.

Offsets of superficial markers on the top of the clay layer and the presence of push-up and pull-apart structures between en-echélon fault segments allow the determination of the sense-of-slip on the faults using the geometries shows in Fig. 6. The NNE-striking fault segments offset superficial markers with right-lateral separation, whereas the E-striking fault segments offset them with left-lateral separation (Fig. 7a). Pull-apart structures develop between NNE-striking, right-stepping fault segments, whereas push-up structures develop between NNE-striking, left-stepping fault segments. Thus, the NNE-striking faults have right-lateral strike-slip (Fig. 7a). Push-up structures also form between E-striking, right-stepping fault segments, whereas pull-apart structures develop between E-striking, left-stepping fault segments. Thus, the E-striking faults have left-lateral strike-slip (Fig. 7b). These conjugate fault sets are known as Riedel shears (Cloos, 1928; Riedel, 1929; Tchalenko, 1970; Sylvester, 1988) and belong to two categories (according to their sense of movement relative to the movement of basal mobile plate): synthetic (right-lateral) R-shears (NNE-striking faults) and antithetic (left-lateral) R'-shears (E-striking faults).

Figure 8 shows the evolution of the Riedel shears in the models. Generally, both sets of faults first appear by 3.8 cm of displacement of the basal mobile plate. In Model C and Model I, however, the R- and R'-shears form at higher displacements (~4.2 cm). With increasing displacement, the R-shears link with other R-shears (Fig. 7a). Some of them cut the R'-shears with right-lateral separation. They also intersect the R'-shears. As deformation progresses, the R'-shears rotate clockwise. Rotation and offsets cause some of the R'-shears to have a curved map-view geometry (Fig. 9). Horsetail splays also develop near the terminations of some R'-shears. These are a type of releasing structure that gives information about the shear sense of the main fault (see Fig. 6).

The summed lengths of fault segments for the R- and R'-shears and the total summed lengths of all segments vary in the models, despite the identical boundary conditions (Fig. 10). Models C and G have approximately equal summed lengths of the R- and R'-shear segments. Models A, B, F, and I have greater summed lengths of the R'-shear segments relative to the R-shear segments, whereas Models D, E, and H have greater summed length of the R-shear segments relative to the R'-shear segments. Despite this heterogeneity, the rose diagrams (Fig. 10) display a similarity in the orientations of the R- and R'-shears in all models: 10° to 20° for the R-shears and 80° to 90° for the R'-shears.

3.1.2. Second phase of deformation

In all models, the observable deformation during the second phase occurs in a zone above the silicone polymer. The deformed zone is wider than that for the strike-slip phase of deformation (~15 cm to 24 cm for the second phase of deformation vs. ~10 cm

for the first phase). The strike-slip fault zone moves either toward the northeast, east, or southeast, depending on the displacement direction. Numerous new faults form in all models during the second phase of deformation. They initially form as isolated segments that subsequently propagate toward each other and link together. In general, the pre-existing R- and R'-shears influence the distribution of the new faults. Where the pre-existing fault population is less developed (i.e., above the basal fixed plate), new faults are abundant, long, and have large displacements. Where the pre-existing fault population is better developed (i.e., above the basal mobile plate), new faults are fewer, shorter, and have less displacements.

3.1.2.1. Models A and A1

In Model A (α_2=30°; ε_2=60°) (Figs. 11b and 12b), new faults first develop before ~3 cm of displacement of the moving plate (Fig. 13). Their strike is 135° to 165° clockwise relative to the long axis of the deformation zone (Fig. 11b). Some new faults nucleate at pre-existing R-shears (Fig. 15). Others are isolated (Fig. 14b). Many new faults end against pre-existing R'-shears and/or die out after cutting across them (Figs. 13 and 14). During the second phase of deformation, pre-existing R- and R'-shears move northward, following the movement of the basal mobile plate. The length of some pre-existing R-shears increases, indicating reactivation of these faults (Fig. 15). Another type of reactivation of R-shears involves changes in sense-of-slip from right-lateral to left-lateral (Fig. 16). Many R'-shears also change their orientation during the second phase of deformation; they rotate counterclockwise relative to the long axis of deformation zone (Figs. 13b to d).

In Model A1 (α=30°; ε=60°; no initial strike-slip deformation), the faults strike 130° to 160° clockwise relative to the long axis of deformation (Fig. 11c, 12c, and 17). Generally, the faults have smaller displacements than those in Model A. Model A1 has approximately the same fault distribution across the deformed zone.

3.1.2.2. Models B and B1

In Model B (α_2=45°; ε_2=67.5°) (Figs. 18b and 19b), the strike of the new faults ranges from 140° to 170° clockwise relative to the long axis of the deformation zone. Figure 20 shows the evolution of the new faults. Most new faults are isolated from pre-existing faults; these faults mostly develop in the area where the pre-existing fault population is less developed. New faults first form before ~2.7 cm of displacement of the basal mobile plate (Fig. 20). New faults that develop within the first-phase deformed zone mostly initiate at pre-existing R-shears (i.e., new faults have maximum displacement at the pre-existing faults) and propagate away from them (Fig. 21). The new faults later cut across pre-existing R'-shears and eventually die out. Reactivation of some pre-existing R-shears occurs in Model B. Some of them become more pronounced with a slightly greater dip-slip component of displacement as the experiment progresses (e.g., Fault 1 in Figs. 22g-l); other faults (e.g., Fault 3 in Figs. 22k-l), which did not reach the clay surface at the end of the strike-slip phase of deformation, propagate to the surface during the latter stages of the second phase of deformation. Some of the new faults also rotate counterclockwise (e.g., Fault 1 in Figs. 22g-l). As in Model A, many pre-existing R'-shears rotate counterclockwise and become more curved during the second phase of deformation (e.g., Fault 2 in Figs. 22g-l).

In Model B1 (α=45°; ε=67.5°; no initial strike-slip deformation) (Figs. 18c and 19c), faults first develop after 2.0 cm of displacement of the basal mobile plate (Fig. 23). The faults strike 140° to 170° clockwise relative to the long axis of deformation zone (Fig. 18c). In general, the distribution of faults in Model B1 is more uniform than new faults in Model B (Fig. 19c). The faults above the basal fixed plate have relatively similar displacements as those that develop above the basal fixed plate in Model B, but faults above the basal mobile plate have significantly higher displacements than those in Model B.

3.1.2.3. Models C and C1

In Model C (α_2=60°; ε_2=75°) (Figs. 24b and 25b), the strike of the new faults ranges from 150° to 180° clockwise relative to the long axis of the deformation zone. Generally, this model has a relatively symmetric distribution of faults across the deformed zone where the pre-existing fault population is poorly developed or is not present (Fig. 25b). Similar to Models A and B, the new faults are numerous, long, and have high displacements where the pre-existing fault population is poorly developed or does not develop but fewer, shorter, and have less displacements where the pre-existing fault population is better developed. However, new faults are also abundant above part of the basal mobile plate where pre-existing faults are not developed (Fig. 24b). Fewer faults develop above this area in Models A (Fig. 11b) and B (Fig.18b). New faults develop after ~2.5 cm (similar to Model B) (Fig. 26). The new faults that are isolated from pre-existing faults (Fig. 26) develop more rapidly and have higher displacements than those that initiate at pre-existing faults (mostly at R-shears; Fig. 27). The new faults

that initiate at pre-existing R-shears terminate against pre-existing R'-shears and/or decrease their displacement after cutting across them. Some of the pre-existing R-shears, which did not appear on the surface at the end of the first phase, propagate to the surface during the second phase of deformation, suggesting reactivation of these faults with dip-slip component (Fig. 27). Horsetail splays on R-shears also suggest reactivation with left-lateral strike-slip. The original slip sense was right lateral.

In Model C1 (α=60°; ε=75°; no initial strike-slip deformation) (Figs. 24c and 25c), faults first develop at or after 3.0 cm of displacement of the basal mobile plate (Fig. 28). The faults strike 155° to 175° clockwise relative to the long axis of deformation zone (Fig. 24c). Similar to Model C, new faults develop above both the basal fixed plate and the mobile plate (Fig. 25c). The deformed zone, however, is narrower than that in Model C (~16.8 cm in this model vs. ~20.8 cm in Model C) at the end of the second phase of deformation.

3.1.2.4. Models D and D1

In Model D (α_2=75°; ε_2=82.5°) (Figs. 29b and 30b), most of the new faults strike oblique to the extension direction (175° to 205° clockwise relative to the long axis of the deformation zone), leaving only a small number of faults whose strike resembles those of the faults in Model D1 (no initial strike-slip deformation; Fig. 29c and 30c). Similar to Model C, the new faults that are isolated from pre-existing faults develop more rapidly and have higher displacements than those that initiate at pre-existing faults. Reactivation of some pre-existing R-shears also occurs in Model D (Figs. 31 and 32). They become more pronounced with a slight dip-slip and slight left-lateral strike-slip component of

displacement during the second phase of deformation. Some pre-existing R-shears pull apart and form tension gashes.

In Model D1, faults first develop at or after 2.0 cm of displacement of the basal mobile plate (Fig. 33). They strike (160° to 180° clockwise relative to the long axis of the deformation zone) subperpendicular to the maximum extension direction and generally have higher displacements than those in Model D (Figs. 29c and 30c). The deformed zone in Model D1 is narrower than that in Model D (~18.4 cm in this model vs. ~22.4 cm in Model D) at the end of the second phase of deformation.

3.1.2.5. Models E and E1

In Model E (α_2=90°; ε_2=90°) (Figs. 34b and 35b), new faults form at relatively low values of displacement (after ~1.3 cm) (Fig. 36). Their strike is 175° to 205° clockwise relative to the long axis of the deformation zone (Fig. 34b). The strike of most faults resembles those of the pre-existing R-shears. The new faults are either isolated from pre-existing faults or initiate at pre-existing R'-shears (Fig. 37). The spatial distribution of the new faults is similar to that in Models C and D (approximately symmetrical) (Fig. 35b). The length of some pre-existing R-shears increases, indicating reactivation of these faults (Fig. 37). Other R-shears are reactivated with significantly greater dip-slip component of displacement as the experiment progresses (Fig. 38). Tension gashes also develop as the pre-existing R-shears pull apart (Fig. 39).

In Model E1 (α=90°; ε=90°; no initial strike-slip deformation) (Figs. 34c and 35c), faults first develop at or after 2.8 cm of displacement of the basal mobile plate (Fig. 40). The fault pattern in Model E1 is significantly different from that in Model E (Fig.

35c). Compared to those in Model E, the faults in Model E1 generally strike parallel (165° to 195°) to the long axis of the deformation zone (Fig. 34c). The deformed zone in Model E1 is slightly narrower than that in Model E (~22 cm in Model E1 vs. ~24 cm in Model E) at the end of the second phase of deformation.

3.1.2.6. Models F and F1

In Model F (α_2=105°; ε_2=97.5°) (Figs. 41b and 42b), new faults first develop after ~1.3 cm of displacement (similar to Model E) (Fig. 43). Many new faults are not associated with pre-existing faults (e.g., Figs. 43b to 43d). Other new faults nucleate at pre-existing R'-shears and propagate away from them (Fig. 44). The strike of the new faults ranges from 5° to 35° clockwise relative to the long axis of the deformation zone, resembling those of the pre-existing R-shears (Fig. 41b). The distribution of new faults is comparable to that in Models C to E. However, new faults, which develop above the basal mobile plate, where the pre-existing fault population is less developed or is not present, are longer and have higher displacement than those that develop above the basal fixed plate (Fig. 42b). During the second phase of deformation, pre-existing R- and R'-shears move southward, following the movement of the basal mobile plate (e.g., Fault 1 in Fig. 43). Reactivation of some pre-existing R-shears also occurs in this model (Fig. 45). They become more pronounced with greater dip-slip component of displacement during the second phase of deformation. Horsetail splays on pre-existing R'-shears indicate reactivation of R'-shears with left-lateral strike-slip (Fig. 40).

In Model F1 (α=105°; ε=97.5°; no initial strike-slip deformation) (Figs. 41c and 42c), faults first develop at or after 2.0 cm of displacement of the basal mobile plate (Fig.

46). The fault pattern in Model F1 is different from that in Model F (Fig. 42c). The faults strike subperpendicular (175° to 205° clockwise relative to the long axis of the deformation zone) to the applied extension direction (97.5°) (Fig. 41c). The two main deformed zones in Model F1 are closer together than the two zones of new faults in Model F. The deformed zone in Model F1 is also narrower that in Model F (~18.4 cm in Model F1 vs. ~23.2 cm in Model F at the end of the second phase of deformation.

3.1.2.7. Models G and G1

In Model G (α_2=120°; ε_2=105°) (Figs. 47b and 48b), new faults first develop at or after ~1.3 cm of displacement of the basal mobile plate (similar to those in Models E and F) (Fig. 49). The new faults initiate at pre-existing R-shears as isolated segments before subsequently propagating toward other segments and linking together (Fig. 49). Their strike (Fig. 47b) is 10° to 40° relative to the long axis of deformation zone, a similar orientation as the pre-existing R-shears. During the second phase of deformation, pre-existing R- and R'-shears move southward and rotate clockwise (e.g., Fault 1 in Fig. 49). Reactivation of some pre-existing R- and R'-shears occurs in this model (Figs. 50b, 51b, and 52c). They become more pronounced with a greater dip-slip component of displacement during the second phase of deformation (Fig. 51). Some R-shears pull apart and form tension gashes. Horsetail splays on pre-existing R'-shears indicate reactivation of R'-shears with left-lateral strike-slip before new faults cut across them (Figs. 50 and 53).

In Model G1 (α=120°; ε=105°; no initial strike-slip deformation) (Figs. 47c and 48c), faults first develop after 3.0 cm of displacement of the basal mobile plate (Fig. 54).

The faults strike 5° to 25° clockwise relative to the long axis of deformation zone, which is a slightly smaller range than that of the new faults in Model G (Figs. 47c). The displacement on the largest fault in Model G is larger than that in Model G1 (more faults in Model G1, but with less displacement). The deformed zone of this model is narrower than that in Model G (~16.8 cm in this model vs. ~24.8 cm in Model G) at the end of the second phase of deformation.

3.1.2.8. Models H and H1

In Model H (α_2=135°; ε_2=112.5°) (Figs. 55b and 56b), new faults form after ~2.3 cm of displacement of the basal mobile plate (similar to Models A to D) (Fig. 57). They develop as isolated fault segments away from the pre-existing faults (e.g., Fig. 57b) and/or initiate at pre-existing R'-shears (e.g., Fig. 58). The strike is 160° to 190° clockwise relative to the long axis of deformation zone. Reactivation of the pre-existing faults is also observable in this model. Reactivation of the pre-existing R-shears includes their greater dip-slip component of displacement as the experiment progresses (Fig. 58) and the formation of tension gashes (Fig. 59). The pre-existing R'-shears become more pronounced with slightly greater dip-slip component of displacement (e.g., Fault 6 in Fig. 60). Other faults (e.g., Faults 7 and 8 in Fig. 60), which did not reach the clay surface at the end of the first phase, presumably continue to propagate to the surface during the second phase of deformation. Horsetail splays on R'-shears also indicate reactivation of R'-shears with left-lateral strike-slip (Figs. 58 and 60).

In Model H1 (α=135°; ε=112.5°; no initial strike-slip deformation) (Figs. 56c and 57c), faults first develop after 2.2 cm of displacement of the basal mobile plate (Fig. 61).

The faults strike 10° to 40° clockwise relative to the long axis of deformation zone (Figs. 55c). In comparison to those in Model H, the faults in this model are fewer but have higher displacement (Fig. 56c). The deformed zone in Model H1 is significantly narrower than that in Model H (~16 cm in Model H1 vs. ~24 cm in Model H) at the end of the second phase of deformation.

3.1.2.9. Models I and I1

In Model I (α_2=150°; ε_2=120°) (Figs. 62b and 63b), new faults form after ~1.3 cm of displacement of the basal mobile plate (similar to those in Models E to G) (Fig. 64). They mostly initiate at pre-existing R'-shears and propagate away from them. The strike of all faults during the second phase of deformation ranges widely from 15° to 110° clockwise relative to the long axis of deformation zone (Fig. 62b). During the second phase of deformation, the pre-existing R- and R'-shears move southward and rotate clockwise (e.g., Faults 1 and 2 in Fig. 64). Reactivation of pre-existing R-shears occurs in Model I. They become more pronounced with slightly greater dip-slip component of displacement as the experiment progresses (Fault 2 in Fig. 64). Some of the pre-existing R-shears are reactivated as tension gashes (Fig. 64). Offset of superficial markers and horsetail splays on pre-existing R'-shears indicate that R'-shears are reactivated with left-lateral strike-slip (Fault 1 in Fig. 64).

In Model I1 (α=150°; ε=120°; no initial strike-slip deformation) (Figs. 62c and 63c), faults first develop after 2.7 cm of displacement of the basal mobile plate (Fig. 65). A single phase of oblique extension in Model I1 produces a simpler fault pattern (Fig. 63c) than that in Model I (Fig. 63b). The faults strike 25° to 55° clockwise relative to the

long axis of deformation zone (Fig. 62c). The largest faults in Model I1 have slightly less displacement than the largest faults in Model I. The width of the deformed zone of Model I1 is approximately the same as that of Model I at the end of the second phase of deformation (~17.6 cm).

3.2. Series 2: Two-Phase Models with Variable Magnitude of First-Phase Displacement

In the Series 2 experiments, the displacement magnitude of the strike-slip phase of deformation varies from 0 cm to 5cm. The displacement and extension directions for the strike-slip phase of deformation are identical to those in Series 1 (α_1=180°; ε_1=135) (Table 1). The displacement and extension directions for the second phase of deformation are identical to those in Model E in Series 1 (α_2=90°; ε_2=90°) (Table 1). The Series 2 experiments show how the properties of a population of pre-existing strike-slip faults control deformation patterns during a subsequent phase of extension.

3.2.1. First-phase fault population

Model 0 does not undergo an initial deformation (Fig. 66a). Thus, no first-phase fault population is developed. During the strike-slip phase of deformation (1st phase), the clay above the mobile plate in Models 1 to 3 (d_1 = 1 to 3 cm) moves southward, but the clay surface is not faulted (Figs. 66b to d). In Model 4 (d_1 = 4 cm), a few R- and R'-shears develop at the edge of the area of analysis (Fig. 66e). In Model 5 (d_1 = 5 cm), numerous R- and R'-shears develop above the silicone polymer and the edge of the overlapping plates (Fig. 66f). The R- and R'-shears in Models 4 and 5 strike 10°-20° and

80°-90° clockwise relative to the long axis of deformation zone. The characteristics of these faults are very similar to those that develop during the strike-slip phase of deformation in Series I.

3.2.2. Second-phase fault population

During the second phase of deformation, α_2 and ε_2 are identical to those in Model E in Series 1. Fig. 67 shows the evolution of the new faults during second phase of deformation in all models. In models with no or poorly developed pre-existing faults (Models 1 to 4), new faults first appear as isolated segments and subsequently form linkages as the displacement increases. Some new faults in Models 2-4 are oblique to the extension direction during the second phase, suggesting that they partially or completely reactivate R-shears that did not reach the surface. In Model 5 (identical to Model E in Series 1), where pre-existing faults are better developed, new faults also initiate at pre-existing R'-shears and propagate away from them. As the displacement magnitude of the first phase increases, the strike of most faults in the second phase of deformation becomes more oblique to the second-phase extension direction and more subparallel to the R-shear orientation.

The length of some pre-existing R-shears increases, indicating reactivation of these faults. Other R-shears reactivate with significantly greater dip-slip component of displacement as the experiment progresses. Some pre-existing R-shears pull apart and become tension gashes.

3.3. Cross-Section Analysis

Cross sections through a layered model (α_1=180°; ε_1=135°; α_2=90°; ε_2=90°; similar to Model E in Series 1) show the geometry of the faults that develop during the two phases of deformation (Fig. 68). Both R- and R'-shears develop during the strike-slip phase of deformation (Fig. 68a). During the second phase of deformation, normal faults develop. In map view, they have two major strikes: subparallel to the trend of the deformation zone and subparallel to the pre-existing R-shears (similar to those in Model E). In cross-section view, the new faults have dip angles ranging from ~60° to 80°. The strike-slip faults have very small normal separation and very high dip angles (~80° to 90°). The layered model also shows that more faults are present at the base of the clay than at the top of the clay.

4. DISCUSSION

4.1. Summary of Modeling Results

In all Series 1 models (Fig. 69), en-échelon R- and R'-shears develop above the silicone polymer and the overlapping plates during the first phase of deformation (strike-slip). R-shears have right-lateral slip, and R'-shears have left-lateral slip. The summed lengths of fault segments for the R- and R'-shears and the total summed lengths of all segments vary in the models (see Fig. 10), despite the identical boundary conditions and use of the same batch of clay in all models. This variability may be a random process governed by where and when the first R- and R'-shears develop, similar to the origin of fault-dip domains for arrays of normal faults (Schlische and Withjack, 2009).

In all Series 1 models, both the formation of new faults and the reactivation of pre-existing faults occur during the second phase of deformation (Figs. 69 and 70). Formation of new faults mostly occurs in models in which $\alpha_2<60°$ ($\varepsilon_2<75°$; Models A to C). In models in which $\alpha_2>60°$ ($\varepsilon_2>75°$), reactivation of pre-existing R- and/or R'-shears accommodate most deformation (Fig. 70). During the second phase of deformation, the maximum extension direction relative to the strike of the R- and R'-shears controls the likelihood of reactivation of the pre-existing faults, the sense of slip on the reactivated pre-existing high-angle faults, and the orientation of new faults (Fig. 70). Moreover, the experimental models show that the high-angle faults that form during the strike-slip phase of deformation influence the development of the new faults that form during the subsequent second phase of extension.

The type of reactivation varies within the Series 1 models (Fig. 69). In Model A ($\alpha_2=30°$; $\varepsilon_2=60°$), the pre-existing right-lateral R-shears are reactivated with an opposite sense of slip (left-lateral). In Models B to I ($\alpha_2=45°$ to $\alpha_2=150°$; $\varepsilon_2=67.5°$ to $\varepsilon_2=120°$), the pre-existing R-shears are reactivated as high-angle normal faults. Some of the pre-existing R-shears pull apart, becoming tension gashes filled with silicone polymer in Models D to H. In Model D, the pre-existing R-shears are reactivated with a slight dip-slip and left-lateral component of slip. In Models F to I, the pre-existing R'-shears are reactivated with oblique-slip (left-lateral and normal components).

New faults that develop during the second phase of deformation fall into three categories based on their orientation (Fig. 70): 1) new faults that strike subperpendicular to the maximum extension direction in Models A to C ($\alpha_2=30°$, 45°, and 60°; $\varepsilon_2=60°$, 67.5°, and 75°), 2) new faults that are subparallel to the strike of the pre-existing R-shears

in Models D to F (α_2=75° to α_2=105°; ε_2=82.5° to ε_2=97.5°), and 3) new faults that are subparallel to the strike of the pre-existing R-shears and/or subperpendicular to the second-phase extension direction in Models G to I (α_2=120° to α_2=150°; ε_2=105° to ε_2=120°). Figure 70 lists the angle between the average strike of the R-shears and the second-phase extension direction.

The Series 1 models also show that a well-developed, pre-existing high-angle fault population can inhibit the development of new faults, perhaps by serving as lateral obstacles to the propagation of new faults (Fig. 71). Where the pre-existing fault population is poorly developed, new faults are abundant, long, and have large displacements. Where the pre-existing fault population is well developed, new faults are fewer, shorter, and have less displacement. The new faults that do develop commonly initiate at pre-existing high-angle faults. This suggests that pre-existing high-angle faults can also act as sites of nucleation for new faults.

As the experiments progress, new faults commonly interact with pre-existing faults by cutting across, initiating at, and/or intersecting them (Fig. 76). During the first phase of deformation (strike-slip), the R-shears offset the R'-shears with right-lateral separation. They also intersect the R'-shears. During the second phase of deformation (extensional), new faults may initiate at pre-existing high-angle faults and propagate away from them. The new faults that nucleate at the pre-existing faults, however, are usually short. The new faults may also lose displacement after cutting across the pre-existing high-angle faults. These interactions suggest that the pre-existing high-angle faults could serve as nucleation sites and/or lateral obstacles.

In the Series 2 models (α_1=180°; ε_1=135°; α_2=ε_2=90°) where the development of the first-phase fault population varies, new faults become increasingly subparallel to the orientation of the R-shears as the first-phase fault population becomes better developed (Fig. 72). Even in models (e.g, Models 1-3) in which no first-phase faults cut the top of the clay, the strike of the new faults differs from that predicted by the extension direction during the second phase. This suggests that pre-existing high-angle faults at depth and/or very small faults (invisible) at the surface can control new fault development and orientations during a subsequent phase of extension. The new faults may propagate upward and are reoriented during the second phase of deformation, with the degree of reorientation increasing as the amount of upward propagation increases. The layered model shows that more faults cut the bottom of the clay than cut the top of the clay, suggesting that many faults nucleate at the base of the clay and propagate upward to the top of the clay.

4.2. Comparisons to Previous Modeling Results

The fault patterns that form during the first phase of deformation (strike-slip) in the models are similar to that in the previous modeling results with similar (but not identical) boundary conditions (e.g., Cloos, 1928; Riedel, 1929; Tchalenko, 1970; Withjack and Jamison, 1986; Sylvester, 1988; Clifton et al., 2000; Atmaoui et al., 2006). Namely en-échelon R- and R'-shears develop. The fault patterns in the single-phase models (Models A1 to I1) are similar to those in the clay models described by Withjack and Jamison (1986) and Clifton et al (2000). No previous studies have investigated whether high-angle faults are reactivated during a subsequent episode of extension.

4.3. Fault Reactivation

Mohr-circle diagrams (Fig. 73) show the predicted range of fault orientations for reactivation. The value for the coefficient of sliding friction for clay is not well constrained but, like Henza et al. (2010), I assume that the frictional-sliding failure envelop parallels the Mohr-Coulomb failure envelop for undeformed clay (μ = 0.6 and C = 50 Pa or C = 100 Pa). The value C is not well constrained, so I also show Mohr diagrams for $C \sim 50$ Pa and $C \sim 100$ Pa. For a σ_1-vertical stress state, the value for σ_v (σ_1) is 510 Pa (calculated using $\sigma_v = \rho g h$; where ρ is 1,600 kg m^{-3}; g is 9.8 m s^{-2}; h is 0.0325 m); the σ_3 value (110 Pa) is constrained by the largest Mohr circle that is tangent to the Mohr-Coulomb failure envelop (Fig. 73c). For a σ_1-horizontal stress state, $\sigma_v = \sigma_2$ = 510 Pa, and I assume that σ_2 lies midway between σ_1 and σ_3, whose values (820 Pa and 220 Pa), respectively, are given by the largest circle that is tangent to the Mohr-Coulomb failure envelop (Fig. 73d). Based on C = 100 Pa and the other values given above, the Mohr diagram predicts that reactivation window during the second phase of deformation is 50° (σ_1-vertical stress state) and 40° (σ_1-horizontal stress state). Based on C = 50 Pa, the Mohr diagram predicts that reactivation window during the second phase of deformation is 37.5° (σ_1-vertical stress state) and 30° (σ_1-horizontal stress state). Thus, as the cohesion value increases, the likelihood of fault reactivation also increases. As the dip angle of the pre-existing faults increases, the likelihood of fault reactivation decreases. The most important parameter is the apparent dip of the reactivated fault measured in the direction of maximum horizontal extension.

In Model A (α_2=30°; ε_2=60°) and Model I (α_2=150°; ε_2=120°), either σ_1 or σ_2 could be vertical (Withjack and Jamison, 1986), depending on the assumed value of the Poisson ratio. Thus, two types of stress states are possible (σ_1-vertical and σ_1-horizontal) in these models (Fig. 74). The Mohr diagram predicts that the pre-existing R- and R'-shears (dip ~80° based on cross-section views) in Model A will fall into the reactivation window for the σ_1-vertical stress state. However, according to the Mohr diagram, only pre-existing R-shears should be reactivated for the σ_1-horizontal stress state; pre-existing R'-shears do not lie in the reactivation window. Although the faults fall within the reactivation window for the σ_1-vertical stress state, the reactivated faults would have a large strike-slip component because the extension direction is oblique to the strike of the faults. In Model A, the observations better match the predictions for the σ_1-horizontal stress state. The pre-existing R-shears are reactivated with left-lateral slip, and no reactivation occurs on the pre-existing R-shears.

In Model I, the predictions of the σ_1-vertical stress state better match the observations. The pre-existing R-shears are reactivated with predominantly a normal component of slip or as tension gashes, and the pre-existing R'-shears are reactivated with oblique-slip (left-lateral and normal components). The stress states that produce reactivation are different in Models A and I because, theoretically, either σ_1 or σ_2 could be vertical (Withjack and Jamison, 1986).

In Models B to H, the orientation of σ_1 (the maximum principal stress) is vertical during the second phase of deformation. Thus, only the σ_1-vertical stress state applies to these models (Fig. 75). Based on the observations, most models (except Models B and C) agree with the predicted reactivation based on the Mohr diagrams. The pre-existing R-

shears are reactivated with a predominantly normal component of slip or as tension gashes. As the dip angle of the R-shears increases, the likelihood that they are not reactivated as faults but instead as tension gashes increases; this is because the very steeply dipping faults cannot accommodate much horizontal extension. The pre-existing R'-shears are not reactivated in Models B to E but are reactivated with oblique-slip (left-lateral and normal components) in Models F to H. In Models B and C, the Mohr diagram predicts the reactivation of R-shears, but I observe no evidence that the R'-shears in these models underwent reactivation.

4.4. Comparisons to Natural Example

The geological map of the Gulf of Suez region shows Precambrian strike-slip faults within the Rihba shear zone (Fig. 77a). The faults have two dominant orientations: NNE and WNW (Younes and McClay, 2002). The Abu Durba area is located on the southeastern margin of the Gulf of Suez (McClay and Khalil, 1998; Fig. 77b). The geological map of this area shows faults with two dominant orientations: NNW and NNE. The NNE-striking faults (e.g., the Erma and Durba transfer faults) developed before the Late Oligocene-Miocene rifting event in the Gulf of Suez (Moustafa, 1996a and b; McClay and Khalil, 1998). The possible regional extension direction during rifting ranges from 220° to 240° (derived from the largest petal of the rose diagram of new faults in figure 10 of Younes and McClay, 2002). According to Moustafa (1996a and b) and McClay and Khalil (1998), the NNE-striking faults were reactivated as oblique-slip faults with normal and left-lateral strike-slip components within relay ramps between en-echélon NNW-striking normal faults during the early stages of rifting. Horsetail splays

formed at the terminations of the NNE-striking faults and formed linkages with new NNW-striking faults, confirming the reactivation of the faults. The NNW-striking normal faults generally terminate against the reactivated NNE-striking faults (McClay and Khalil, 1998).

The fault patterns and interactions between the reactivated pre-existing NNE-striking faults and the newly formed NNW-striking faults in the Abu Durba area closely resemble those that form in Model G of Series 1 (Fig. 78). As displacement increases, pre-existing high-angle R'-shears are reactivated as oblique-slip faults with normal and left-lateral strike-slip components during the second phase of deformation. These reactivated high-angle R'-shears impede the propagation of new normal faults (i.e., the new faults lose displacement near the reactivated high-angle R'-shears). Horsetail splays at the termination of the R'-shears also link with the new normal faults. It appears that the new normal faults eventually cut the R'-shears and stop their activity. The pre-existing R'-shears population in the Abu Durba area may not be as well developed as that in Model G. However, the reactivated pre-existing R'-shears and new normal faults in Model G, particularly at a moderate stage of development (Fig. 78b), are comparable to the reactivated NNE-striking oblique-slip faults and newly formed NNW-striking normal faults in the Abu Durba area of the southern Suez rift system. In Model G, the extension direction is subperpendicular to the pre-existing R-shears and at small angle to the pre-existing R'-shears (~22°). In the Suez rift, the angle between the inferred regional extension direction and the strike of the pre-existing faults (e.g., Ekma and Durba faults) is ~25° to ~35°. As mentioned previously, the range of the inferred regional extension

direction is 220° to 240°; the modeling results suggest that the regional extension direction in the Abu Durba area is approximately 220°.

5. SUMMARY AND CONCLUSIONS

I use experimental models with wet clay to study the extensional reactivation of pre-existing high-angle strike-slip faults and their influence on the development of new faults.

- During the strike-slip phase of deformation, R- and R'-shears (strike-slip faults) develop. In map view, they appear as en-échelon segments. The R-shears strike 10°-20° clockwise relative to the long axis of the deformation zone and have right-lateral strike-slip. The R'-shears strike 80°-90° clockwise relative to the long axis of the deformation zone and have left-lateral strike-slip. The summed lengths of the R- and R'-shears is variable in the models.
- During the second phase of deformation (extension), the reactivation of the pre-existing faults and the formation of new faults accommodate the deformation. In cross-section view, the R- and R'-shears are very high-angle faults but are not necessarily vertical (~80°). The new faults have dip angles ranging from ~60° to ~80°.
- The maximum extension direction relative to the strike of the R- and R'-shears controls the likelihood of reactivation of the pre-existing faults, the sense of slip on the reactivated pre-existing high-angle faults, and the orientation of new faults. Pre-existing high-angle faults are more likely to be reactivated as high-angle normal faults if they strike subperpendicular to the extension direction. Some of

the pre-existing R-shears pull apart becoming tension gashes because subvertical faults can accommodate little or no horizontal extension. Pre-existing high-angle faults are more likely to be reactivated as oblique-slip/strike-slip faults if they strike subparallel to the extension direction.

- The strike of new faults is more likely to be subparallel to that of the R-shears if the population of pre-existing high-angle strike-slip faults is well developed. Pre-existing high-angle faults at depth and/or numerous small faults (invisible) at the surface can control new fault development and orientations during a subsequent phase of extension. The new faults would propagate upward from the base of the model and some of them are reoriented during the second phase of deformation, with the degree of reorientation increasing as the amount of upward propagation increases.
- A pre-existing high-angle fault population can inhibit the development of new faults. Where a pre-existing fault population is less developed, new faults are more likely to be abundant, long, and have large displacement. Where a pre-existing fault population is better developed, new faults are more likely to be fewer, shorter, and have less displacement.
- New faults commonly interact with pre-existing faults by cutting across, initiating at, and/or intersecting them. These interactions suggest that the pre-existing high-angle faults may serve as nucleation sites and/or lateral obstacles.
- A Mohr diagram analysis of reactivation using average parameters for the wet clay (e.g., cohesion, coefficient of sliding friction, and Coulomb coefficient) successfully predicts reactivation of the pre-existing faults in most models. The

discrepancy between predictions and observations may be due to poor constraints on some parameters (e.g., the cohesion of wet clay) or the range of values for the dips and strike of the pre-existing faults. Increasing the cohesion value increases the likelihood of fault reactivation. Increasing the dip angle of the pre-existing faults decreases the likelihood of fault reactivation. The most important parameter is the apparent dip of the reactivated fault measured in the direction of maximum horizontal extension.

- The reactivation of the pre-existing high-angle faults during a subsequent episode of deformation and the interactions between the pre-existing high-angle faults and the new faults in this study are comparable to those observed in nature, such as those in the Abu Durba area (Suez rift). The models in this study provide insights to explain the complex fault patterns and fault evolution in this area and to better constrain the regional extension direction.

REFERENCES

Abdeen, M. M., 1995, Late orogenic basin evolution and deformation in the Pan-African basement, Wadi Queih, Eastern Desert of Egypt: Ph.D. dissertation, Heidelberg University, Germany, 239 p.

Abu Zeid, H. T., 1984, Geology of the Wadi Hamrawin area, Red Sea hills, Eastern Desert, Egypt: Ph.D. thesis, University of South Carolina, Columbia, South Carolina, 234 p.

Atmaoui, N., N. Kukowski, B. Stöckhert, and D. König, 2006, Initiation and development of pull-apart basins with Riedel shear mechanism: Insights from scaled clay experiments: International Journal of Earth Sciences, v. 95, no. 2, p. 225–238.

Byerlee, J., 1978, Friction of rocks. Pure and Applied Geophysics 116, 615–626.

Clifton, A.E., Schlische, R.W., Withjack, M.O., Ackermann, R.V., 2000. Influence of rift obliquity on fault-population systematics: results of clay modeling experiments. Journal of Structural Geology 22, 1491–1509.

Cloos, H., 1928, Experimente zur inneren tektonik: Centralblatt für Mineralogie, part B, p. 609–621.

Eisenstadt, G., Sims, D., 2005, Evaluating sand and clay models: do rheological differences matter? Journal of Structural Geology 27, 1399–1412.

Eisenstadt, G., Withjack, M.O., 1995, Estimating inversion: results from clay models. In: Buchanan, P. G. (Eds), Basin Inversion. Geological Society Special Publication No. 88, 119-136.

Faccenna, C., Nalpas, T., Brun, J., Davy, P., and Bosi, V., 1994, The influence of pre-existing thrust faults on normal fault geometry in nature and in experiments. Journal of Structural Geology 17 1139-1149

Handin, 1966, Strength and ductility. In: Clark, S.P. (Ed.), Handbook of Physical Constants, 97. Geological Society of America Memoir, pp. 233–289.

Henza, A.A., Withjack, M.O., Schlische, R.W., 2009, Normal-fault development during two phases of non-coaxial extension: an experimental study. Journal of Structural Geology 32, 1656-1667

Henza, A.A., Withjack, M.O., Schlische, R.W., 2010, How do properties of a pre-existing normal-fault population influence faults development during a subsequent phase of extension? Journal of Structural Geology 33 1312-132

McClay, K., Khalil, S., 1998, Extensional hard linkages, eastern Gulf of Suez, Egypt. Geology 26, 563-566

Moustafa, A.R., 1996a, Internal structure and deformation of an accommodation zone in the northern part of the Suez rift. Journal of Structural Geology 18, 93-107.

Moustafa, A.R., 1996b, Structural setting and tectonic evolution of the northern Hammam Faraun Block (Wadi Wasit-Wadi Wardan area), eastern side of the Suez rift. Kuwait Journal of Science and Engineering 23, 105-122.

Moustafa, A.R., 1997, Controls on the development and evolution of transfer zones: the influence of basement structure and sedimentary thickness in the Suez rift and Red Sea. Journal of Structural Geology 19, 755-768.

Riedel, W., 1929, Zur Mechanik geologischer Brucherscheinungen; Ein Betrag zum Problem der “Fiederspalten”: Centralblatt für Mineralogie, Geologie, und

Paleontologie, part B, p. 354–368.

Schlische, R.W., Withjack, M.O., Eisenstadt, G., 2002, An experimental study of the secondary deformation produced by oblique-slip normal faulting. AAPG Bulletin 86, 885-906.

Schlische, R. W., Withjack, M. O., 2009, Origin of fault domains and fault-domain boundaries (transfer zones and accommodation zones) in extensional provinces: Result of random nucleation and self-organized fault growth. Journal of Structural Geology 31, 910-925.

Sims, D. 1993, The rheology of clay: a modeling material for geologic structures. Los, Transactions, American Geophysical Union, 569.

Stern, R., and C. Hedge, 1985, Geochronological and isotopic constraint on the late Precambrian crustal evolution in the Eastern Desert of Egypt: American Journal of Science, v. 258, p. 97-127.

Sylvester, G. Arthur., 1988, Strike-slip faults. Geological Society of America Buletin, v. 100, p. 1666-1703.

Tchalenko, J. S., 1970, Similarities between shear zones of different magnitudes: Geological Society of America Bulletin, v. 81, p. 1625–1640.

Vendeville , B., Withjack, M. O., and Eisenstadt, G., 1995, Introduction to experimental omdeling of tectonic processes: Geological Society of America, Short Course Notes, 1995 National Meeting, 120 p.

Weijermars, R., 1986, Flow behaviour and physical chemistry of bouncing putties and related polymers in view of tectonic laboratory applications. Tectonophysics 124, 325-358.

Withjack, M.O., Jamison, W.R., 1986, Deformation produced by oblique rifting. Tectonophysics 126, 99-124.

Withjack, M.O., Callaway, S., 2000, Active normal faulting beneath a salt layer: an experimental study of deformation patterns in the cover sequence. AAPG Bulletin 84, 627e651.

Withjack, M.O., Schlische, R.W., 2006, Geometric and experimental models of extensional fault-bend folds. In: Buiter, S.J.H., Schreurs, G. (Eds.), Analogue and Numerical Modelling of Crustal-Scale Processes. Geological Society (London) Special Publication, vol. 253, pp. 285e305.

Withjack, M.O., Schlische, R.W., Henza, A.A., 2007, Scaled experimental models of extension: dry sand vs.wet clay. Houston Geological Survey Bulletin 49 (8), 31–49

Younes, A.I. and K.R. McClay., 2002, Development of accommodation zones in the Gulf of Suez-Red Sea rift, Egypt. American Association of Petroleum Geologists Bulletin, v. 86, p. 1003-1026

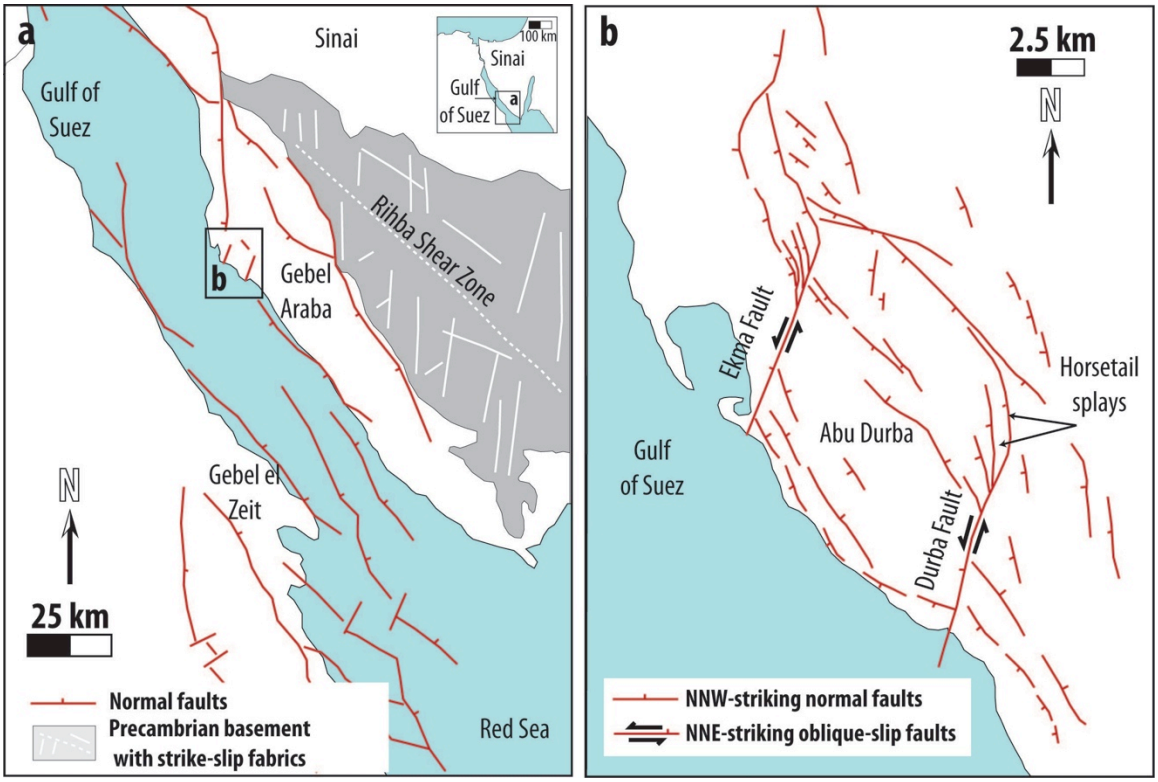

Figure 1. Fault pattern (a) from Suez rift showing major faults and shear zone (see inset map for location) and (b) from Abu Durba area of southern part of Suez rift (see inset map in part a for location) (modified from McClay and Khalil, 1998; Younes and McClay, 2002). In Abu Durba area, basement faults were reactivated with oblique slip during Oligocene-Miocene rifting and interacted with new normal faults, forming an intersecting fault pattern (McClay and Khalil, 1998). New normal faults lose displacements near the pre-existing faults.

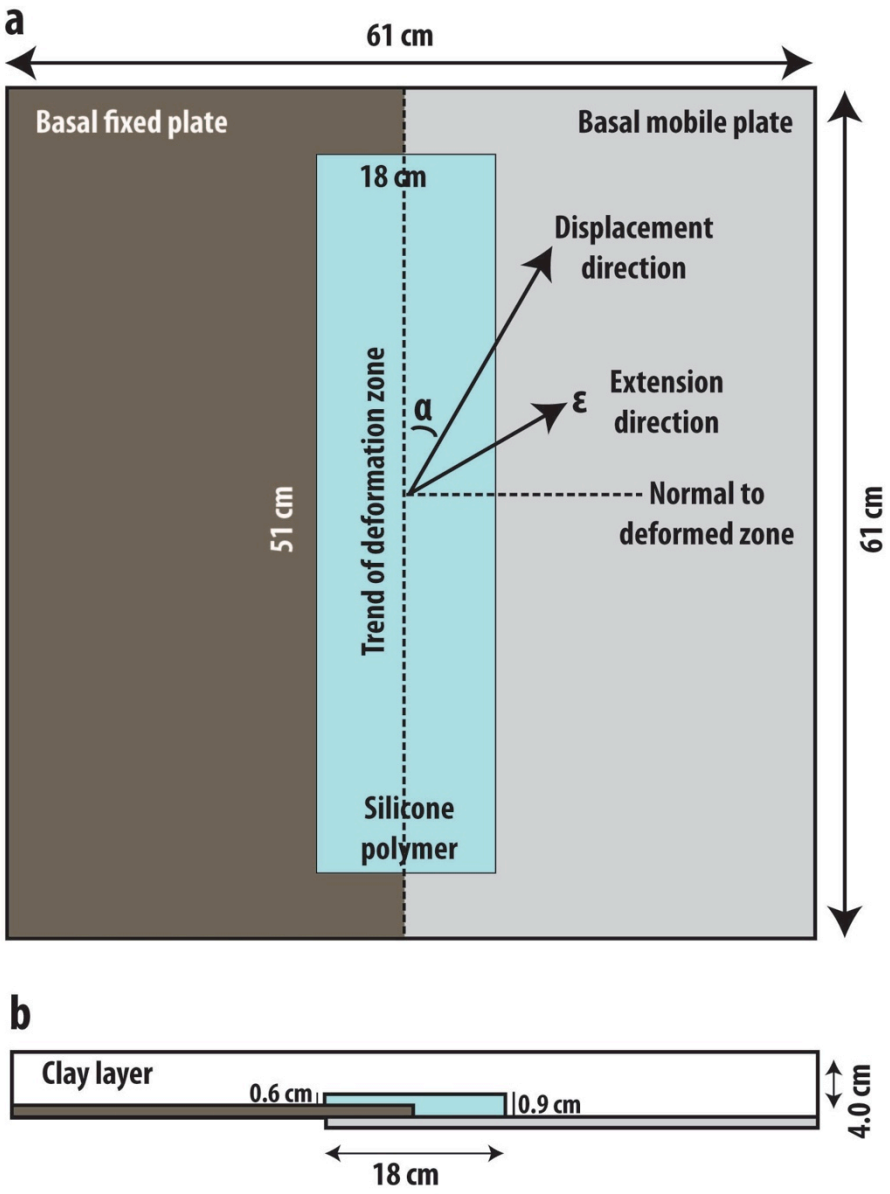

Figure 2. Sketch of experimental modeling apparatus in (a) map view and (b) cross-sectional view. During the first phase, the mobile plate moves in a right-lateral sense relative to the fixed plate. During the second phase, the mobile plate moves away from the fixed plate. α is the angle measured clockwise from trend of deformation zone to displacement direction (Withjack and Jamison, 1986). The extension direction (ε) is midway between the displacement direction and the normal to deformed zone. The dark and light areas represent basal fixed and mobile plates. The light blue are represents silicone polymer.

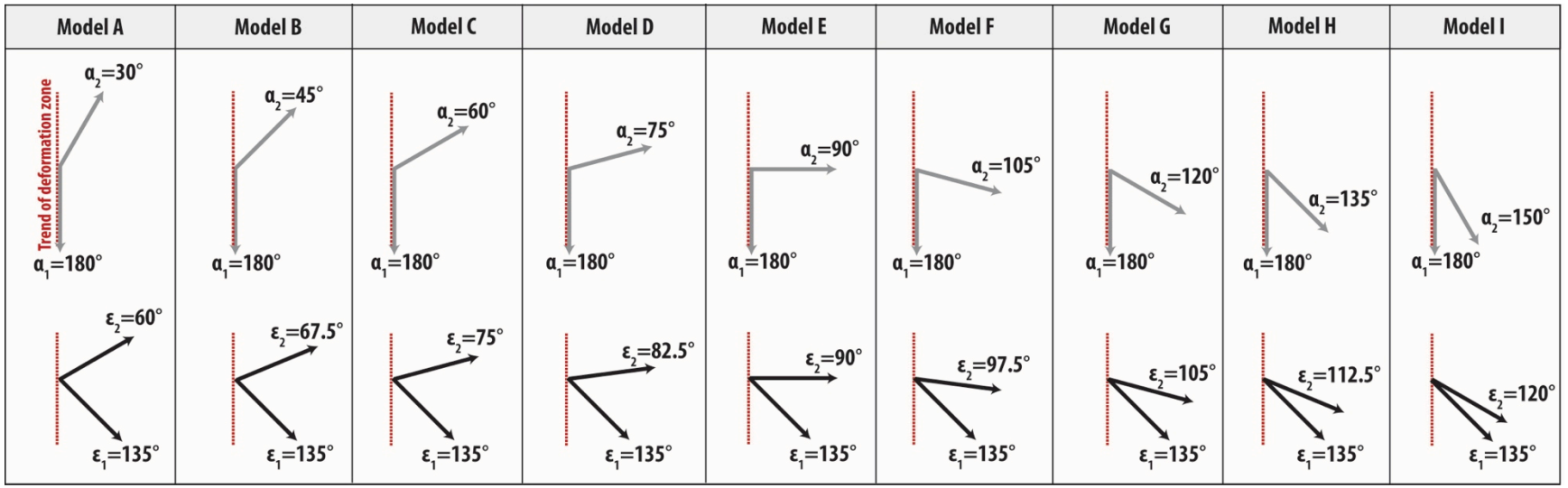

Figure 3. Displacement and extension directions for Series 1 models. α_1 is the displacement direction during the strike-slip phase of deformation, and α_2 is the displacement direction during the second phase of deformation. ε_1 is the extension direction during the strike-slip phase of deformation, and ε_2 is extension direction during the second phase of deformation.

Series 1 - two phase	Model A	Model B	Model C	Model D	Model E	Model F	Model G	Model H	Model I	Layered
1st phase final magnitude of displacement (cm)	5	5	5	5	5	5	5	5	5	5
2nd phase final magnitude of displacement (cm)	5	5	5	5	5	5	5	5	5	2.5
1st phase displacement direction (α_1)	180°	180°	180°	180°	180°	180°	180°	180°	180°	180°
1st phase extension direction (ε_1)	135°	135°	135°	135°	135°	135°	135°	135°	135°	135°
2nd phase displacement direction (α_2)	30°	45°	60°	75°	90°	105°	120°	135°	150°	90°
2nd phase extension direction (ε_2)	60°	67.5°	75°	82.5°	90°	97.5°	105°	112.5°	120°	90°

Series 1 - single phase	Model A	Model B	Model C	Model D	Model E	Model F	Model G	Model H	Model I
Final magnitude of displacement (cm)	5	5	5	5	5	5	5	5	5
Displacement direction (α)	30°	45°	60°	75°	90°	105°	120°	135°	150°
Extension direction (ε)	60°	67.5°	75°	82.5°	90°	97.5°	105°	112.5°	120°

Series 2	Model 0	Model 1	Model 2	Model 3	Model 4	Model 5
1st phase final magnitude of displacement (cm)	0	1	2	3	4	5
2nd phase final magnitude of displacement (cm)	5	5	5	5	5	5
1st phase displacement direction (α_1)	180°	180°	180°	180°	180°	180°
1st phase extension direction (ε_1)	135°	135°	135°	135°	135°	135°
2nd phase displacement direction (α_2)	90°	90°	90°	90°	90°	90°
2nd phase extension direction (ε_2)	90°	90°	90°	90°	90°	90°

Table 1. Parameters in Series 1 and 2 models. Extension direction (ε) is midway between the displacement direction and the normal to deformation zone.

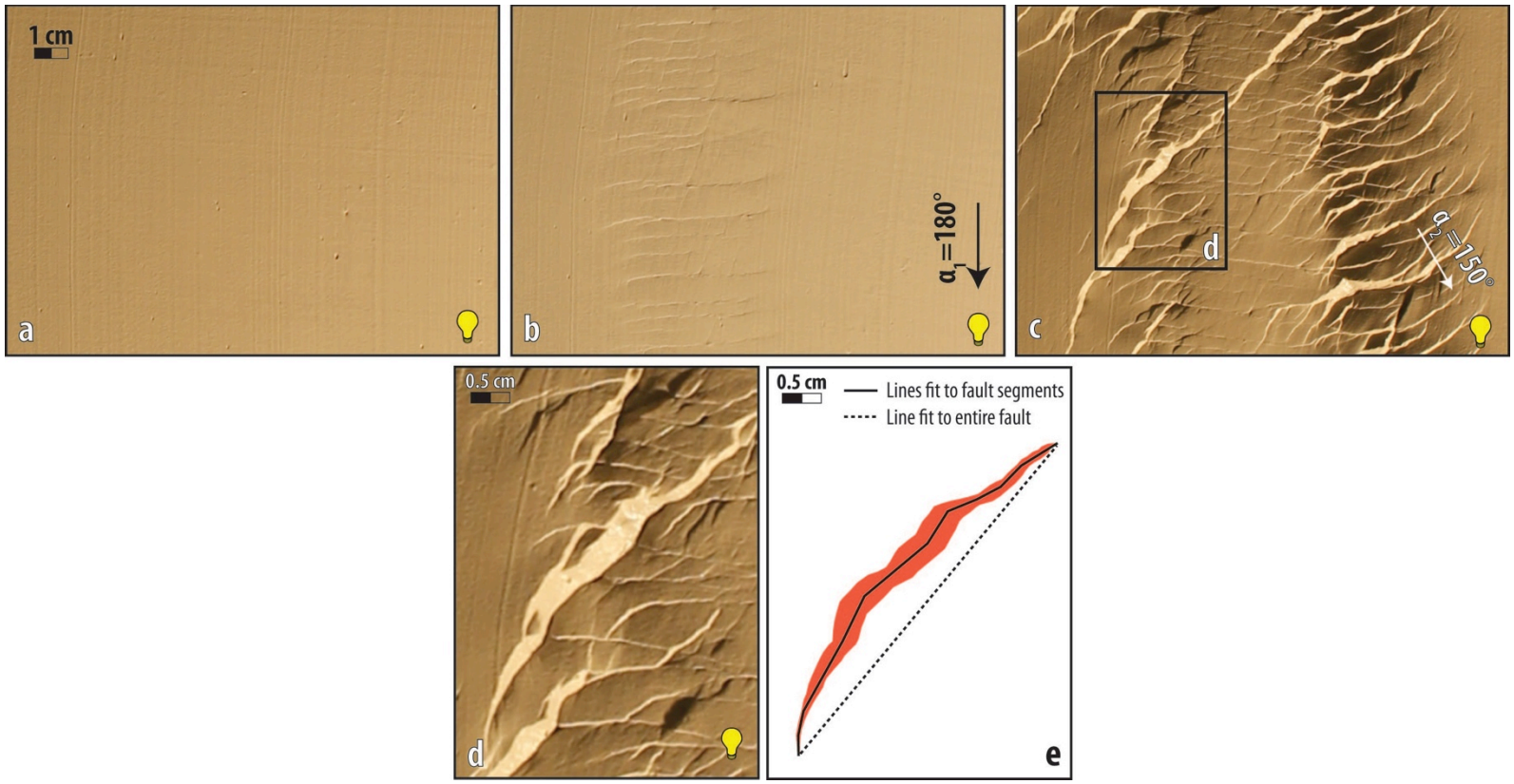

Figure 4. Methods used in fault analysis. Photographs of the top surface of the clay layer of Model I showing superficial linear markers at the beginning of the experiment (a), after the strike-slip phase of deformation (b), and after the second phase of deformation (c). Offset markers indicate the separation on faults. Arrows indicate displacement direction for each phase. (d) Photograph of a segmented fault scarp (bright on photograph). Fault scarps dipping toward light appear bright; fault scarps dipping away from light appear dark. (e) Line drawing of a segmented fault showing straight-line fit for each fault segment. The segments lie midway between the hanging-wall and footwall cutoffs. The strike difference between adjacent segments is ~5°. Fitting lines to fault segments results in several distinct segments with several distinct orientations, whereas a tip-to-tip line yields one fault with one orientation.

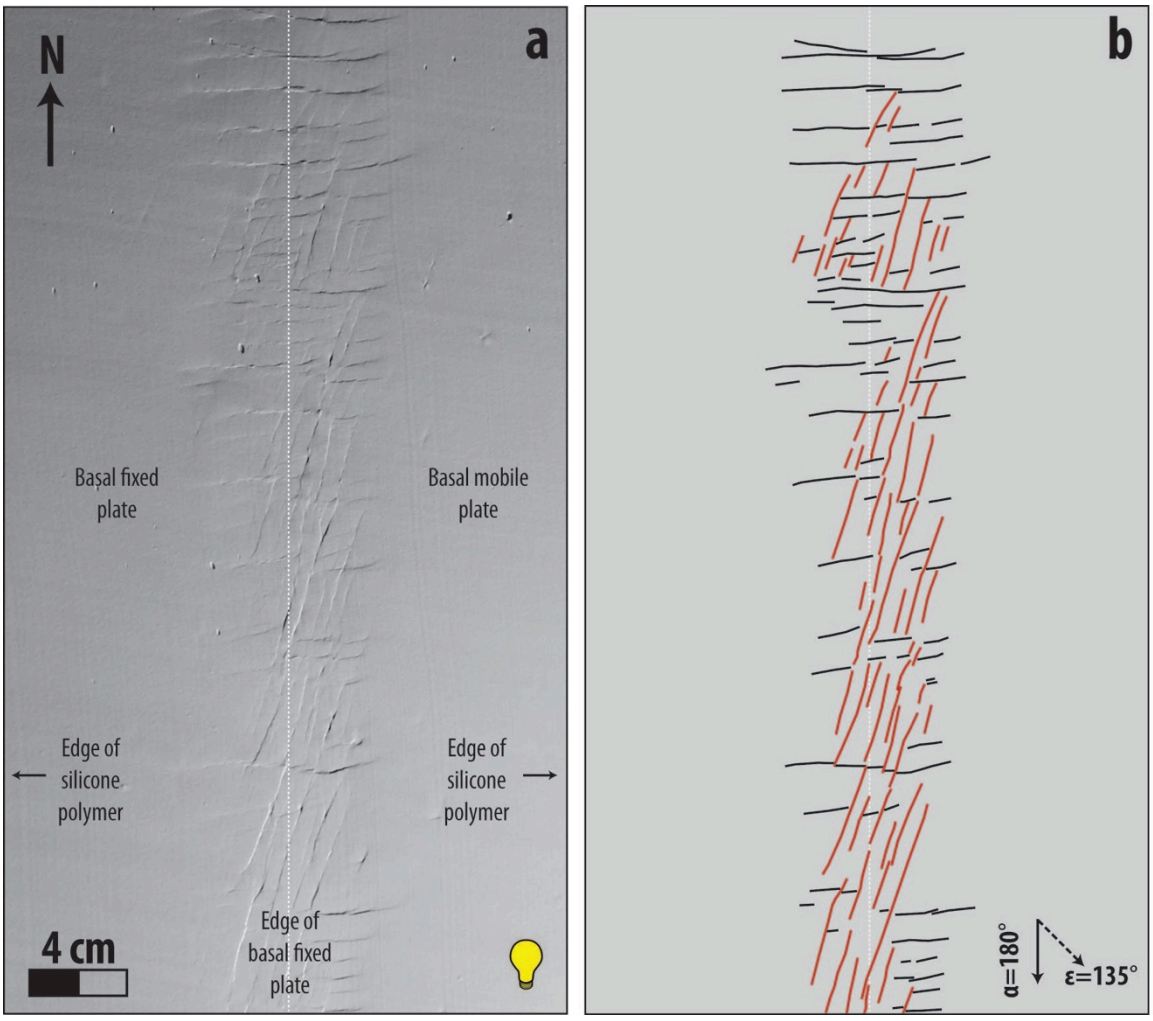

Figure 5. Map view of fault pattern of Model C at end of strike-slip phase of deformation. a) Photograph of top surface. Fault scarps dipping toward light appear bright; fault scarps dipping away from light appear dark. b) Line drawing showing faults (NNE-striking faults are red; E-striking faults are black). Dashed arrow shows extension direction (ε =135°) and solid arrow shows displacement direction (α=180°) measured clockwise relative to long axis of deformation zone (north arrow). Sides of photograph and line drawing are above outer edges of silicone polymer beneath clay layer. Observable deformation occurs only in a narrow zone centered above edge of overlapping plates.

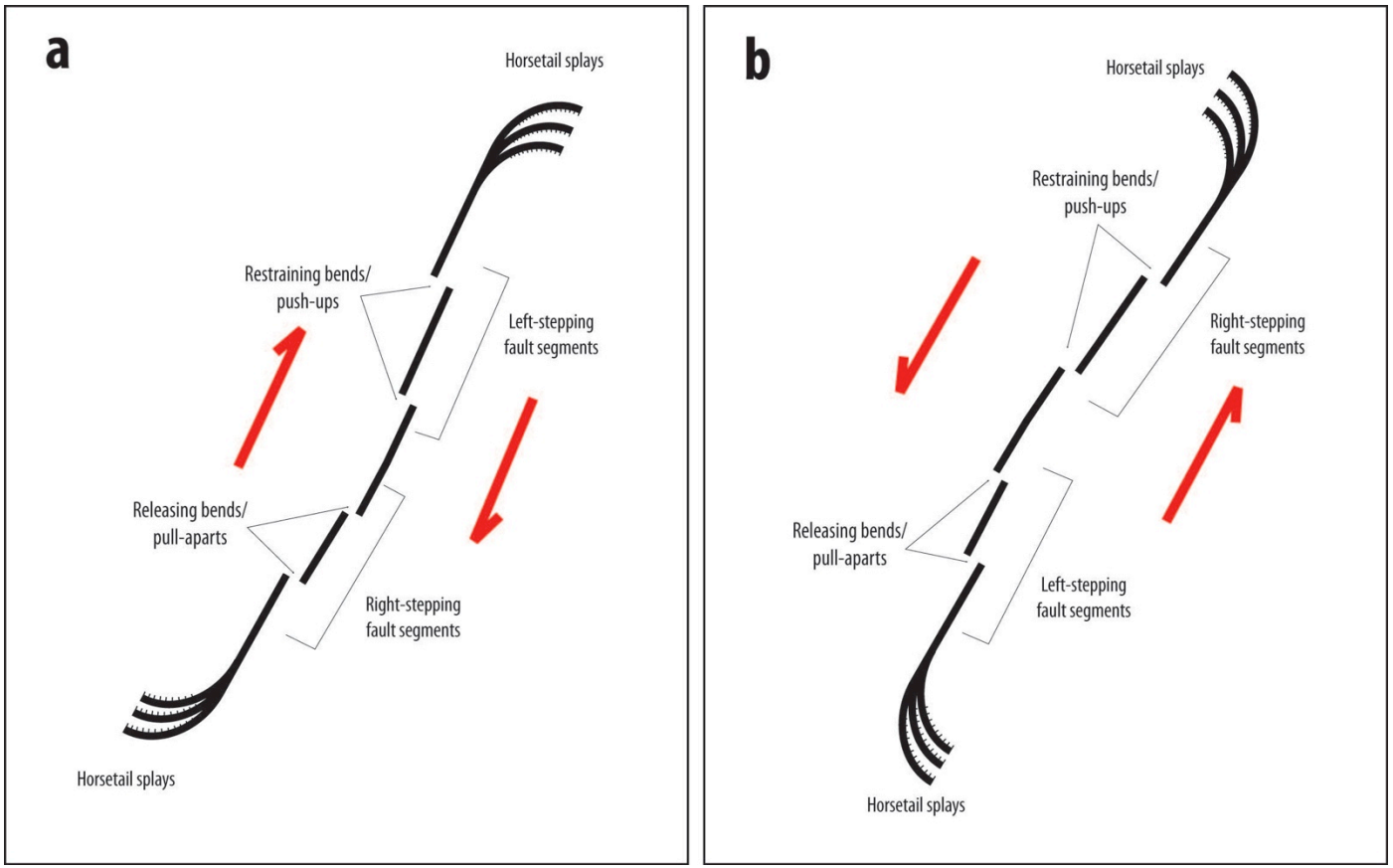

Figure 6. General relationships between strike-slip fault segments in map view and their associated structures. a) Left-stepping fault segments with right-lateral slip are associated with restraining bends or push-up structures; right-stepping fault segments with right-lateral slip are associated with releasing bends or pull-apart structures. b) Right-stepping fault segments with left-lateral slip are associated with restraining bends or push-up structures; left-stepping fault segments with left-lateral slip are associated with releasing bends or pull-apart structures. Faulting at fault terminations (horsetail splays) is a type of releasing structure.

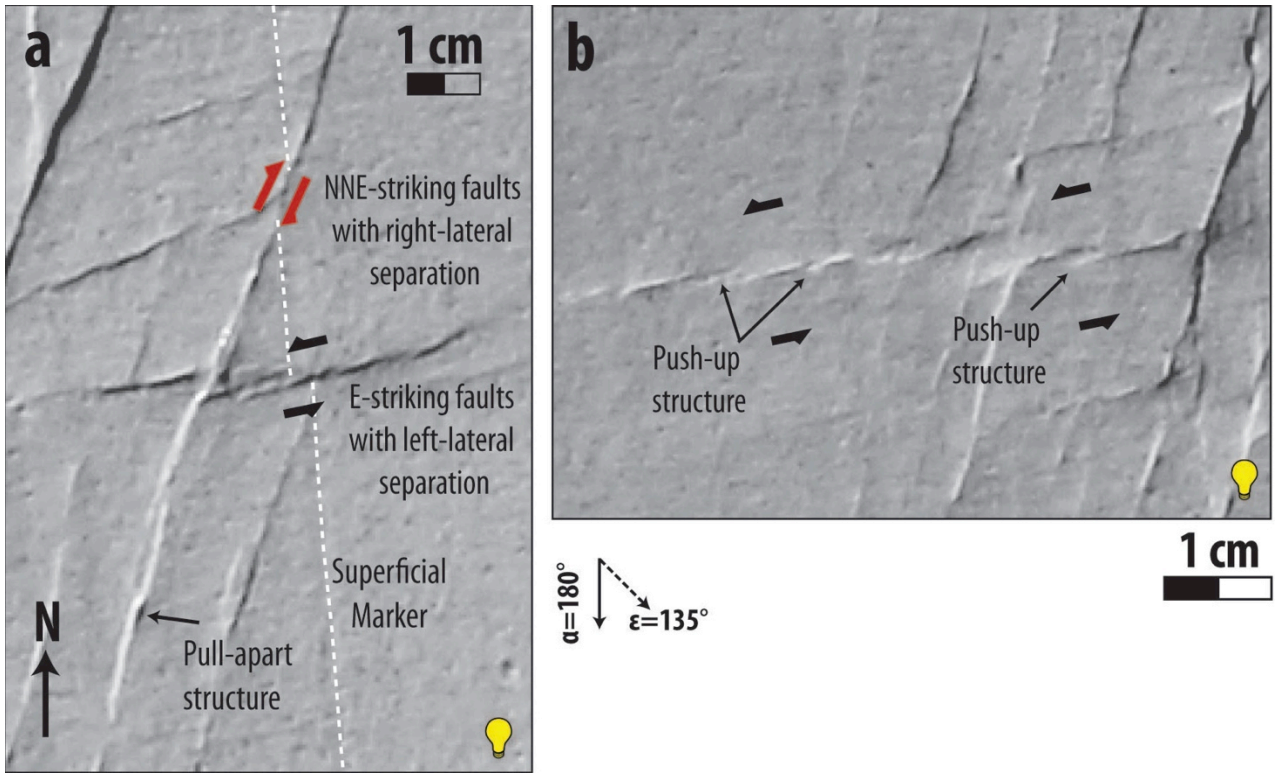

Figure 7. Features used to determine separation and slip sense in Model A. a) Photograph of part of top surface showing NNE-striking fault segments cutting superficial marker (white dashed line) with right-lateral separation, and E-striking fault segments cutting superficial marker with left-lateral separation. Pull-apart structures develop between NNE-striking, right-stepping fault segments, indicating right-lateral strike-slip. Some R-shears cutting R'-shears with right-lateral separation. They also intersect R'-shears. b) Photograph of part of top surface showing push-up structures developing between right-stepping fault segments, indicating left-lateral strike-slip.

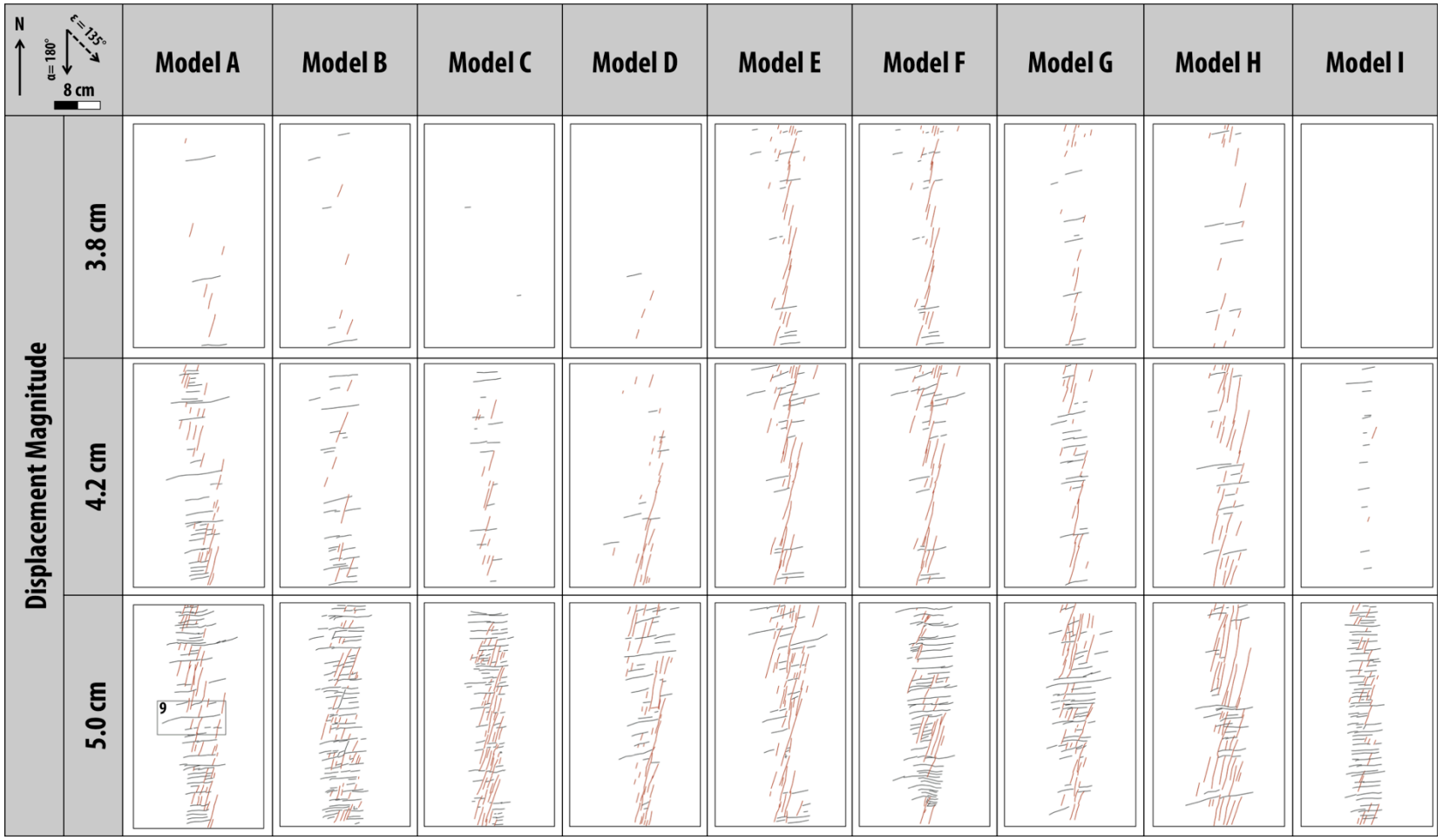

Figure 8. Evolution of Riedel shears during strike-slip phase of deformation for all models. Sides of line drawings are above edges of silicone polymer beneath clay layer. Generally, both R- and R'-shears (red and black lines, respectively), first develop before 4.2 cm of displacement. With further displacement, R-shears link with other R-shears. Some of them cut R'-shears and/or also intersect R'-shears. Rotation and offsets cause some of R'-shears to have curved geometries. Rectangle (Model A) shows area enlarged in Fig. 9.

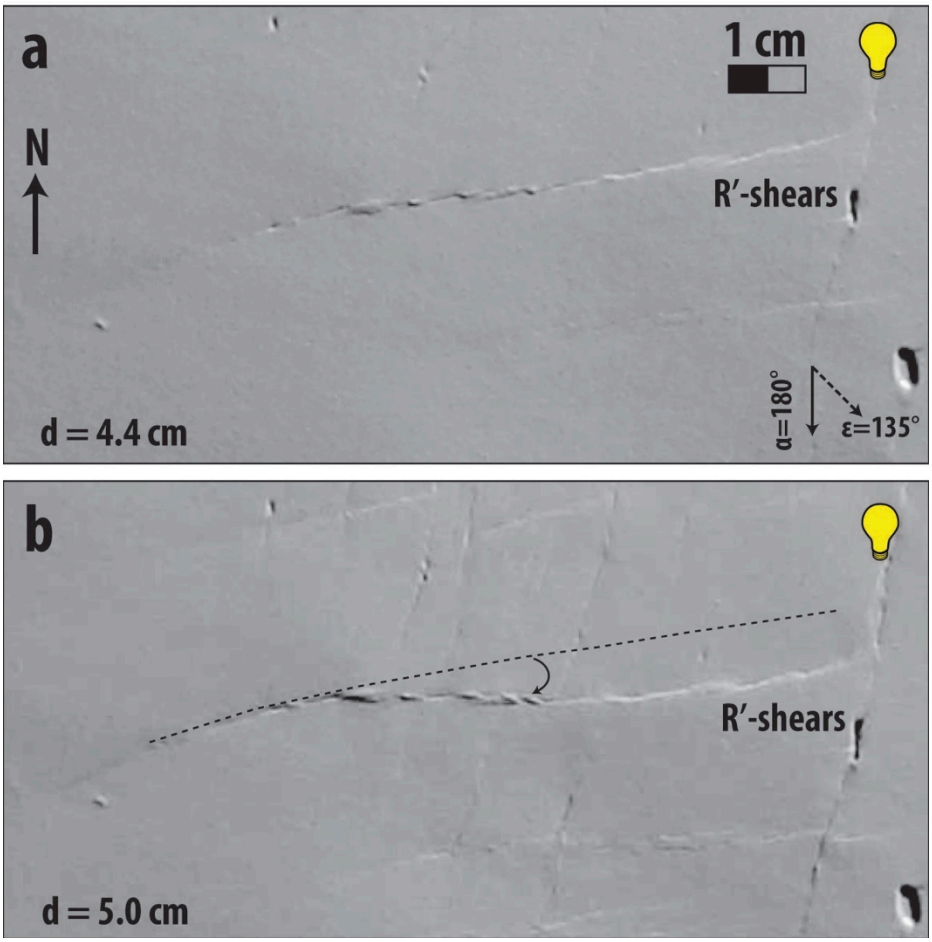

Figure 9. Example of curved geometry of R'-shears in Model A. a) and b) Photographs of part of the top surface at 4.4 cm and 5.0 cm of displacement, respectively. At end of strike-slip phase of deformation, R'-shears rotate clockwise. Dashed line indicates initial location of R'-shears before rotation and subsequent offsets. See Figure 8 for location.

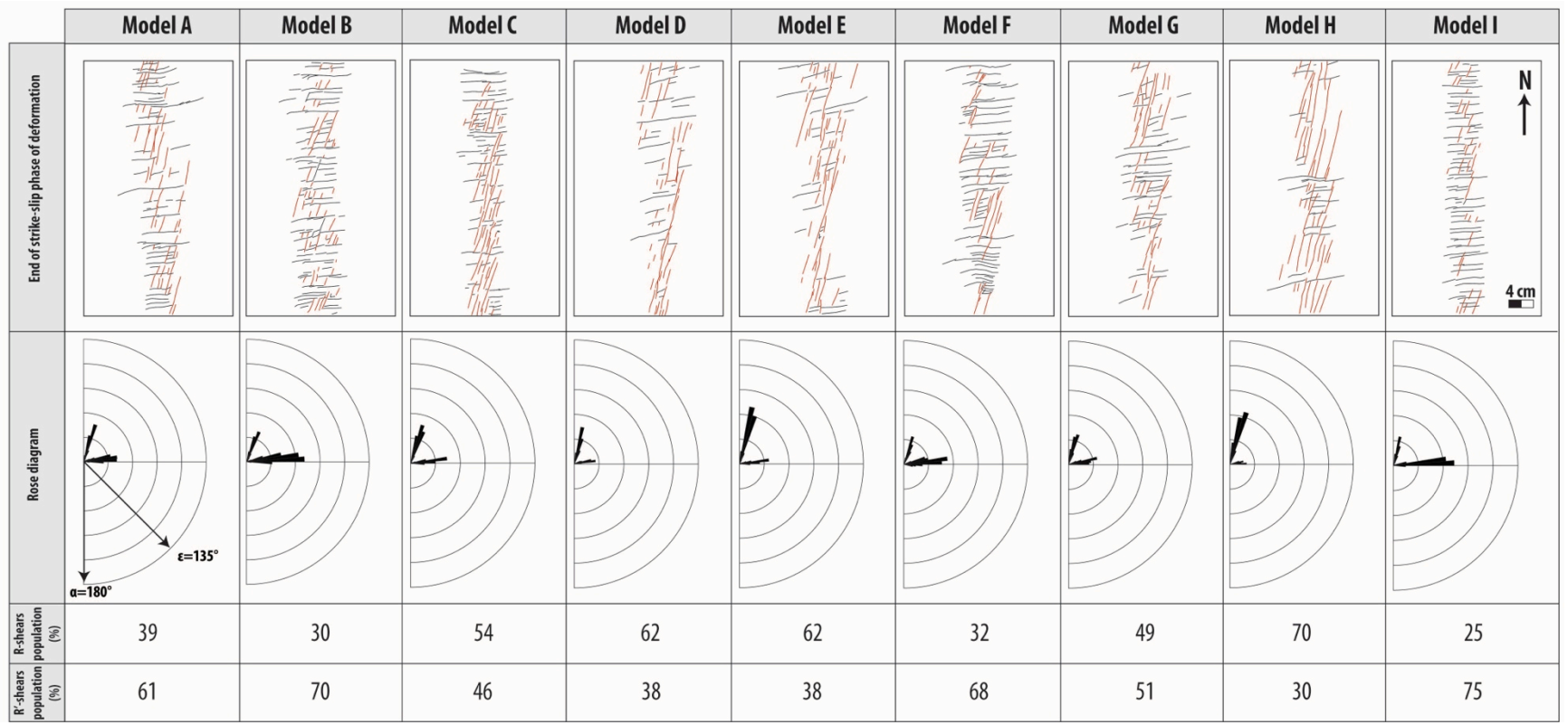

Figure 10. Line drawings of fault patterns in Models A to I at end of strike-slip phase of deformation (d = 5 cm) (top) and rose diagrams showing trends of fault segments (bottom). Bin size for rose diagrams is 5°; outside circle of rose diagrams is 120 cm. Arrows indicate displacement direction (α=180°) and maximum extension direction (ε=135°). All models have identical boundary conditions. Models C and G have approximately percentage of R- and R'-shear segments. Models A, B, F, and I have greater percentage of R'-shear segments, whereas Models D, E, and H have greater percentage of R-shear segments.

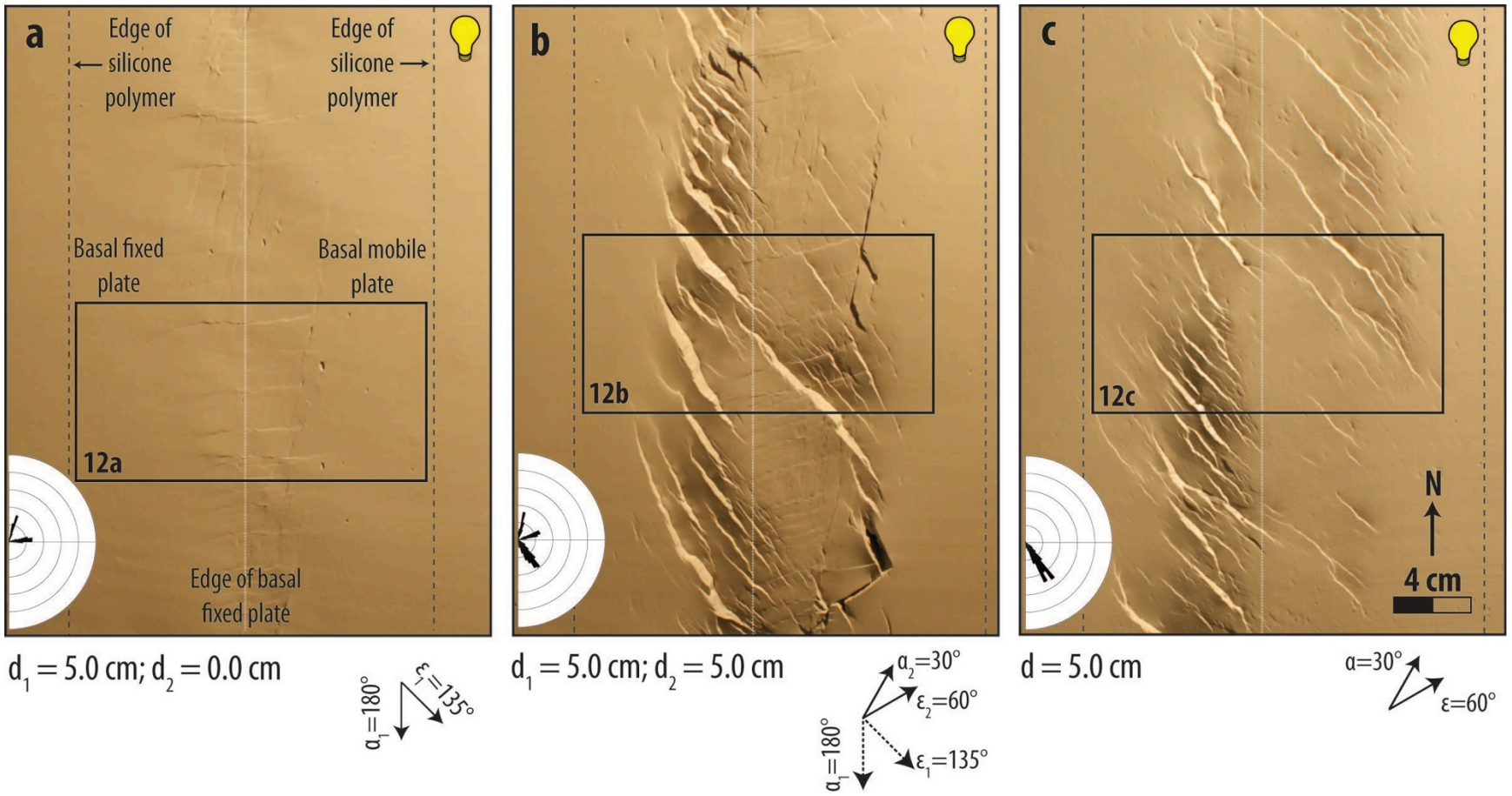

Figure 11. Map-view photograph of top surface of clay layer of Model A and Model A1. a) Model A at end of strike-slip phase of deformation. b) Model A at end of second phase of deformation. c) Model A1 at end of single phase of oblique extension. Fault scarps dipping toward light appear bright; fault scarps dipping away from light appear dark. Rose diagram shows trends of fault segments; bin size for rose diagram is 5°; outside circle of rose diagram is 120 cm. Rectangles show areas enlarged in Fig. 12. Rectangles in Figs. 12a and 12b are not aligned because faults in Fig. 12a move northward during second phase of deformation.

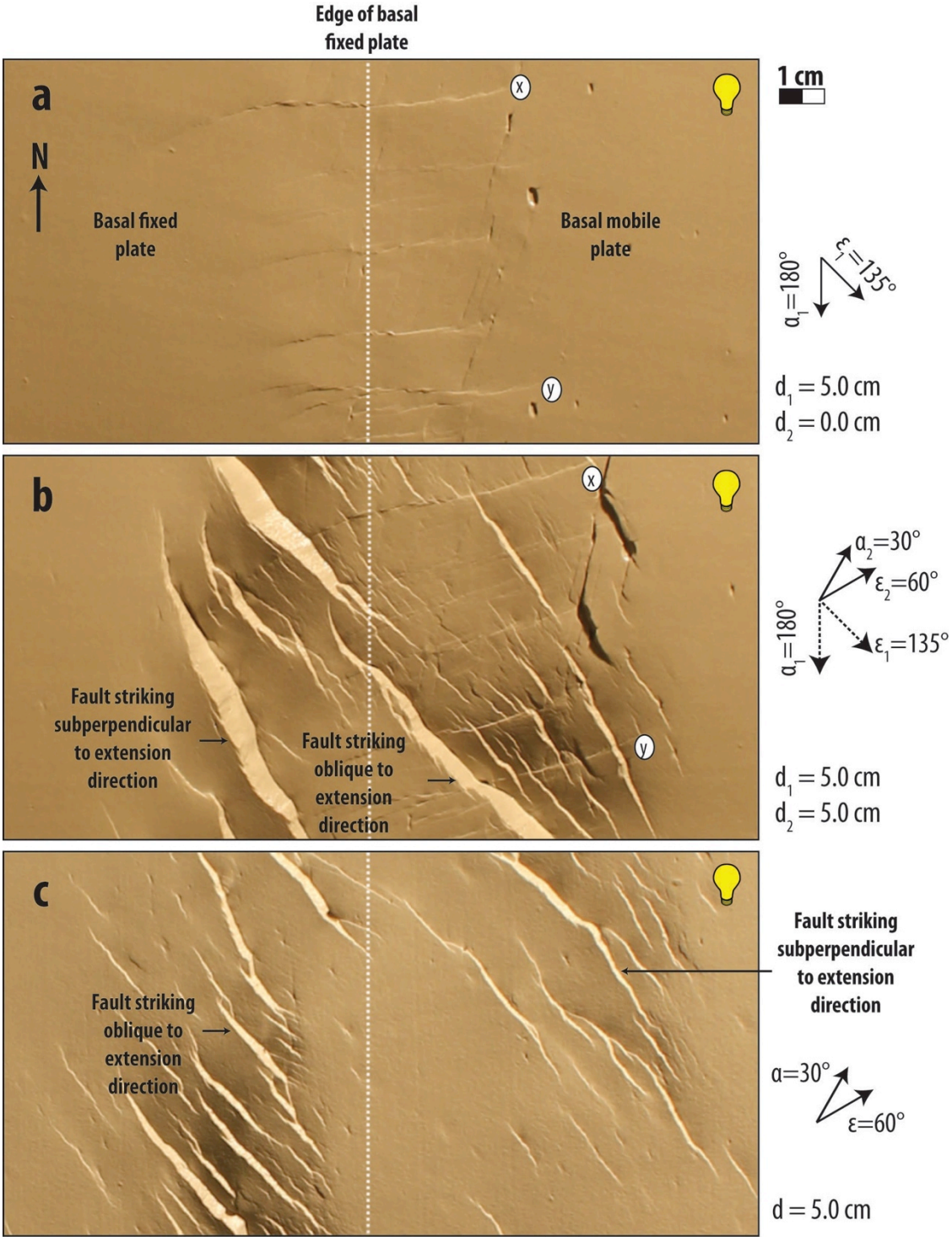

Figure 12. Close-up photographs of parts of Models A and A1 (for location, see Figure 11). a) Riedel shears present at the end of strike-slip phase of deformation in Model A. b) Fault geometry at end of second phase of deformation in Model A. New faults strike subperpendicular or oblique to the extension direction. Faults x and y in part a are Faults x and y in part b. c) Fault geometry at the end of Model A1. Overall, these faults have less displacement than those that form in Model A.

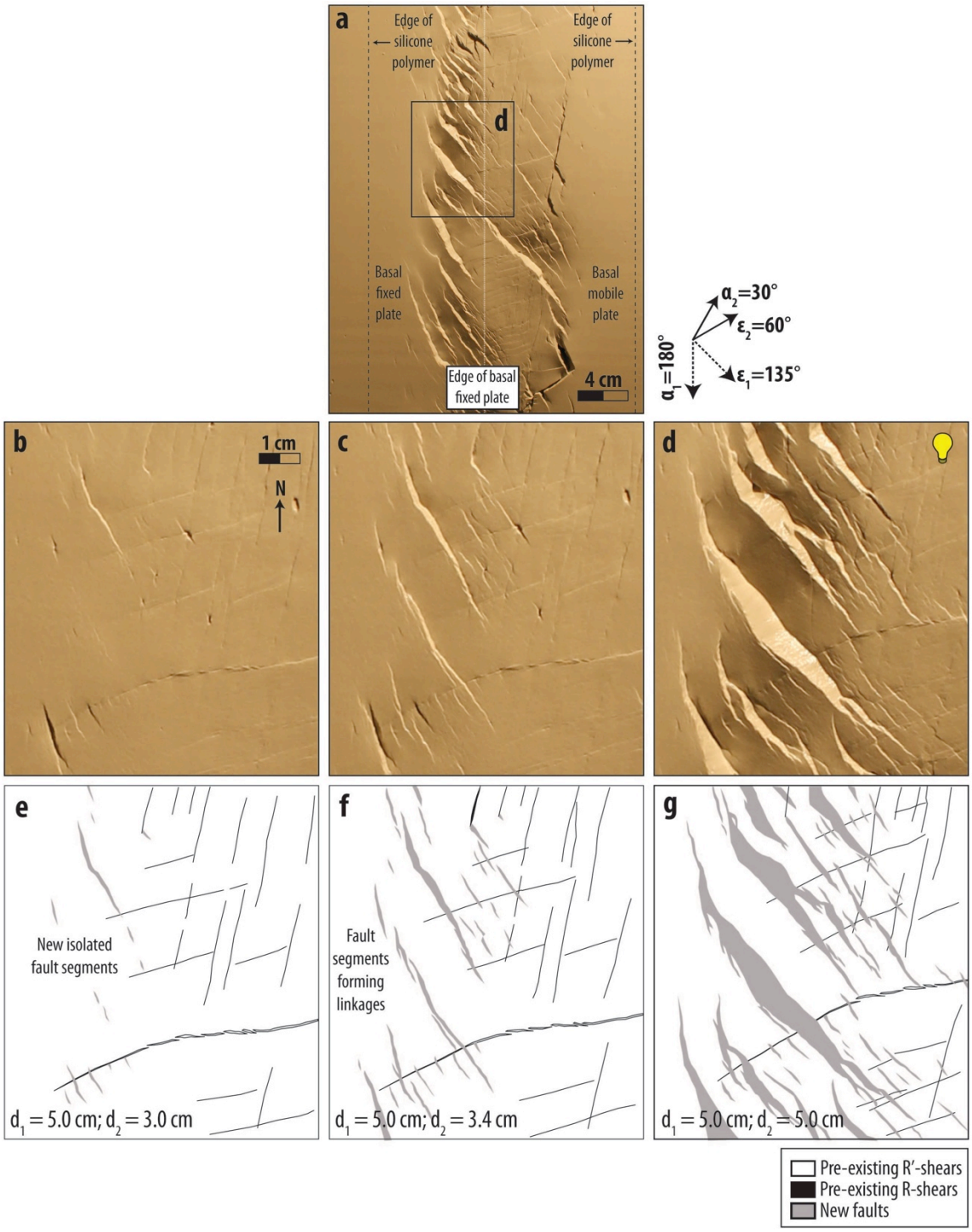

Figure 13. Evolution of faults during second phase of deformation in Model A. a) Photograph of top surface of Model A at 5.0 cm of displacement. Rectangle shows area enlarged in part d. b) to d) Uninterpreted photographs of part of top surface of Model A at 3 cm, 3.4 cm, and 5 cm of displacement, respectively. Fault scarps dipping toward light appear bright; fault scarps dipping away from light appear dark. e) to g) Line drawing of select faults. New faults initially form as isolated segments and propagate away from them. They lose displacement after cutting across R'-shears.

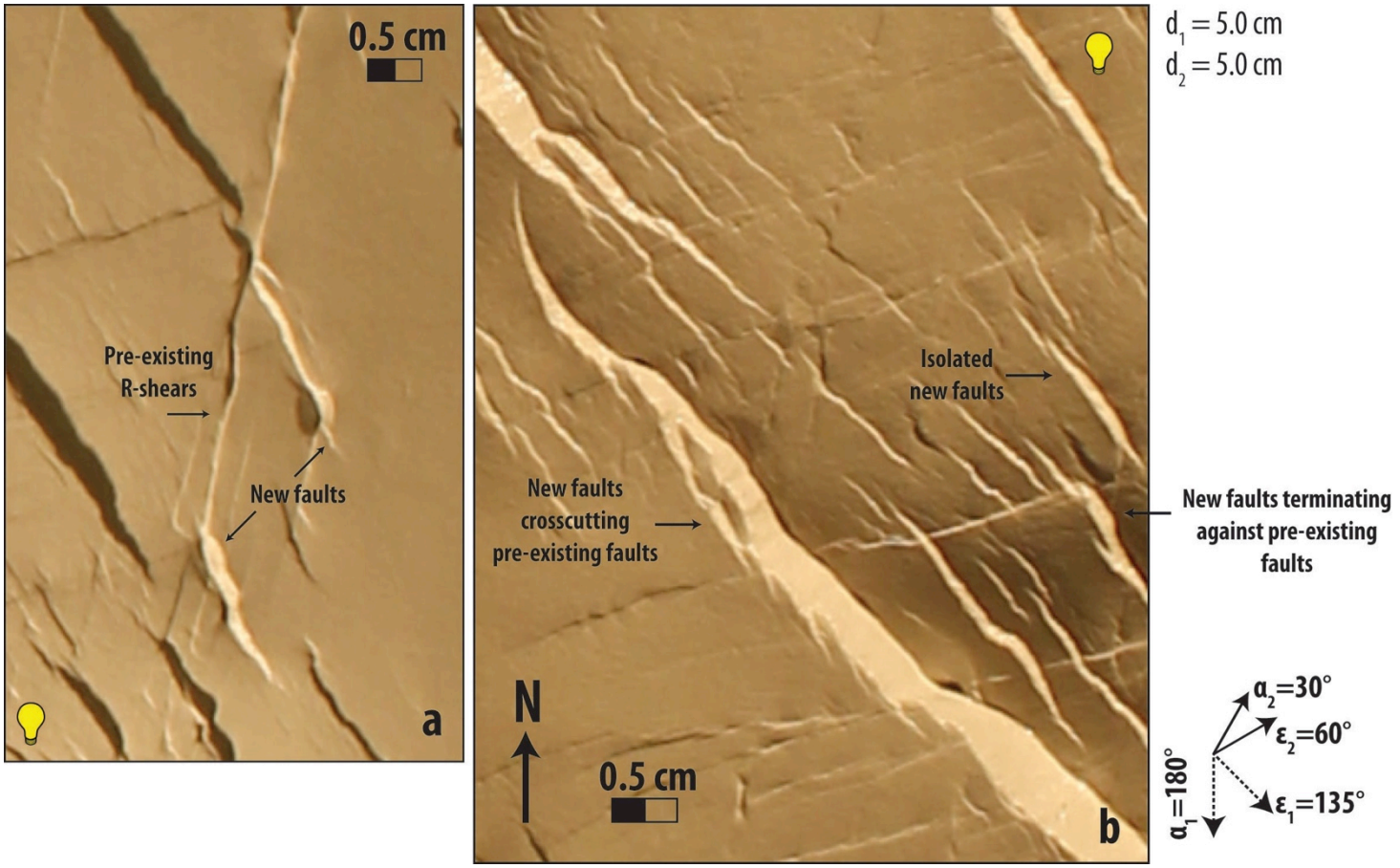

Figure 14. Examples of fault interactions in Model A. Photographs at end of second phase of deformation showing: a) pre-existing R-shears becoming sites of nucleation of new faults, and b) new faults cutting across and/or terminating at pre-existing faults, and others never encounter them. Fault scarps dipping toward light appear bright; fault scarps dipping away from light appear dark. The lighting direction is different in a and b.

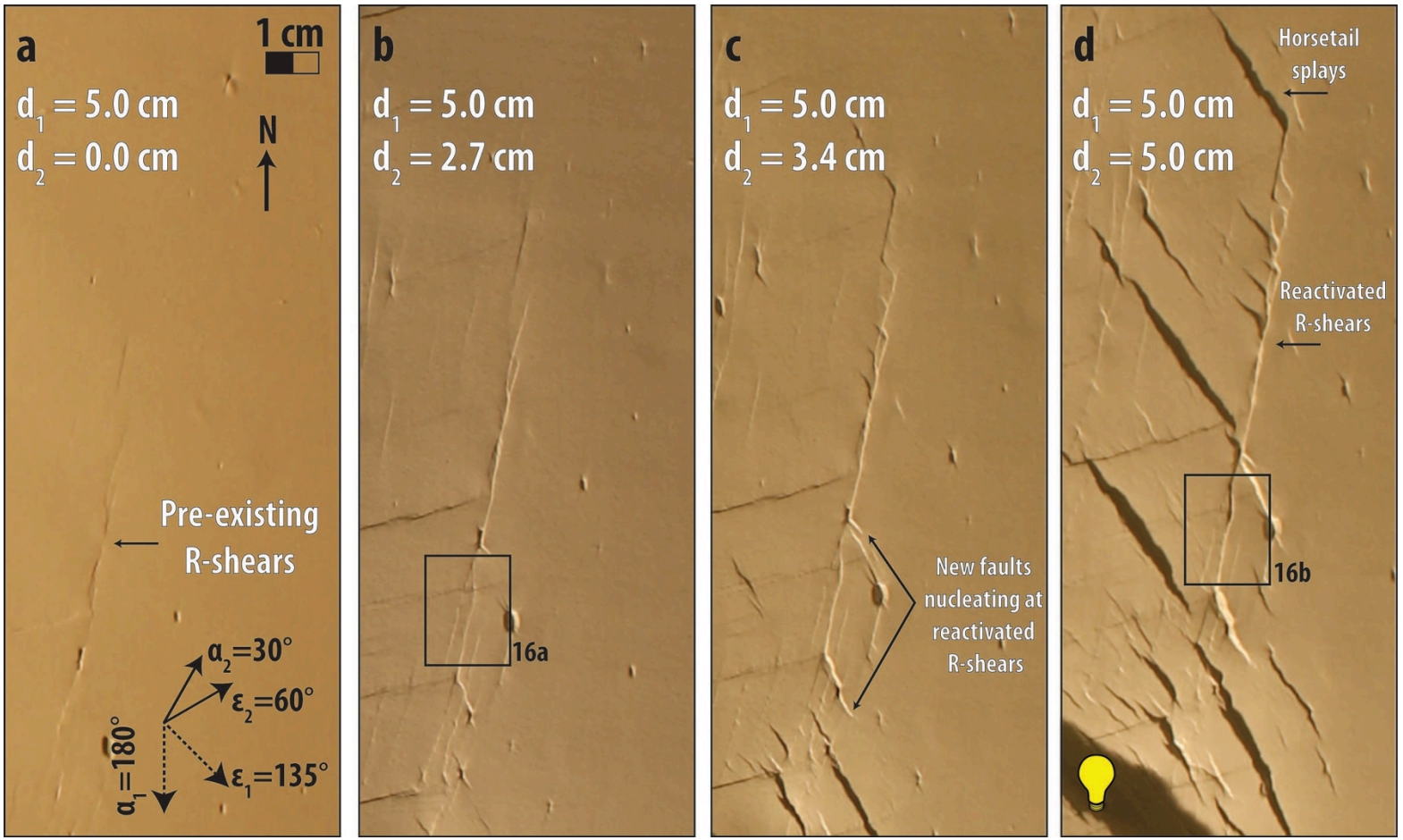

Figure 15. Reactivation of R-shears during second phase of deformation in Model A. a), b), c) and d) Photographs of part of top surface at 0 cm, 2.7 cm, 3.4 cm, and 5 cm of displacement, respectively. R-shears continue to propagate as deformation progresses. Horsetail splays and new faults nucleate at reactivated R-shears. Fault scarps dipping toward light appear bright; fault scarps dipping away from light appear dark. Rectangle shows area enlarged in Fig. 16.

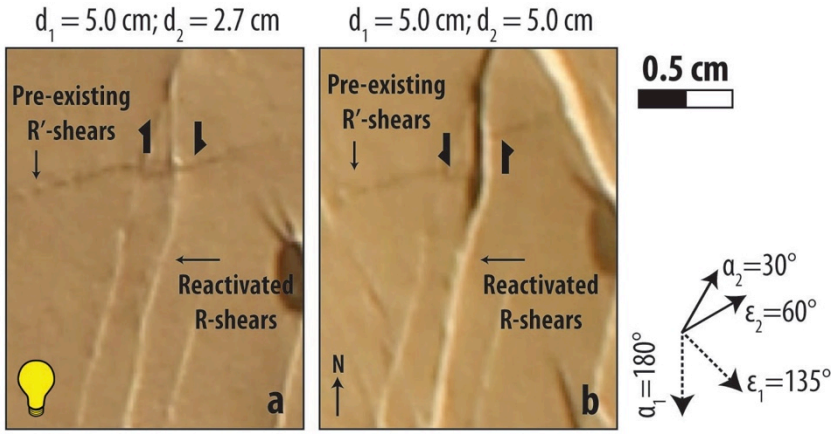

Figure 16. Reactivation of R-shears in Model A (for location, see Figure 15). a) and b) Photographs of part of top surface of Model A at 2.7 cm and 5.0 cm of displacement showing pre-existing R-shear with right-lateral separation (part a) but left-lateral separation by end of second phase of deformation. Fault scarps dipping toward light appear bright; fault scarps dipping away from light appear dark.

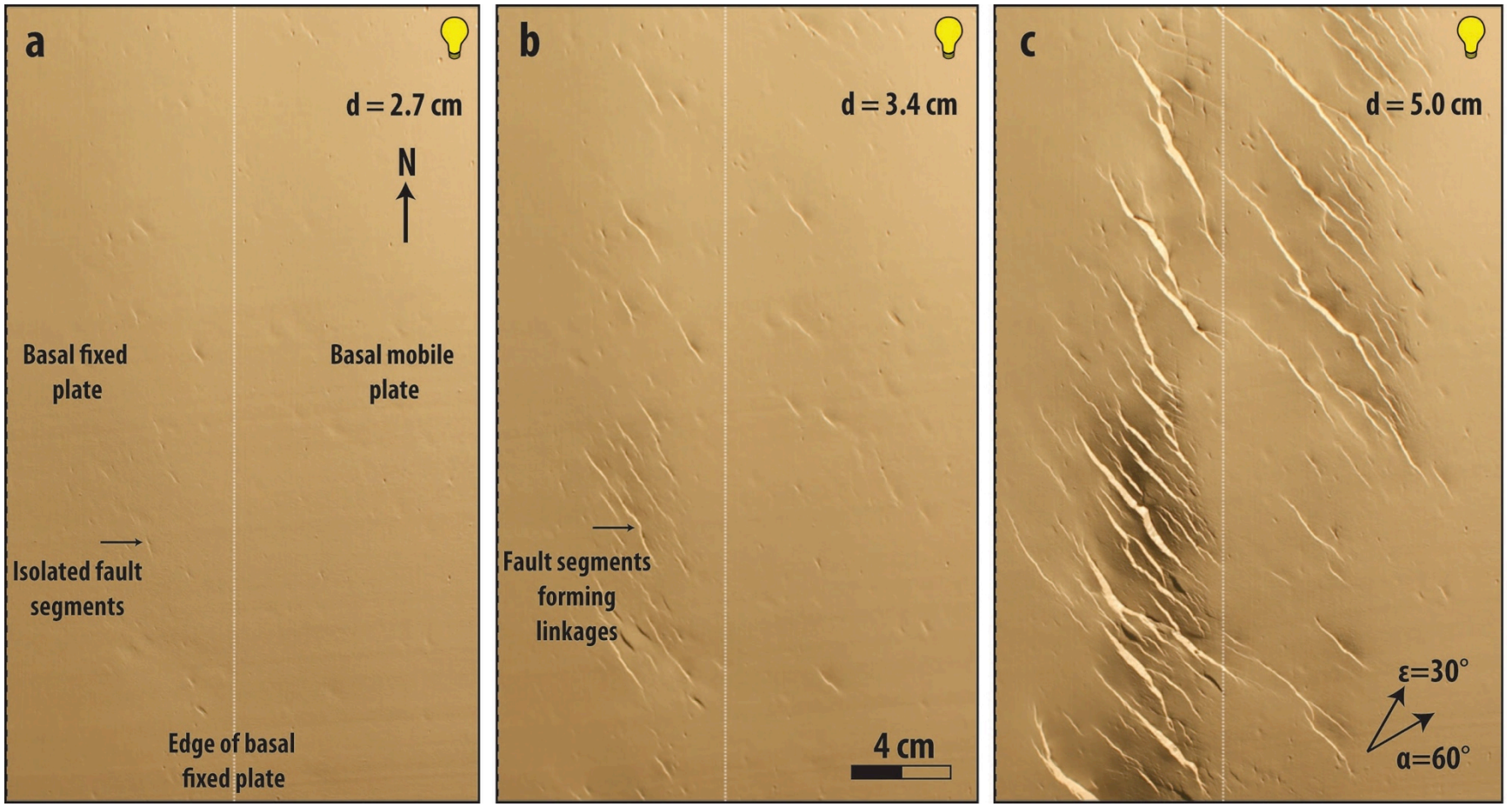

Figure 17. Evolution of faults during single phase of oblique extension in Model A1. a), b), and c) Map-view photographs of top surface of Model A1 at 2.7 cm, 3.4 cm, and 5 cm of displacement, respectively. Their strike is 130° to 160° relative to the long axis of deformation. Sides of photographs are above outer edges of silicone polymer. Fault scarps dipping toward light appear bright; fault scarps dipping away from light appear dark.

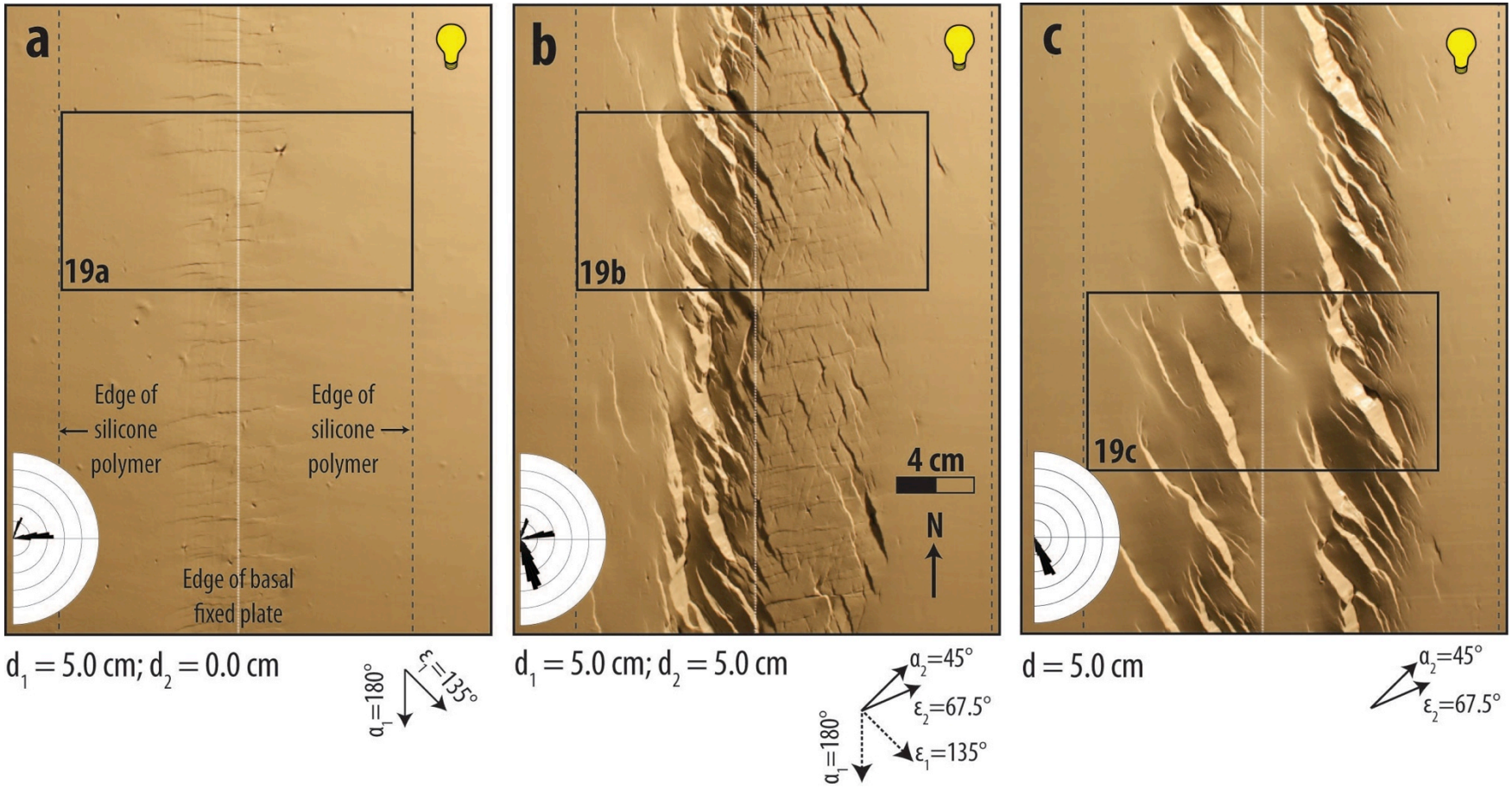

Figure 18. Map-view photograph of top surface of clay layer of Model B and Model B1. a) Model B at end of strike-slip phase of deformation. b) Model B at end of second phase of deformation. c) Model B1 at end of single phase of oblique extension. Fault scarps dipping toward light appear bright; fault scarps dipping away from light appear dark. Rose diagram shows trends of fault segments; bin size for rose diagram is 5°; outside circle of rose diagram is 120 cm. Rectangles show areas enlarged in Fig. 19.

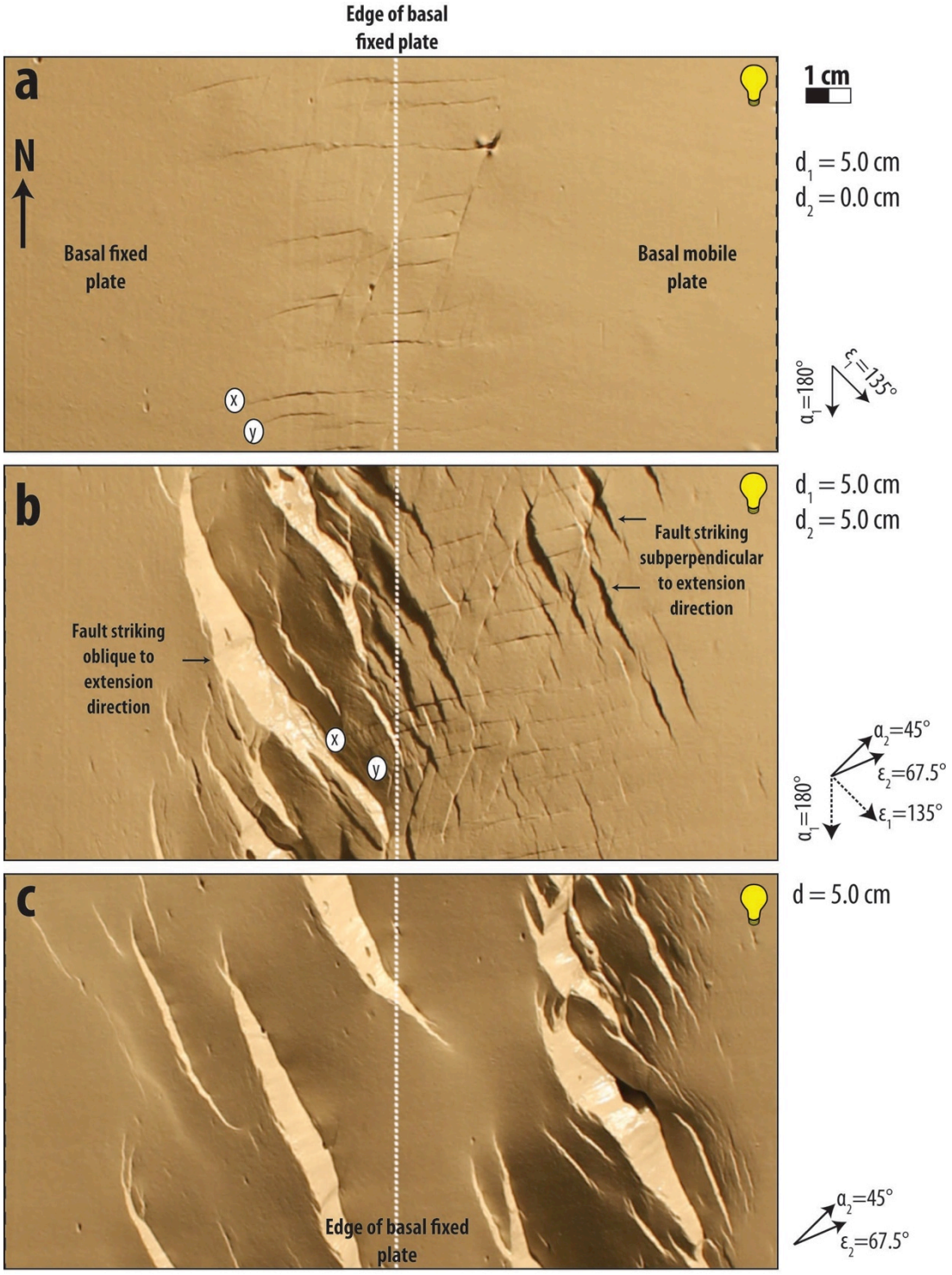

Figure 19. Close-up photographs of parts of Models B and B1 (for location, see Figure 18). a) Riedel shears present at the end of strike-slip phase of deformation in Model B. b) Fault geometry at end of second phase of deformation in Model B. New faults strike subperpendicular or oblique to the extension direction. Faults x and y in part a are Faults x and y in part b. c) Fault geometry at end of Model B1. Faults in Model B1 are similar to those that form where pre-existing fault population is less developed in Model B. Fault scarps dipping toward light appear bright; fault scarps dipping away from light appear dark.

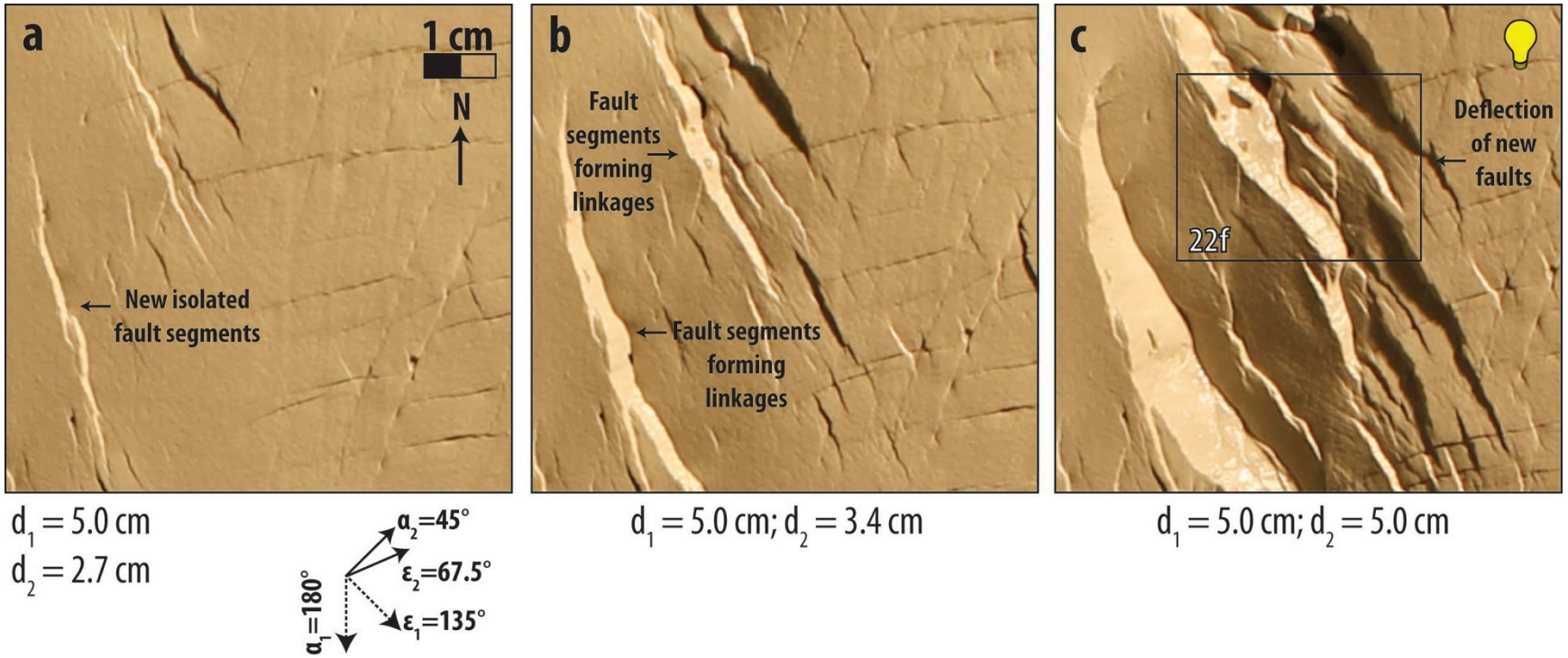

Figure 20. Evolution of faults during second phase of deformation in Model B. a) to c) Photographs of part of top surface at 2.7, 3.4 cm and 5 cm of displacement, respectively. New faults initially form as segments and subsequently link together. They are eventually deflected as they encounter pre-existing R'-shears (part c). Fault scarps dipping toward light appear bright; fault scarps dipping away from light appear dark. Rectangle shows area enlarged in Fig. 22.

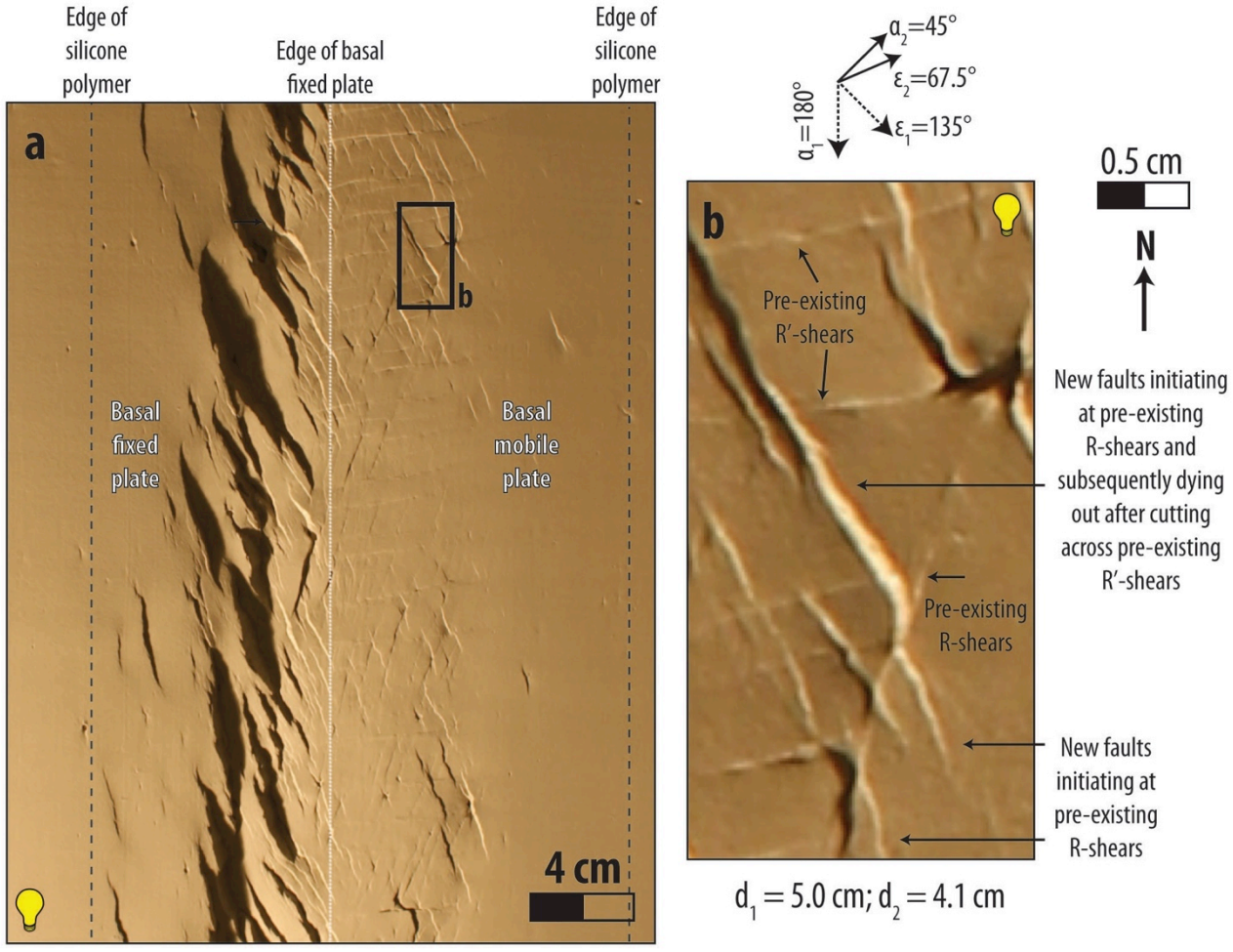

Figure 21. Example of fault interaction during second phase of deformation in Model B. a) Photograph of top surface at 4.1 cm of displacement. Rectangle shows are enlarged in part b. b) Photograph of part of top surface at 4.1 cm of displacement. New faults, which initiated at pre-existing R-shears, cut across pre-existing R'-shears and eventually die out. Fault scarps dipping toward light appear bright; fault scarps dipping away from light appear dark.

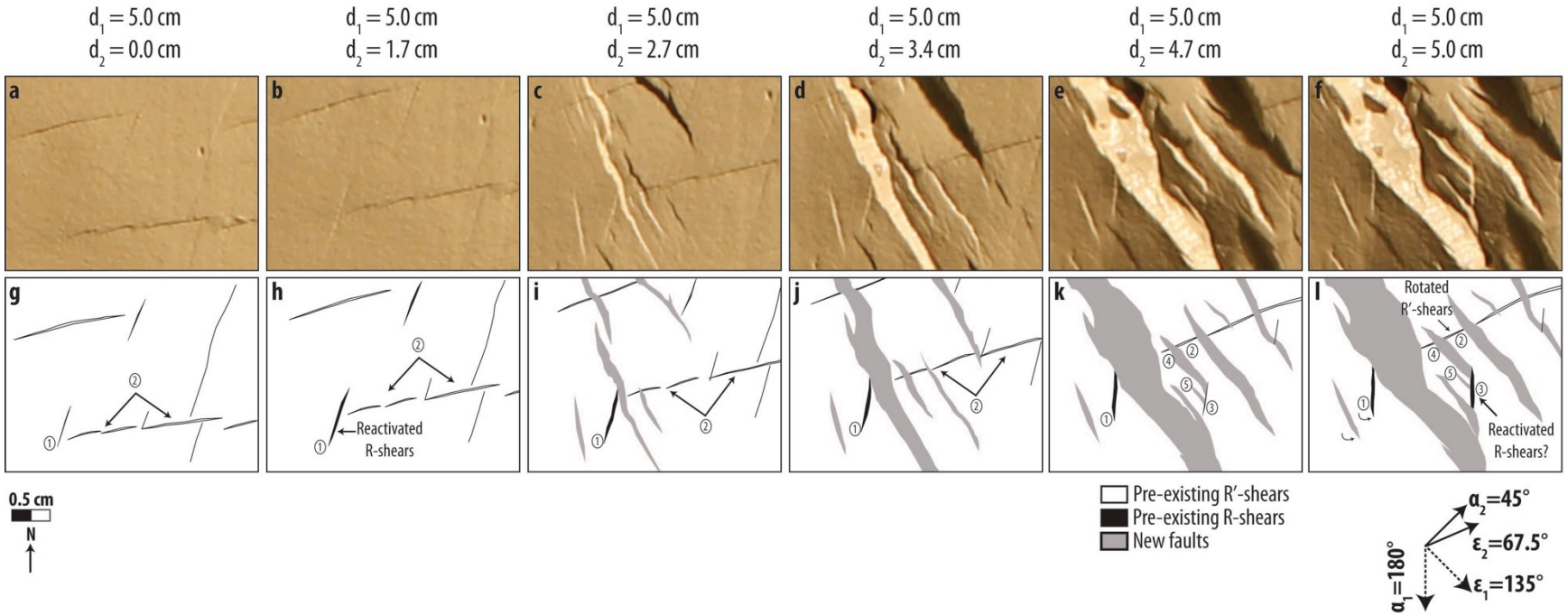

Figure 22. Reactivation and rotation of some pre-existing faults in Model B during second phase of deformation. a) to f) Uninterpreted photographs of part of top surface at 0 cm, 1.7 cm, 2.7 cm, 3.4 cm, 4.7 cm, and 5 cm of displacement, respectively (for location, see Figure 20). Fault scarps dipping toward light appear bright; fault scarps dipping away from light appear dark. g) to l) Line drawings of select faults. Fault 1 is an example of pre-existing R-shear that is more pronounced with slightly more dip-slip component as the experiment progresses. It also rotates counterclockwise. Fault 2 is an example of pre-existing R'-shears that shift northward and rotate counterclockwise relative to the long axis of deformation zone. Fault 3 is an example of fault that did not appear on the clay surface at the end of the strike-slip phase, but propagated to the surface during the latter stage of the second phase of deformation. According to its strike, Fault 3 is possibly a reactivated R-shear. Faults 4 and 5 terminate against Fault 3.

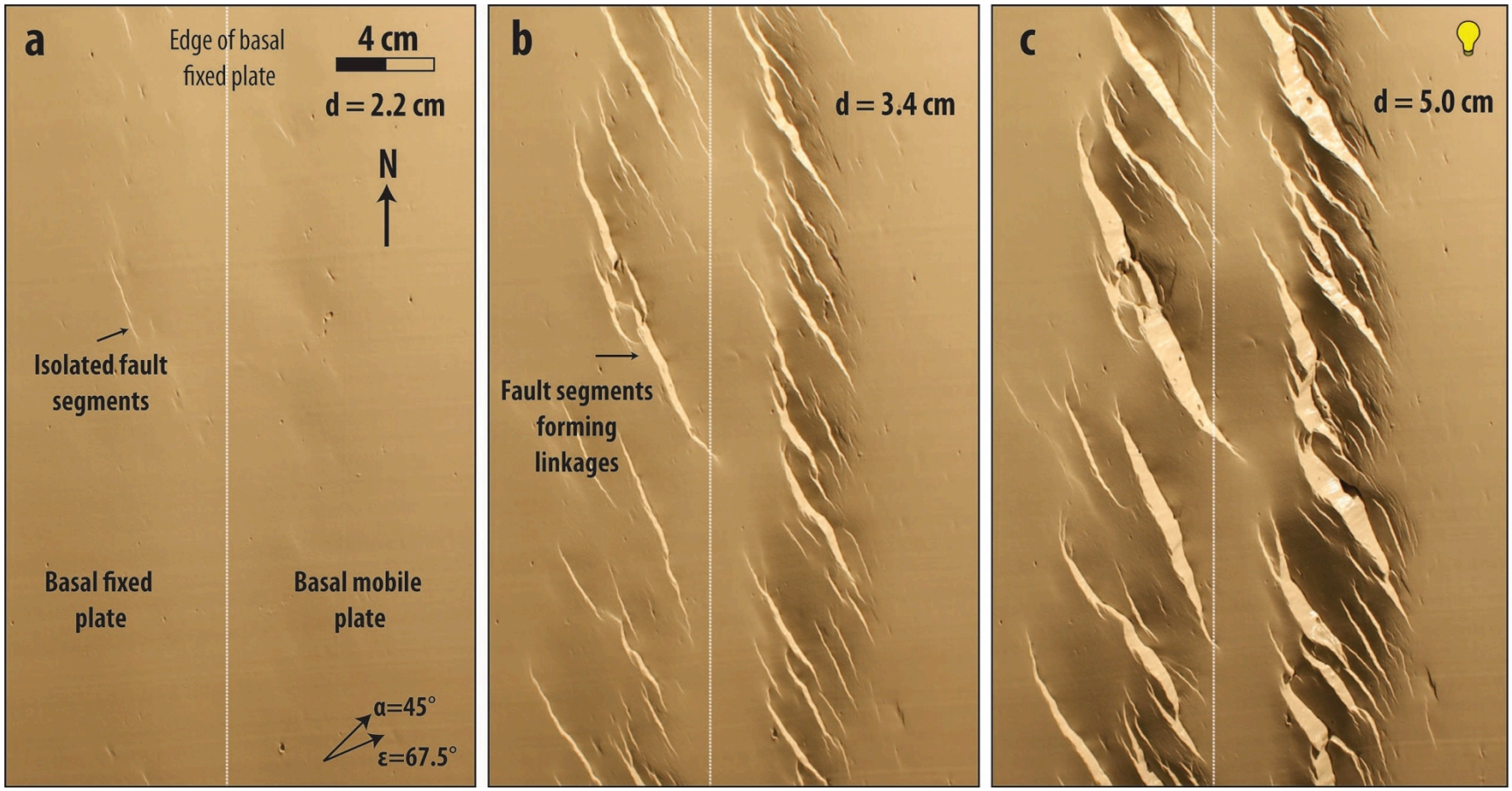

Figure 23. Evolution of faults during single phase of oblique extension in Model B1. a), b), and c) Map-view photographs of top surface of at 2.2 cm, 3.4 cm, and 5 cm of displacement, respectively. Fault scarps dipping toward light appear bright; fault scarps dipping away from light appear dark. Their strike is 140° to 170° relative to the long axis of deformation. Sides of photographs are above outer edges of silicone polymer.

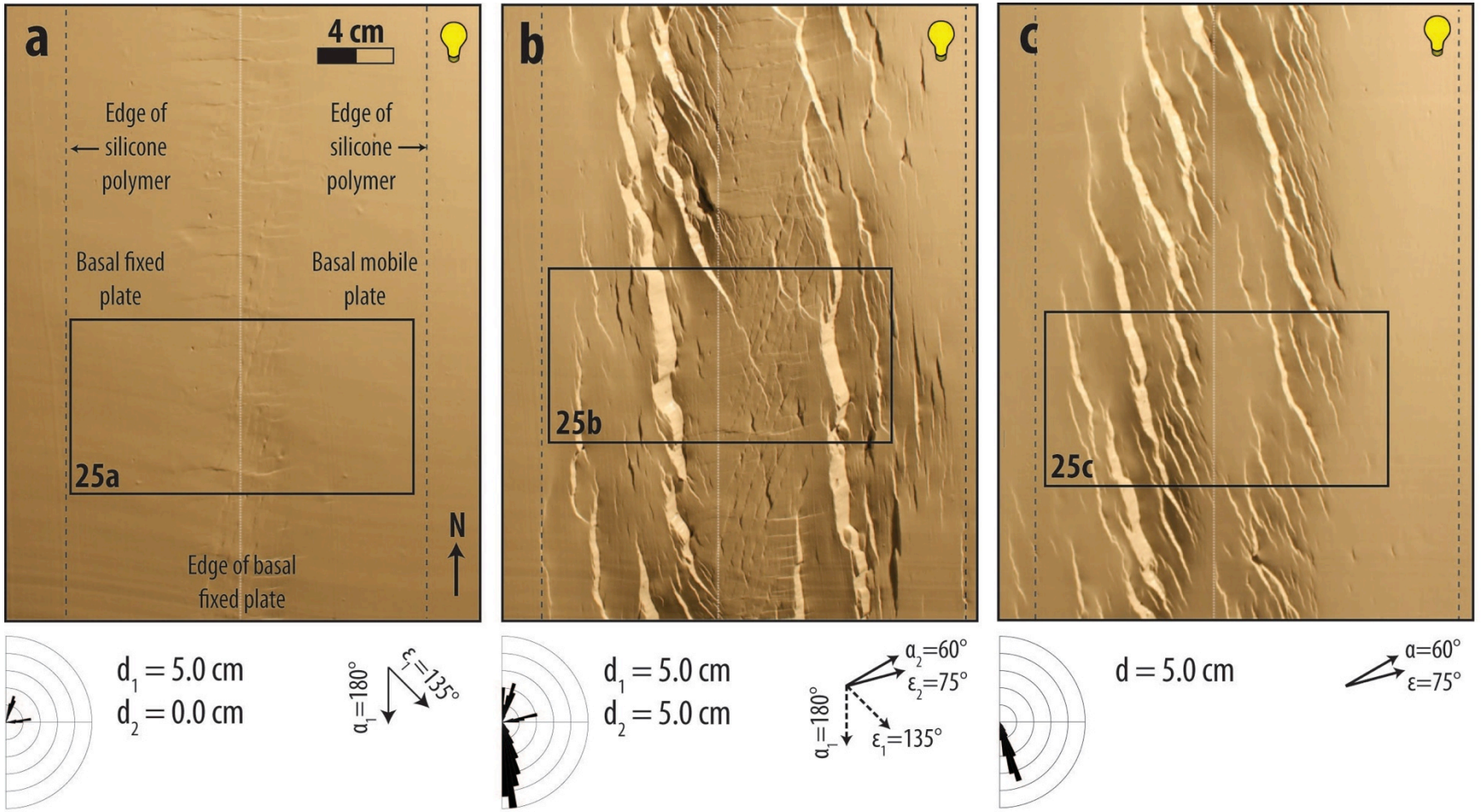

Figure 24. Map-view photograph of top surface of clay layer of Model C and Model C1. a) Model C at end of strike-slip phase of deformation. b) Model C at end of second phase of deformation. c) Model C1 at end of single phase of oblique extension. Fault scarps dipping toward light appear bright; fault scarps dipping away from light appear dark. Rose diagram shows trends of fault segments; bin size for rose diagram is 5°; outside circle of rose diagram is 120 cm. Rectangles show areas enlarged in Fig. 25.

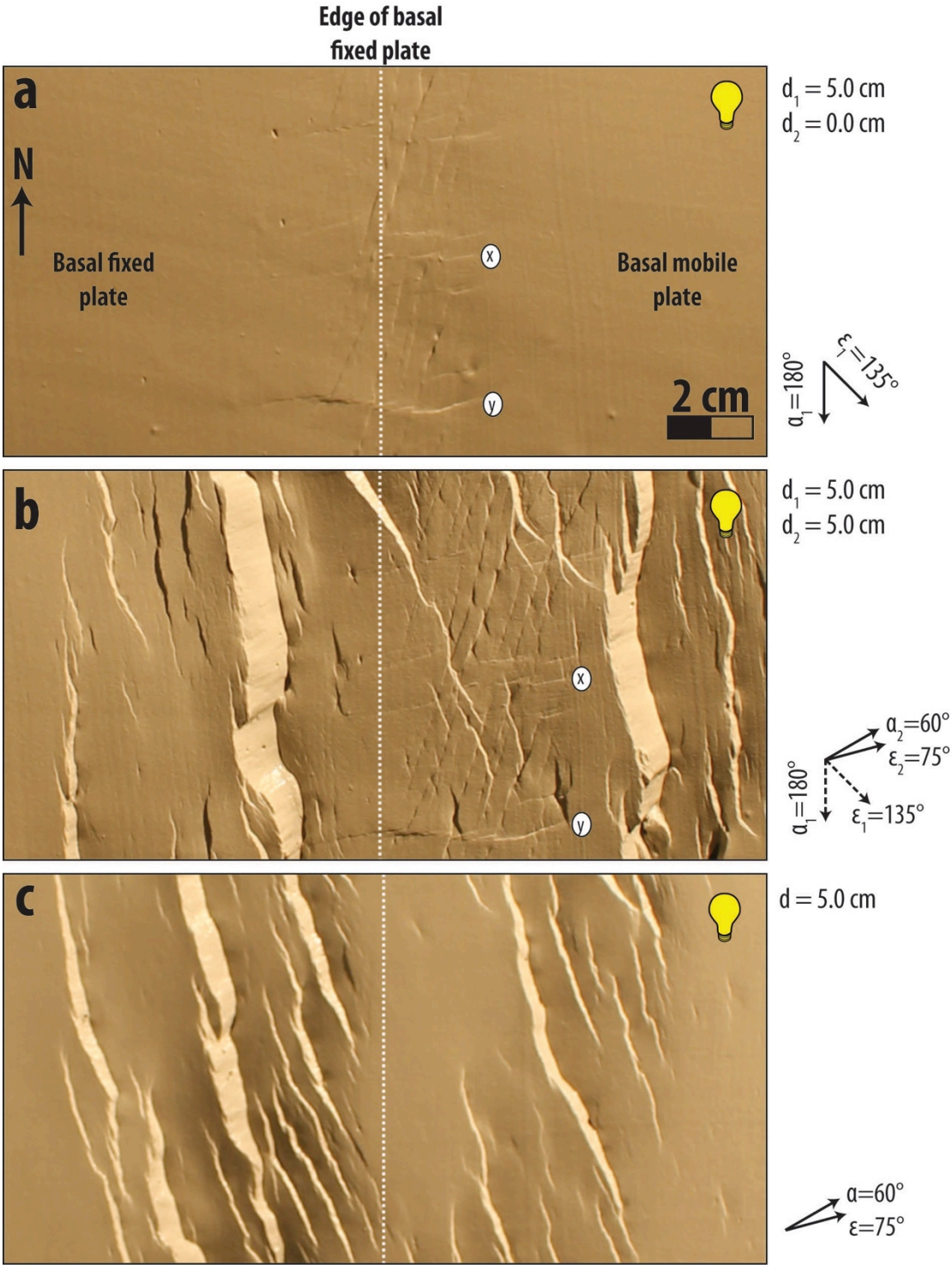

Figure 25. Close-up photographs of parts of Models C and C1 (for location, see Figure 24). a) Riedel shears present at the end of strike-slip phase of deformation in Model C. b) Fault pattern at end of Model C. Pre-existing faults serve as barriers for propagation of new faults. New faults lose displacement as they enter pre-existing deformed zone. For reference for location of pre-existing faults at end of second phase of deformation, use Faults x and y. c) Fault geometry at end of Model C1. Fault scarps dipping toward light appear bright; fault scarps dipping away from light appear dark.

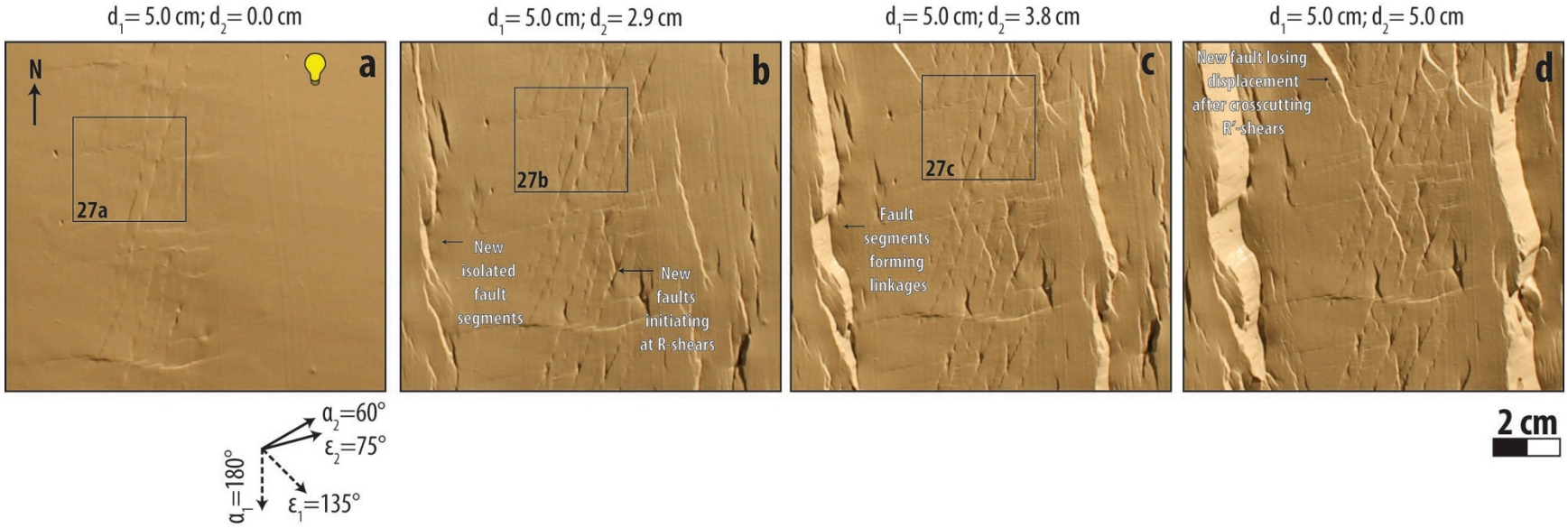

Figure 26. Evolution of faults during second phase of deformation in Model C. a), b), c), and d) Photographs of smaller part of area shown in Fig. 25 at 0 cm, 2.9 cm, 3.8 cm, and 5 cm of displacement, respectively. New faults initially form as isolated segments before linking together. They develop away from pre-existing faults and lose displacement as they enter first-phase deformed zone. Others nucleate at R-shears and terminate after cutting across R'-shears. Fault scarps dipping toward light appear bright; fault scarps dipping away from light appear dark. Rectangles show areas enlarged in Figure 27.

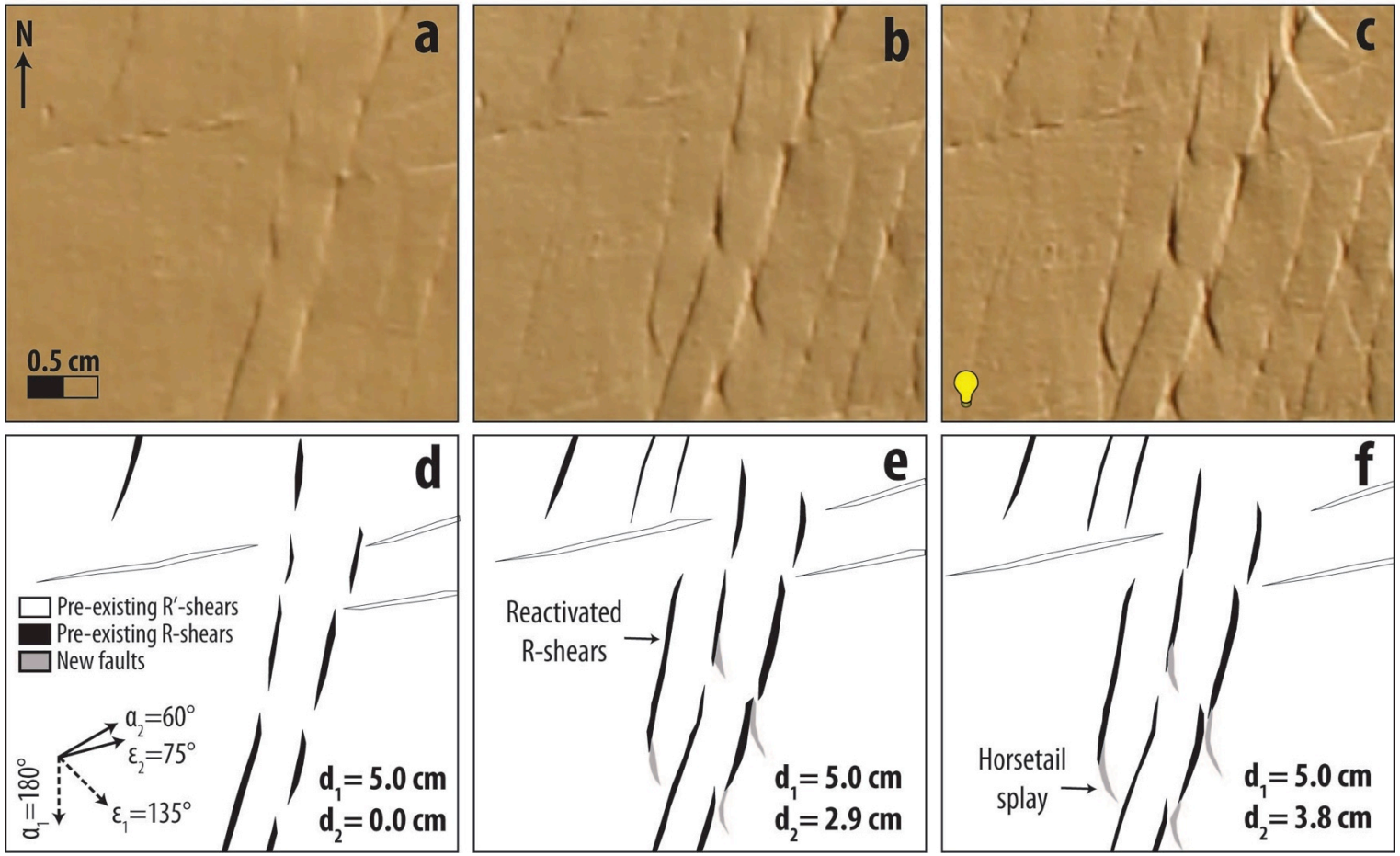

Figure 27. Reactivation of pre-existing R-shears during second phase of deformation (for location, see Figure 26). a), b), and c) Photographs of part of top surface of Model C during second phase of deformation at 0 cm, 2.9 cm, and 3.8 cm of displacement, respectively. d, e, and, f) Line drawings of select faults. New faults nucleate at pre-existing R-shears. Other R-shears, which did not appear on surface at end of first phase, propagate to surface during second phase of deformation, indicating reactivation of these faults with dip-slip component. Moreover, horsetail splays on R-shears also suggest reactivation with left-lateral strike-slip. Fault scarps dipping toward light appear bright; fault scarps dipping away from light appear dark.

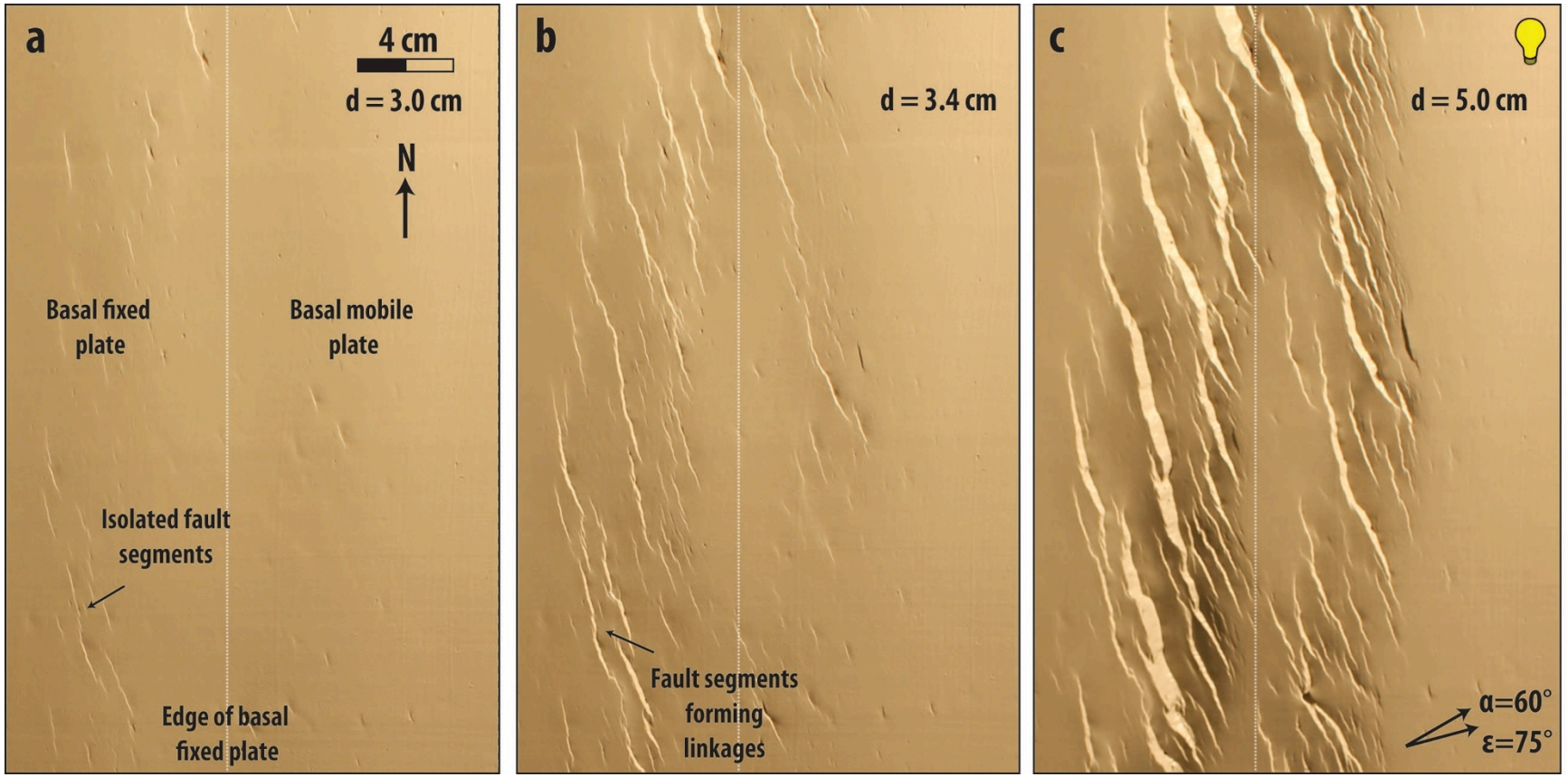

Figure 28. Evolution of faults during single phase of oblique extension in Model C1. a), b), and c) Map-view photographs of top surface at 3.0 cm, 3.4 cm, and 5 cm of displacement, respectively. Fault scarps dipping toward light appear bright; fault scarps dipping away from light appear dark. Their strike is 155° to 175° relative to the long axis of deformation. Sides of photographs are above outer edges of silicone polymer.

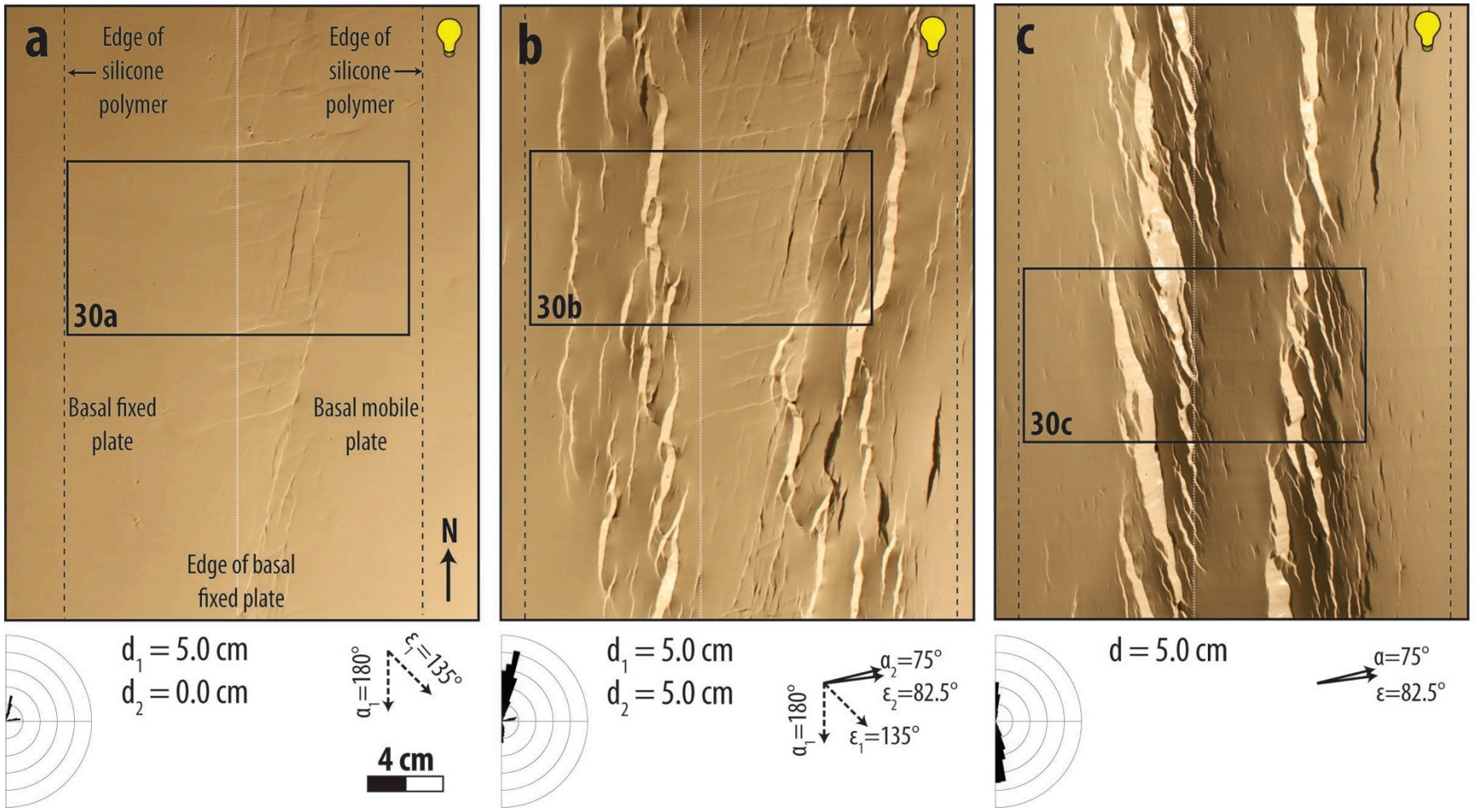

Figure 29. Map-view photographs of top surface of clay layer of Model D and Model D1. a) Model D at end of strike-slip phase of deformation. b) Model D at end of second phase of deformation. c) Model D1 at end of single phase of oblique extension. Fault scarps dipping toward light appear bright; fault scarps dipping away from light appear dark. Rose diagram shows trends of fault segments; bin size for rose diagram is 5°; outside circle of rose diagram is 120 cm. Arrow indicates the maximum extension direction. Rectangles show areas enlarged in Fig. 30.

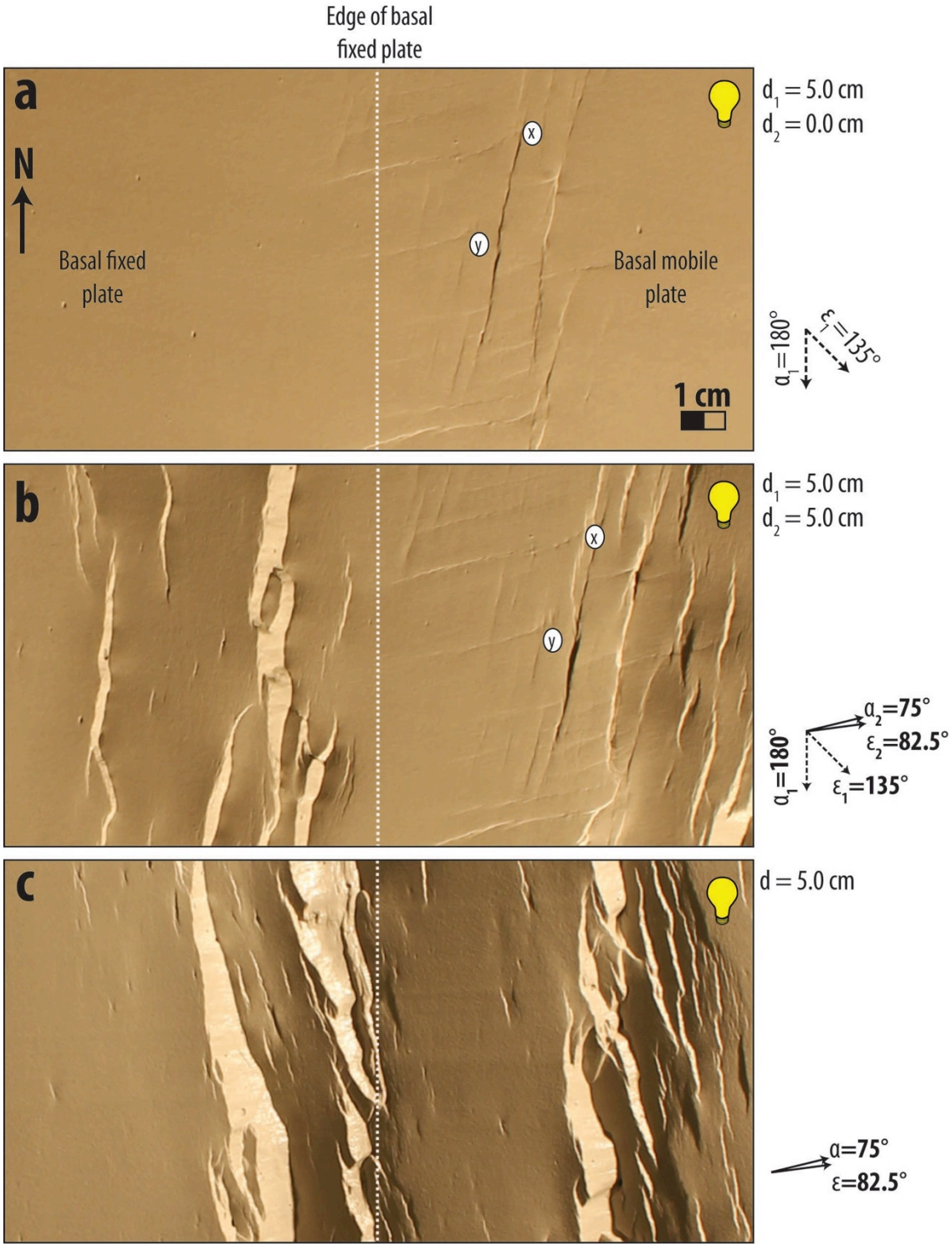

Figure 30. Close-up photographs of parts of Models D and D1 (for location, see Figure 29). a) Riedel shears present at the end of strike-slip phase of deformation in Model D. b) Fault pattern at end of Model D. Very few new faults appear where pre-existing faults are well developed. Their strike is slightly oblique to extension direction. For reference for location of pre-existing faults at end of second phase of deformation, use Faults x and y. c) Fault geometry at end of Model D1. Their strike is subperpendicular to extension direction. Dotted white line represents edge of basal fixed plates. Fault scarps dipping toward light appear bright; fault scarps dipping away from light appear dark.

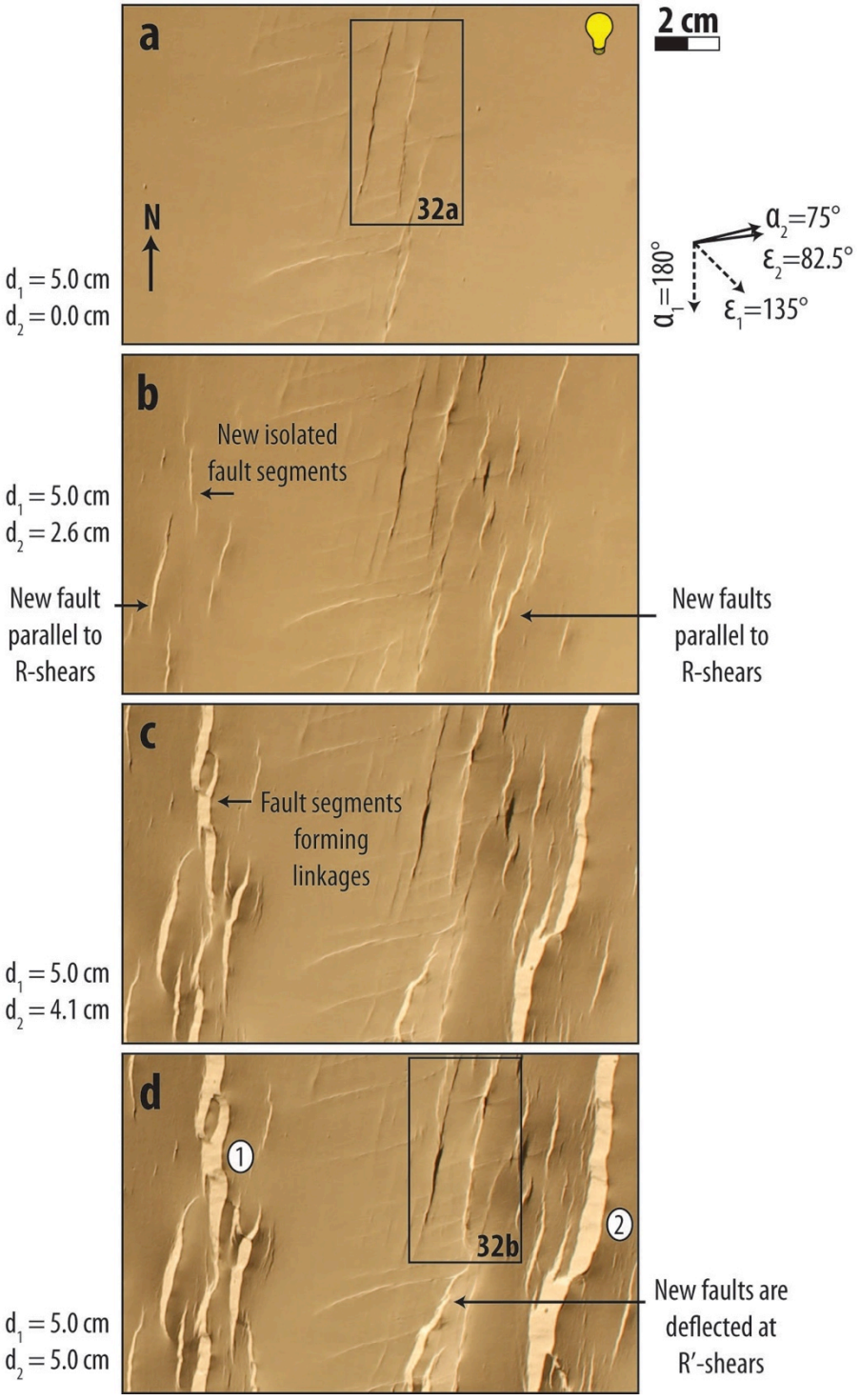

Figure 31. Evolution of faults during second phase of deformation in Model D. a) to d) Photographs of part of top surface at 0.0 cm, 2.6 cm, 4.1 cm, and 5.0 cm of displacement, respectively. New faults initially form as isolated segments and link together. They have same strike as R-shears. Faults 1 and 2 are examples of new faults that are not associated with any observable pre-existing R-shears. Fault scarps dipping toward light appear bright; fault scarps dipping away from light appear dark. Rectangles show areas enlarged in Fig. 32.

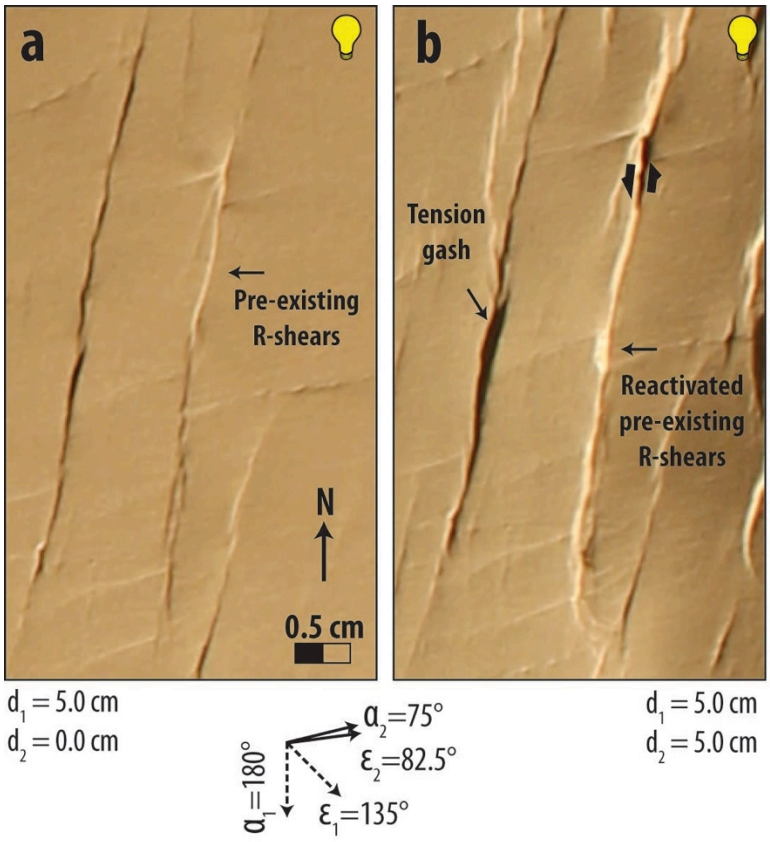

Figure 32. Reactivation of pre-existing R-shears during second phase of deformation (for location, see Figure 31). a) and b) Photographs of part of top surface of Model D at end of strike-slip and second phase of deformation, respectively. Pre-existing R-shears become more pronounced with slightly normal and also left-lateral strike-slip components. Other R-shears pull apart and form tension gashes. Fault scarps dipping toward light appear bright; fault scarps dipping away from light appear dark.

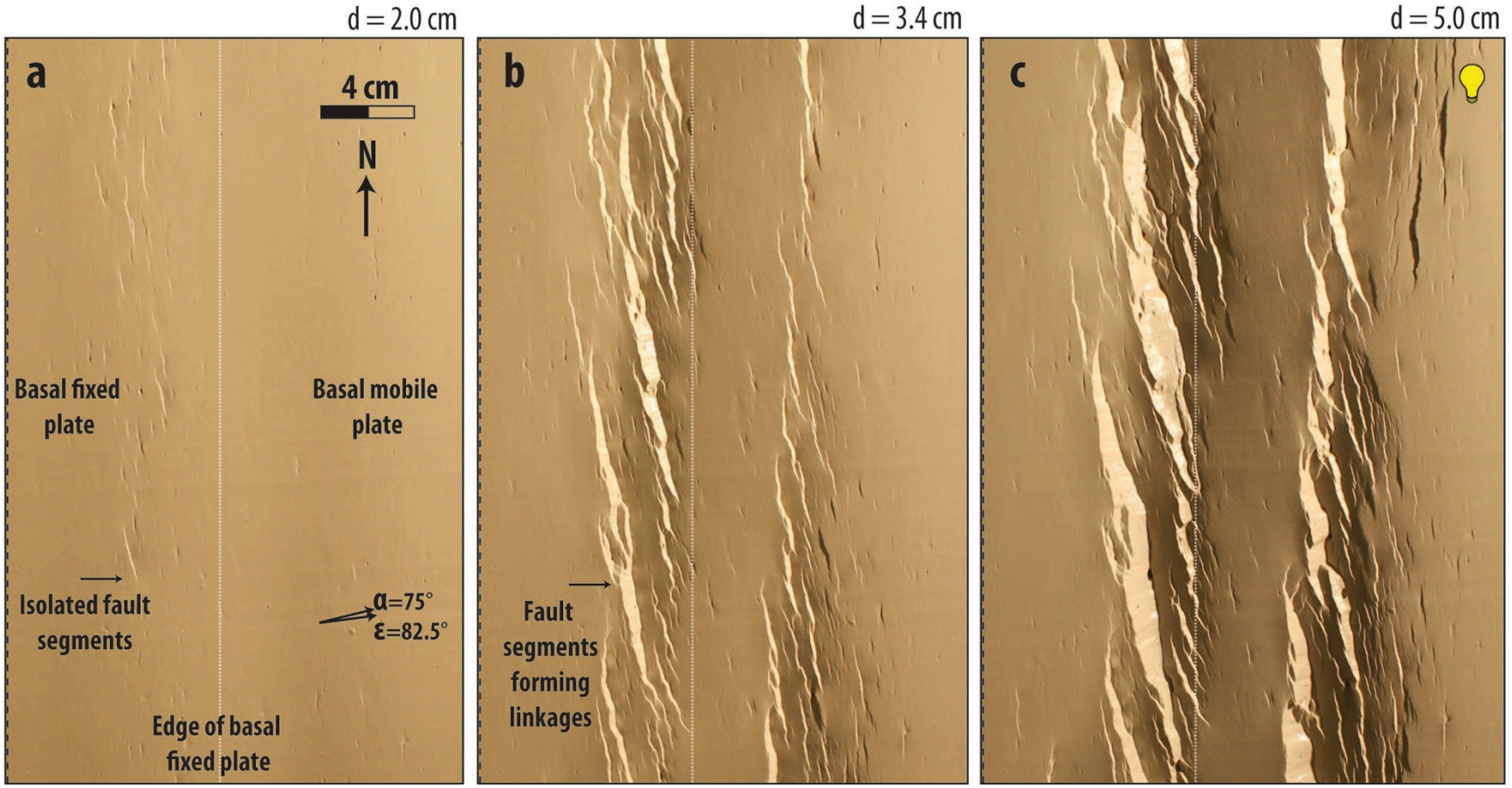

Figure 33. Evolution of faults during single phase of oblique extension in Model D1. a), b), and c) Map-view photographs of top surface at 2.0 cm, 3.4 cm, and 5.0 cm of displacement, respectively. Their strike is 160° to 180° relative to the long axis of deformation. Fault scarps dipping toward light appear bright; fault scarps dipping away from light appear dark. Sides of photographs are above outer edges of silicone polymer.

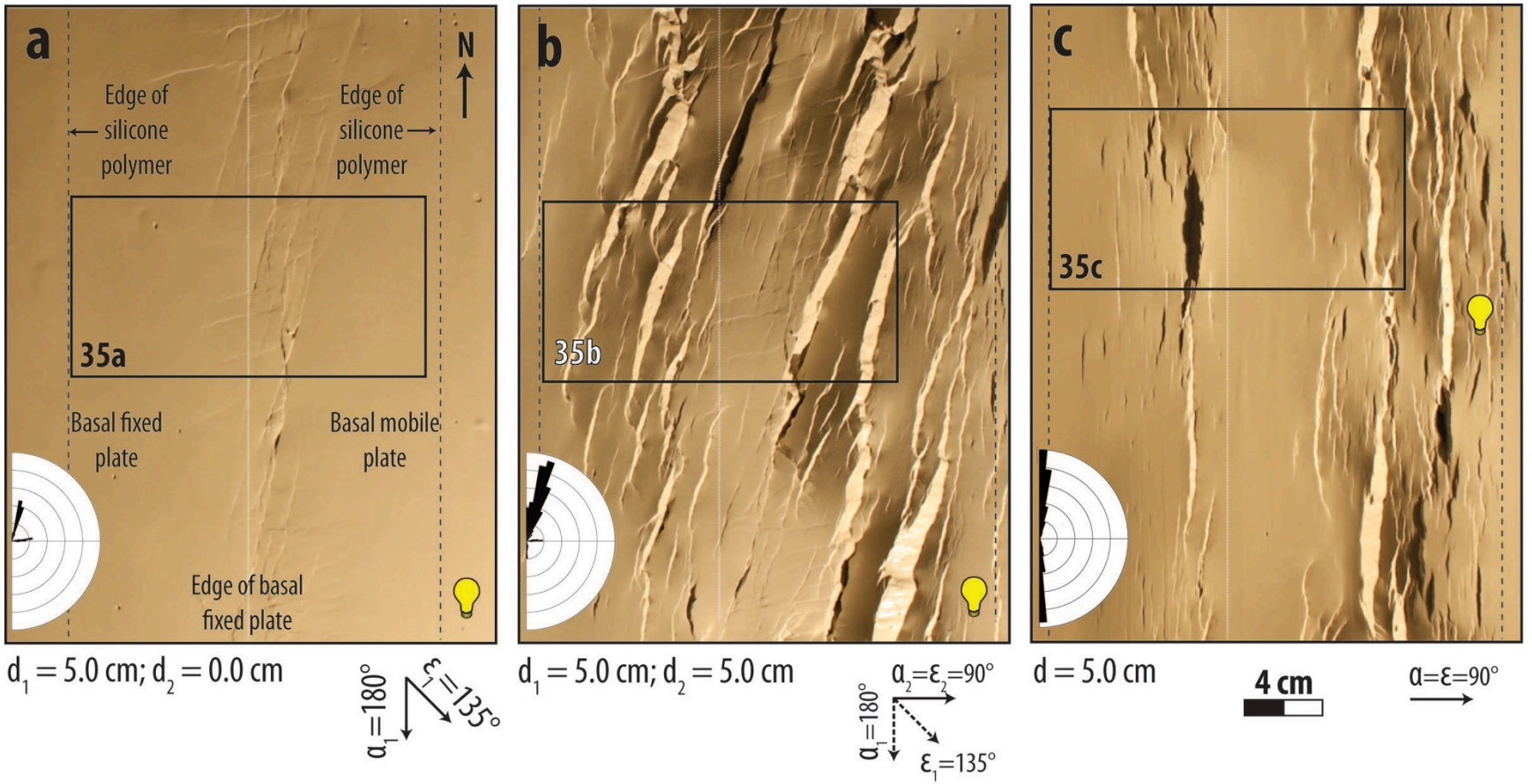

Figure 34. Map-view photographs of top surface of clay layer of Model E and Model E1. a) Model E at end of strike-slip phase of deformation. b) Model E at end of second phase of deformation. c) Model E1 at end of single phase of oblique extension. Fault scarps dipping toward light appear bright; fault scarps dipping away from light appear dark. Rose diagram shows trends of fault segments; bin size for rose diagram is 5°; outside circle of rose diagram is 120 cm. Rectangles show areas enlarged in Fig. 35.

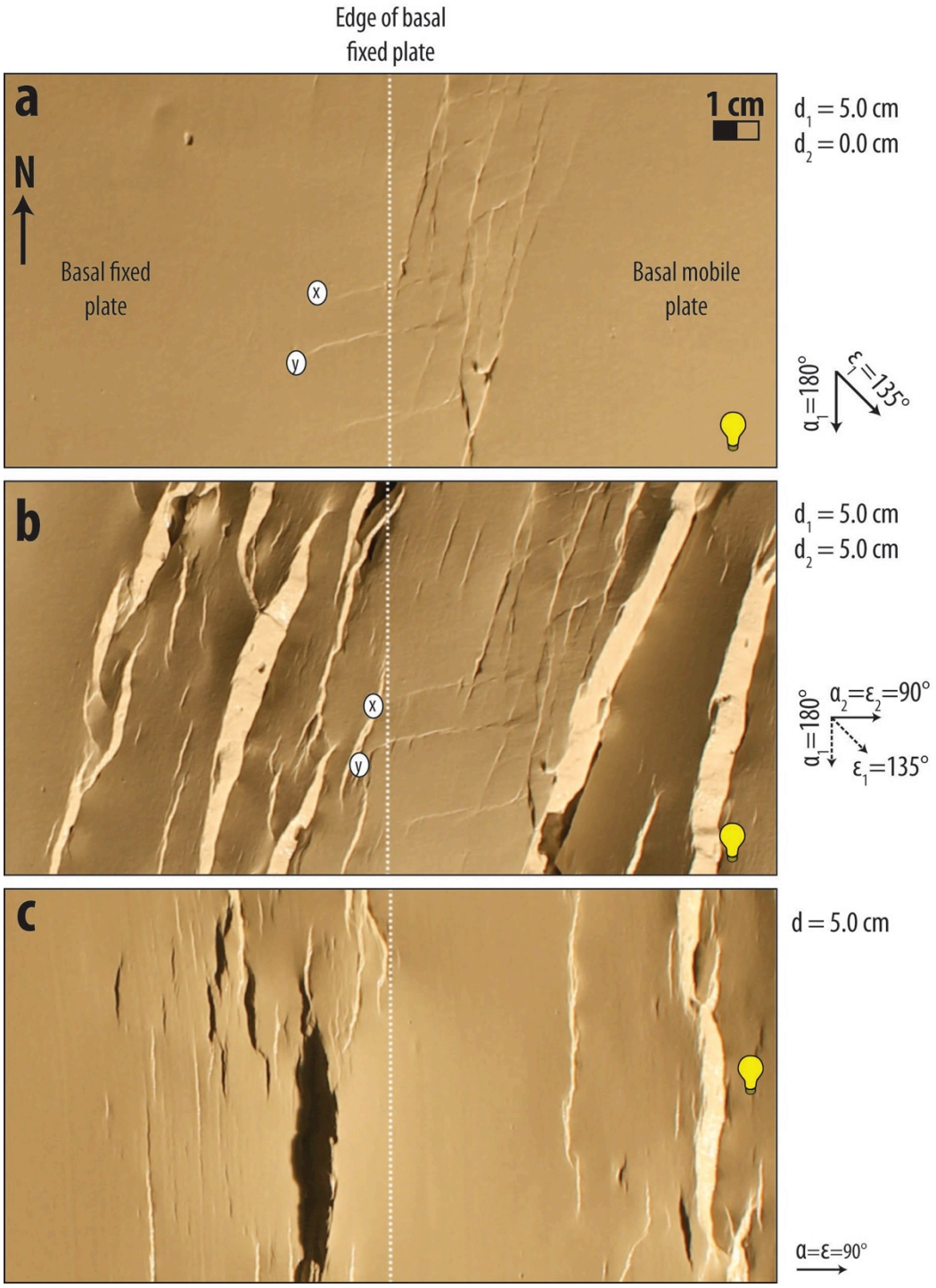

Figure 35. Close-up photographs of parts of Models E and E1 (for location, see Figure 34). a) Riedel shears present at the end of strike-slip phase of deformation in Model E. b) Fault pattern at end of Model E. Only a few new faults develop where pre-existing faults are well developed. Strike of most new faults resembles that of the pre-existing R-shears. Faults x and y in part a are Faults x and y in part b. c) Fault pattern at end of single phase of orthogonal extension in Model E1. Faults strike subperpendicular to maximum extension direction. Fault scarps dipping toward light appear bright; fault scarps dipping away from light appear dark.

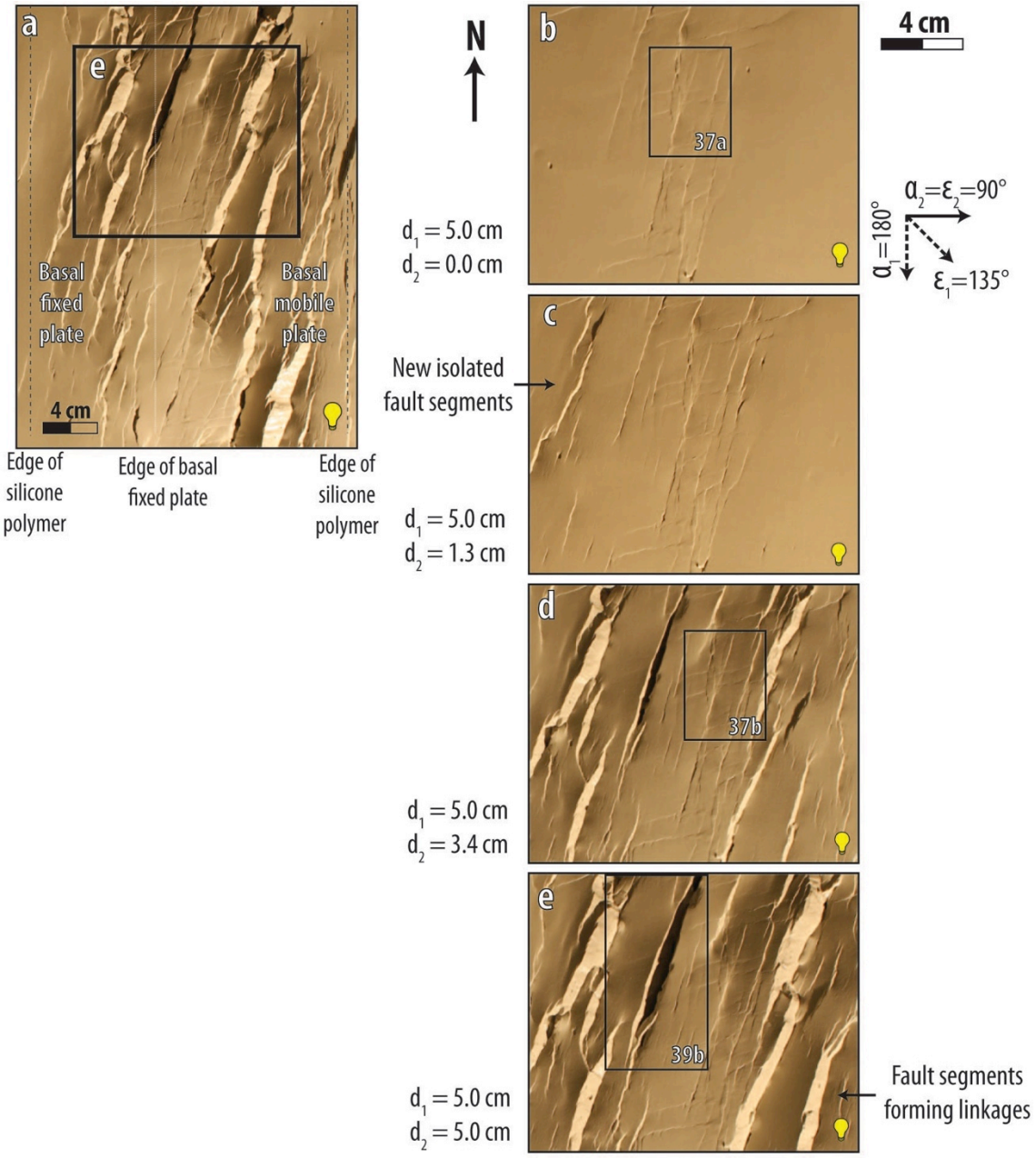

Figure 36. Evolution of faults during second phase of deformation in Model E. a) Photograph of top surface at 5.0 cm of displacement. Rectangle shows are enlarged in part e. b) to e) Photographs of part of top surface at 0.0 cm, 2.3 cm, 3.4 cm, and 5.0 cm of displacement, respectively. New faults are generally parallel to R-shears. They initially form as isolated segments and link together. Fault scarps dipping toward light appear bright; fault scarps dipping away from light appear dark. Rectangles show areas enlarged in Figs. 37 and 39.

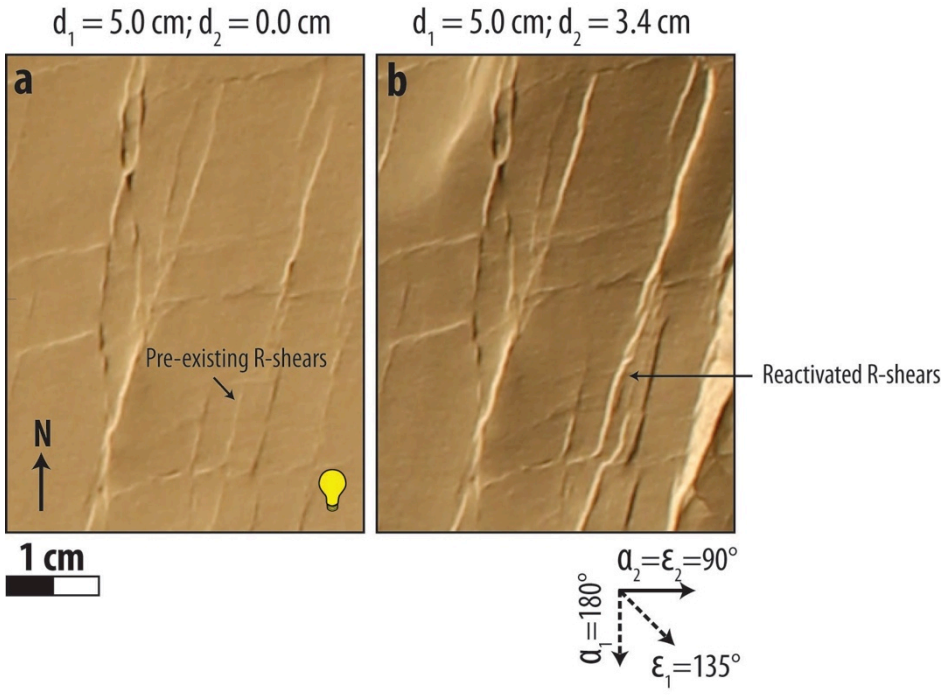

Figure 37. Example of fault interaction and reactivation of pre-existing R-shears in Model E (for location, see Figure 36). a) and b) Photographs of part of top surface at 0 cm and 3.4 cm of displacement, respectively. During second phase of deformation, pre-existing R-shears become more pronounced with slightly greater dip-slip component during the second phase of deformation. Fault scarps dipping toward light appear bright; fault scarps dipping away from light appear dark.

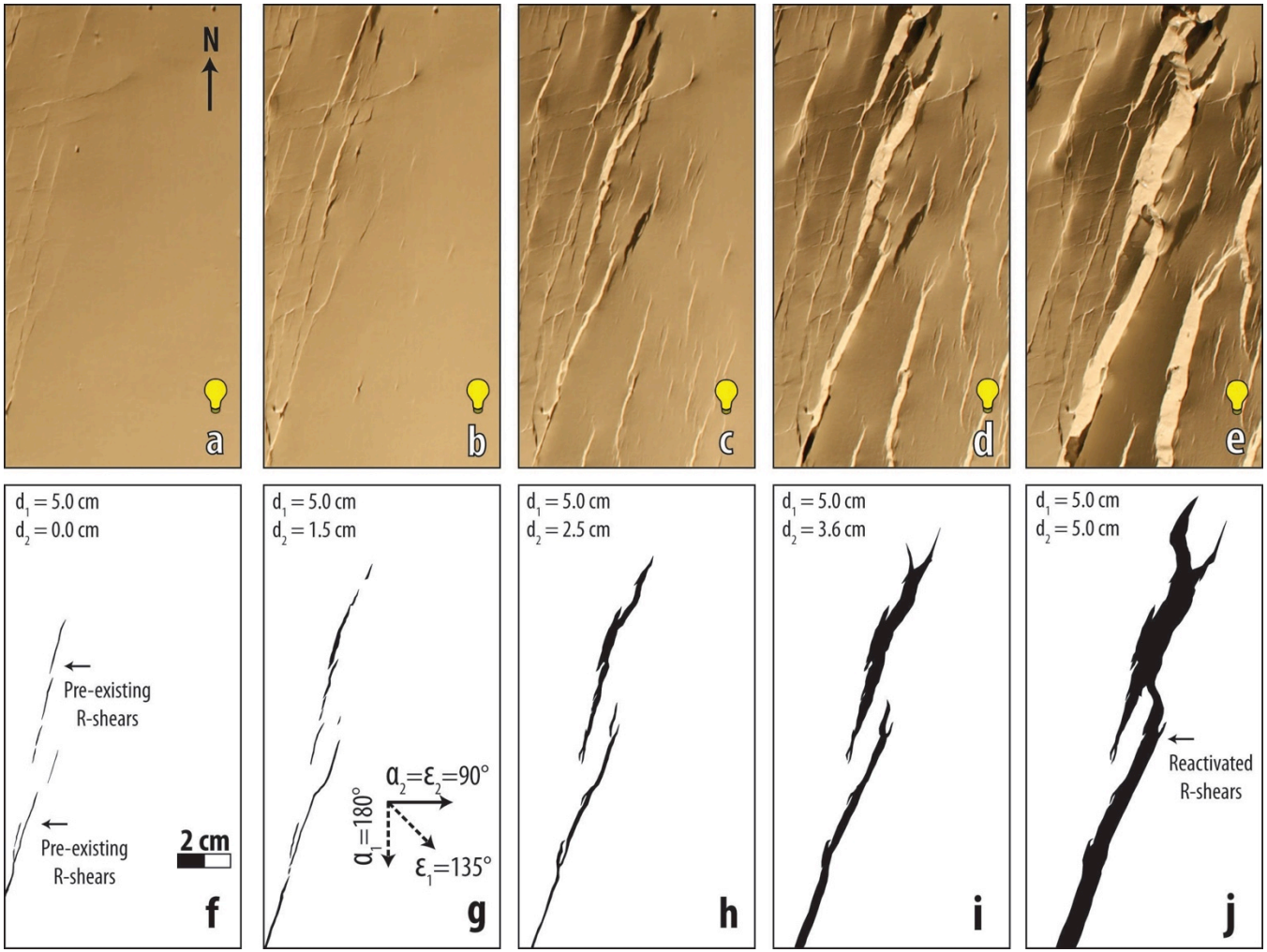

Figure 38. Reactivation of pre-existing R-shears during second phase of deformation in Model E. The faults in this figure are located in the same area as Figure 36a. a) to e) Photographs of part of top surface at 0 cm, 2.9 cm, and 3.8 cm of displacement, respectively. Fault scarps dipping toward light appear bright; fault scarps dipping away from light appear dark. f) to j) Line drawings of select faults showing reactivation of pre-existing R-shears. During second phase of deformation, they become more pronounced with a significantly greater dip-slip component of displacement.

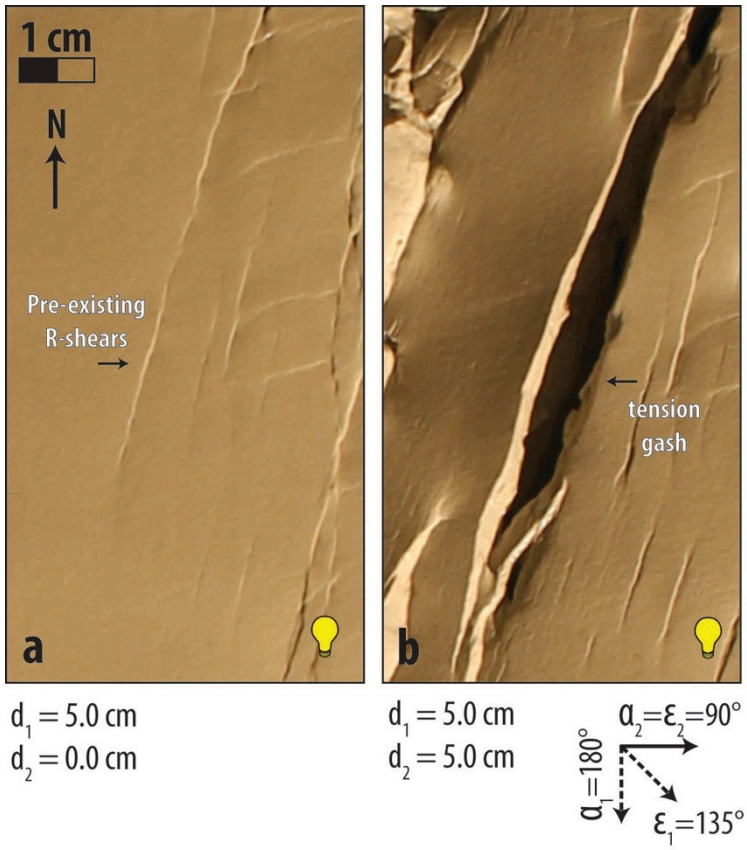

Figure 39. Formation of tension gashes during second phase of deformation in Model E (for location, see Figure 36d). a) and b) Photographs of part of top surface at 0 cm and 5 cm of displacement, respectively. Pre-existing R-shears pull apart and form tension gash. Fault scarps dipping toward light appear bright; fault scarps dipping away from light appear dark.

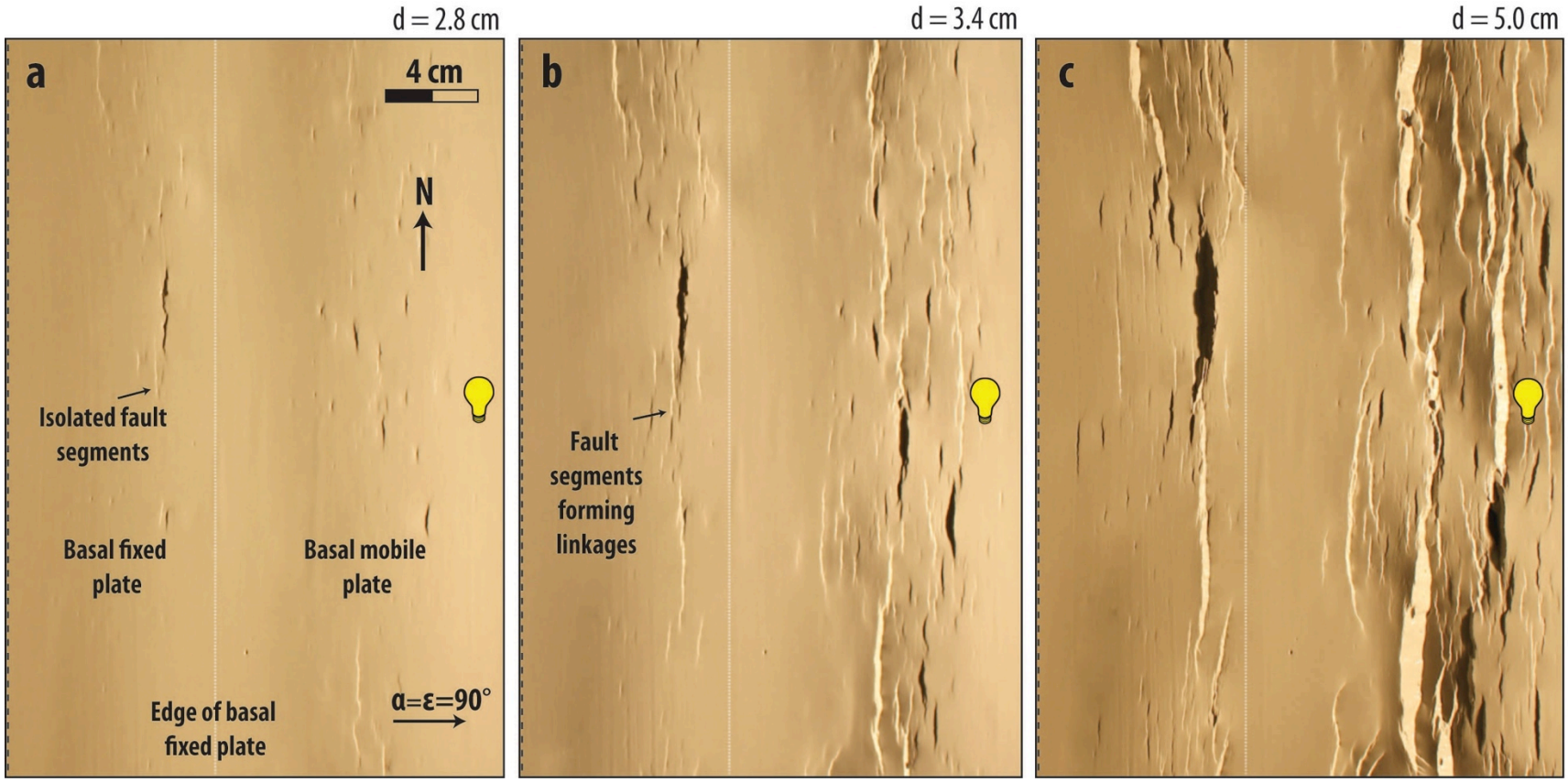

Figure 40. Evolution of faults during single phase of oblique extension in Model E1. a), b), and c) Map-view photographs of top surface of Model E1 at 2.8 cm, 3.4 cm, and 5 cm of displacement, respectively. Fault scarps dipping toward light appear bright; fault scarps dipping away from light appear dark. Their strike is 165° to 195° relative to the long axis of deformation. Sides of photographs are above outer edges of silicone polymer.

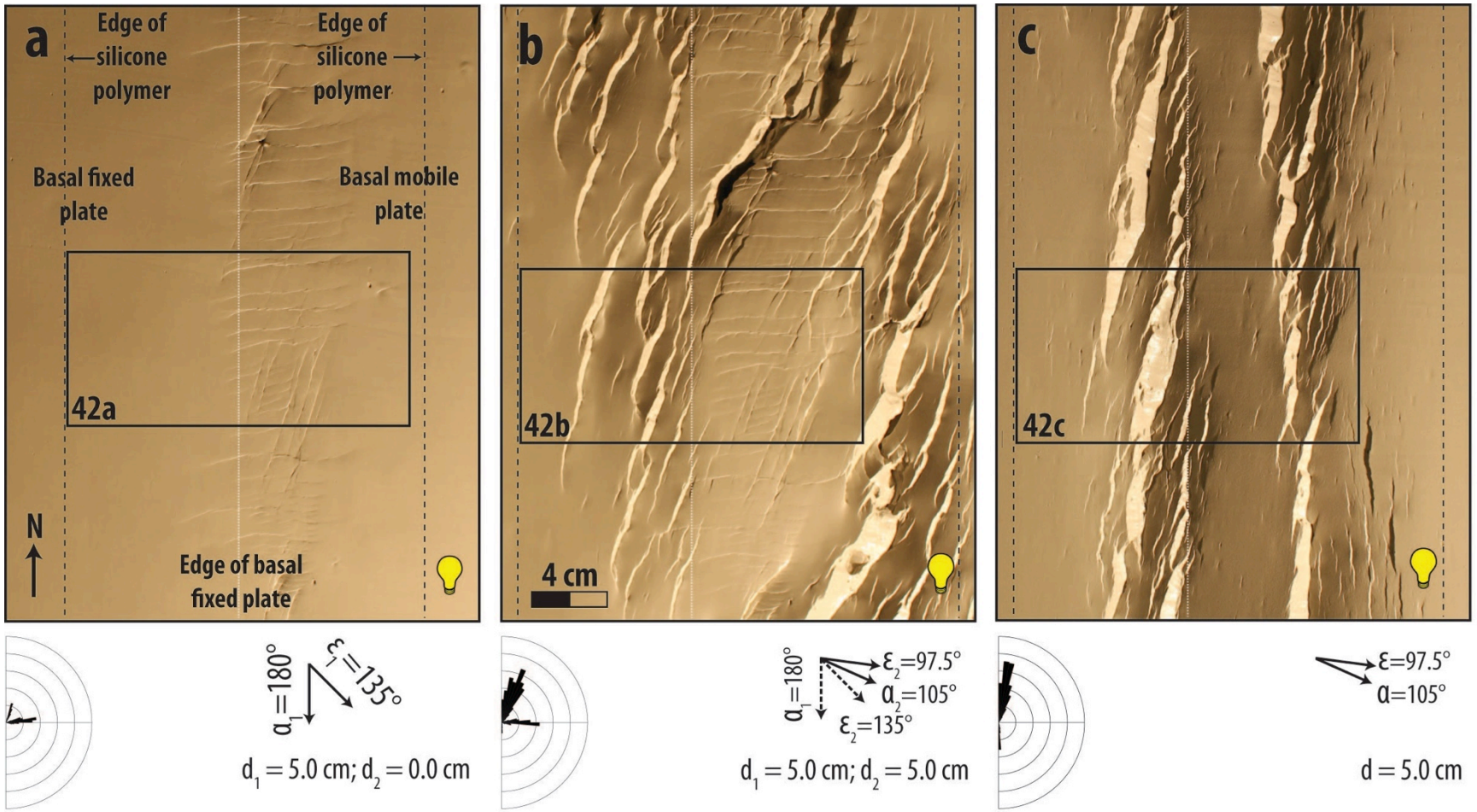

Figure 41. Map-view photographs of top surface of clay layer of Model F and Model F1. a) Model F at end of strike-slip phase of deformation. b) Model F at end of second phase of deformation. c) Model F1 at end of single phase of oblique extension. Fault scarps dipping toward light appear bright; fault scarps dipping away from light appear dark. Rose diagram shows trends of fault segments; bin size for rose diagram is 5°; outside circle of rose diagram is 120 cm. Rectangles show areas enlarged in Fig. 42.

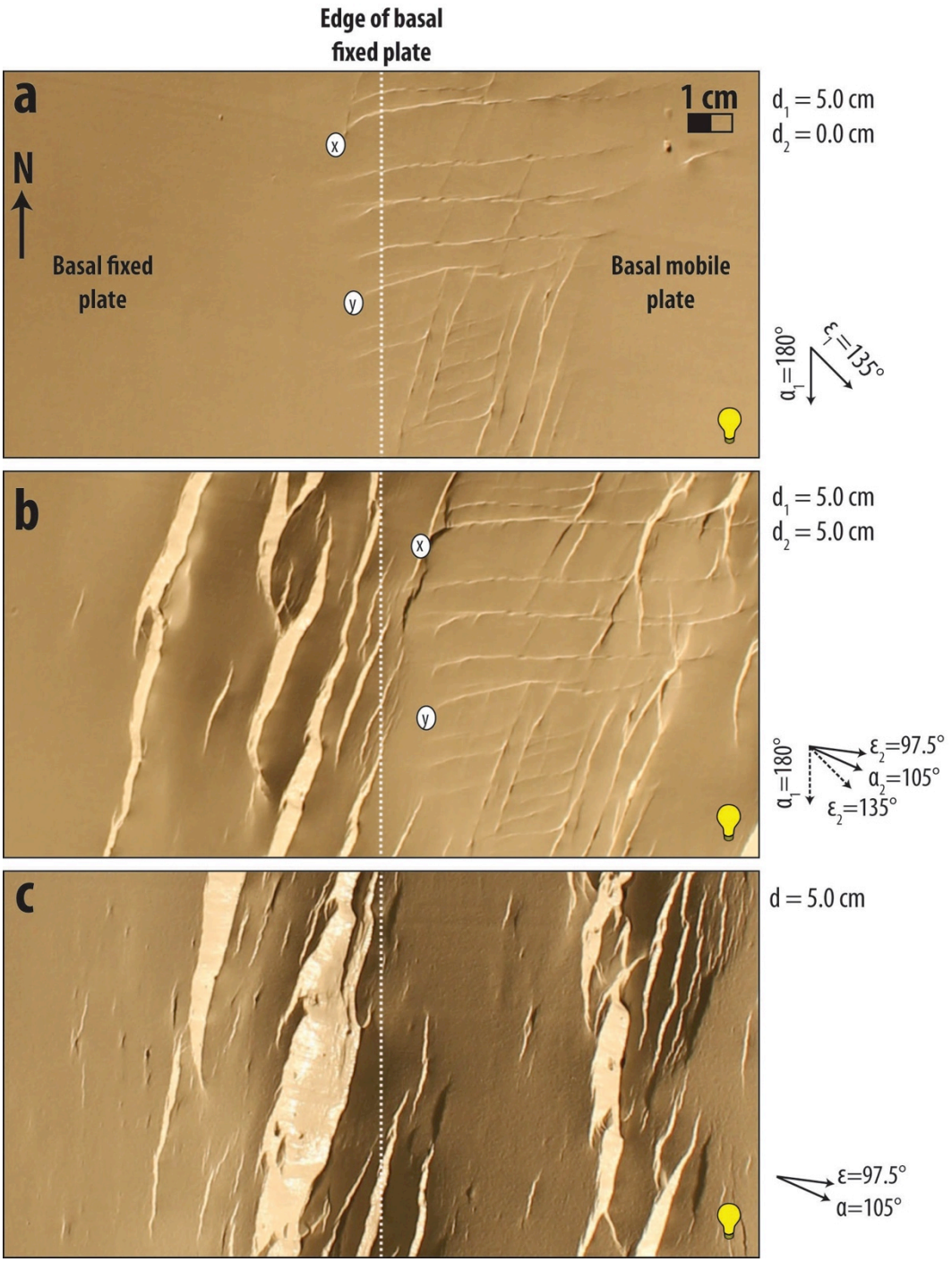

Figure 42. Close-up photographs of parts of Models F and F1 (for location, see Figure 41). a) Riedel shears present at the end of strike-slip phase of deformation in Model F. b) Fault pattern at end of Model F. Strike of new faults resembles those of pre-existing R-shears and is similar to new faults in Model F1. Faults x and y in part a are Faults x and y in part b. c) Fault pattern at end of deformation in F1. These faults strike subperpendicular to maximum extension direction. Fault scarps dipping toward light appear bright; fault scarps dipping away from light appear dark.

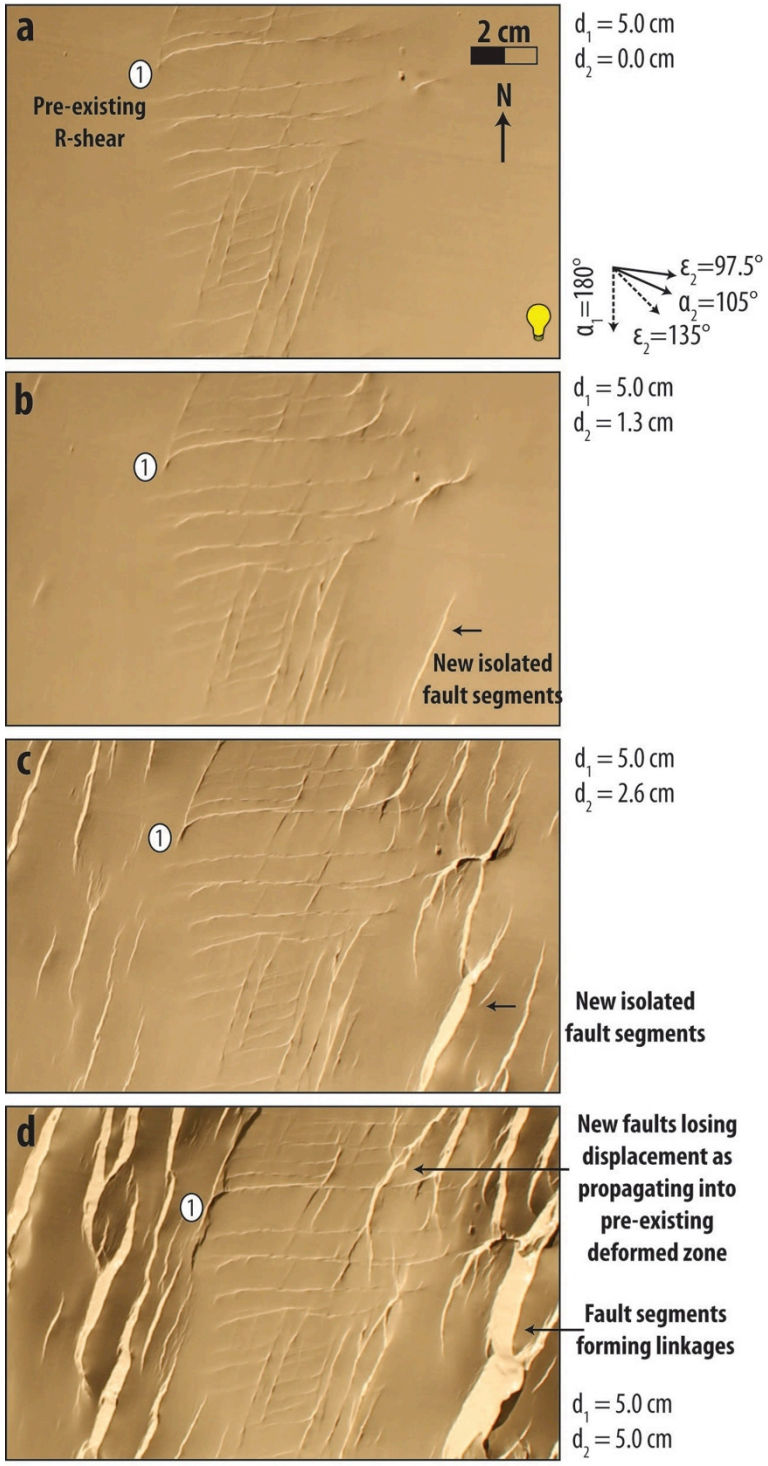

Figure 43. Evolution of faults during second phase of deformation in Model F. a), b), c), and d) Photographs of part of top surface of Model F at 0 cm, 1.3 cm, 2.6 cm, and 5.0 cm of displacement, respectively. Horsetail splays form on pre-existing R'-shear (Fault 1), indicating reactivation of this fault (left-lateral strike-slip). New faults initially form as isolated segments before linking together. They lose displacement as they encounter pre-existing faults. Fault scarps dipping toward light appear bright; fault scarps dipping away from light appear dark.

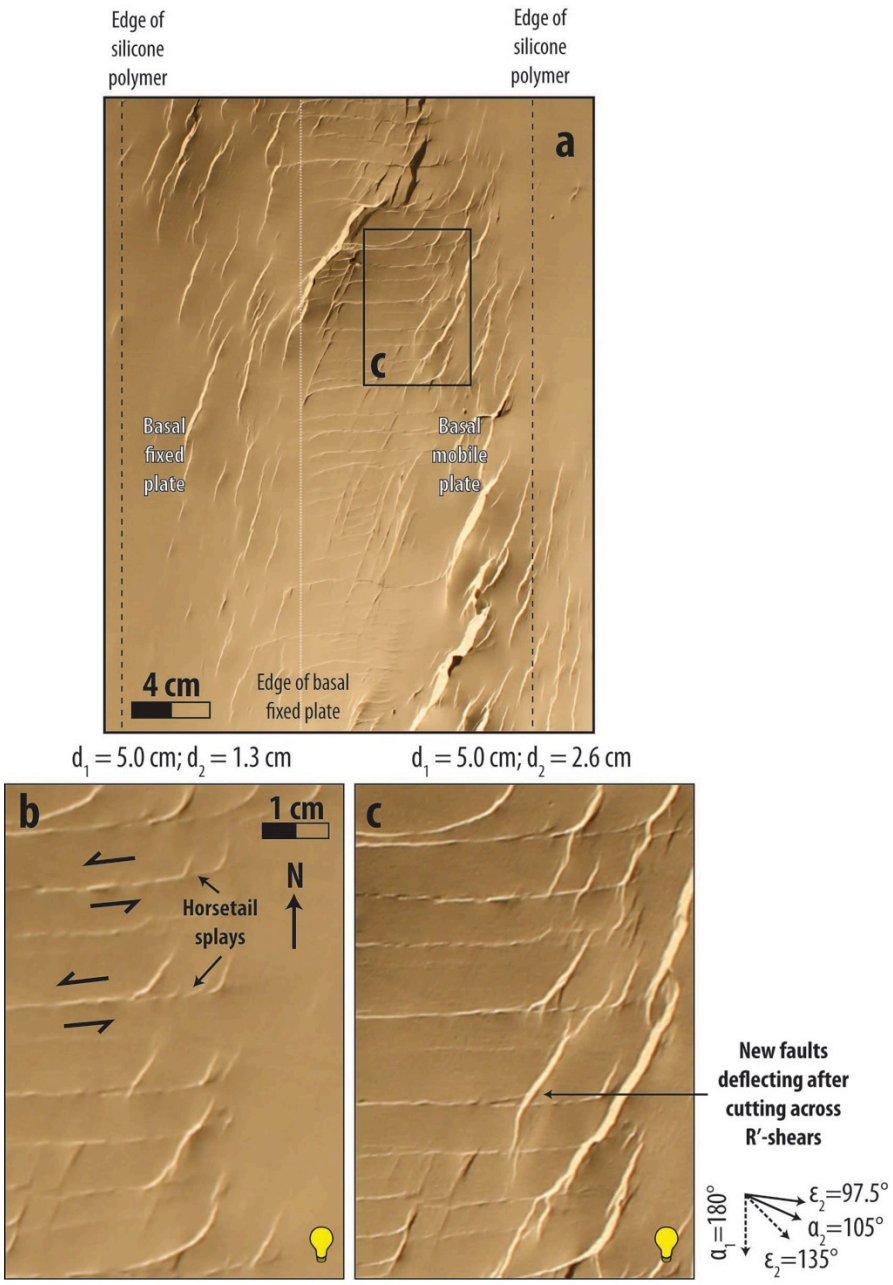

Figure 44. Example of fault interactions during second phase of deformation in Model F. a) Photograph of top surface at 2.6 cm of displacement. Rectangle shows are enlarged in part c. b) and c) Photographs of part of top surface at 1.3 cm and 2.6 cm of displacement, respectively, showing horsetail splays that indicate that pre-existing R'-shears reactivate with left-lateral strike-slip. Deflection of new faults suggests that pre-existing faults become barriers to new fault propagation. Fault scarps dipping toward light appear bright; fault scarps dipping away from light appear dark.

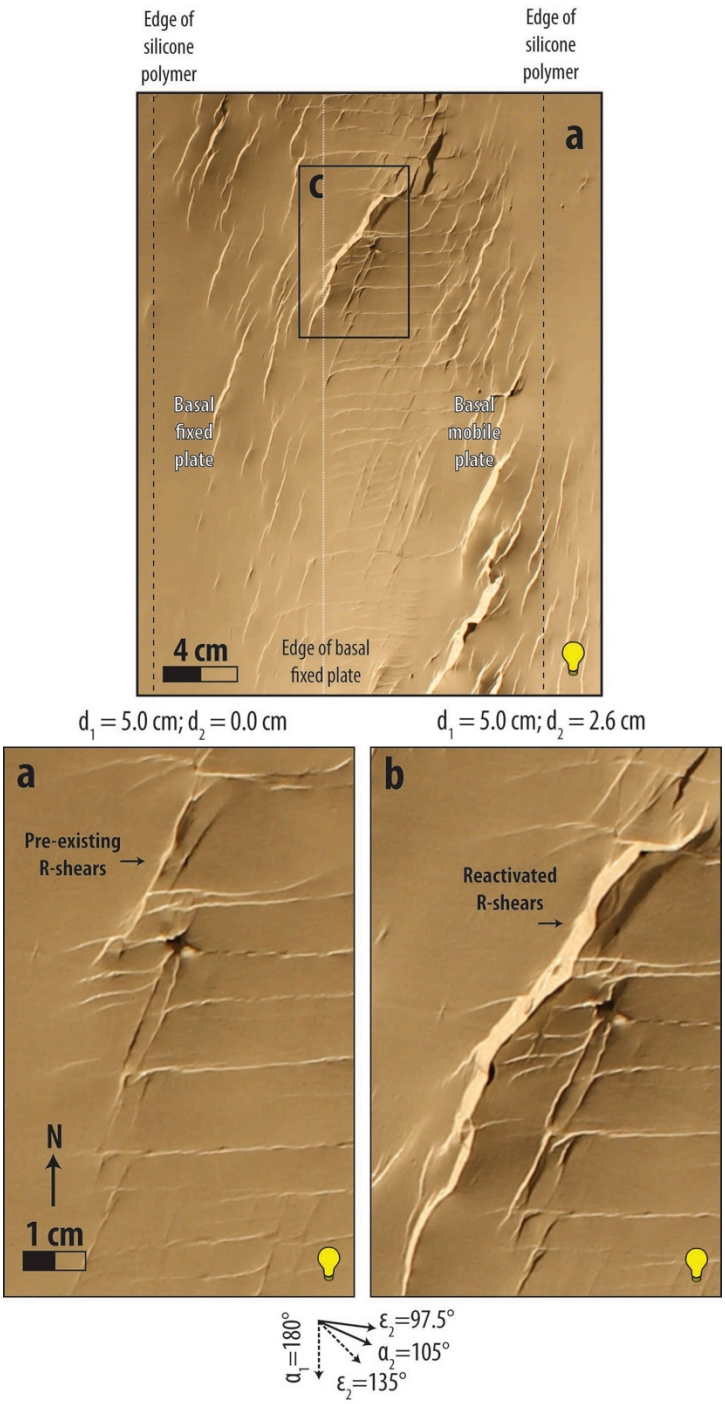

Figure 45. Reactivation of pre-existing R-shears during second phase of deformation in Model F. a) Photograph of top surface at 2.6 cm of displacement. Rectangle shows are enlarged in part c. b) and c) Photographs of part of top surface of Model F at 0.0 cm and 2.6 cm of displacement, respectively. Fault scarps dipping toward light appear bright; fault scarps dipping away from light appear dark. During second phase of deformation, pre-existing R-shears become more pronounced with greater dip-slip component.

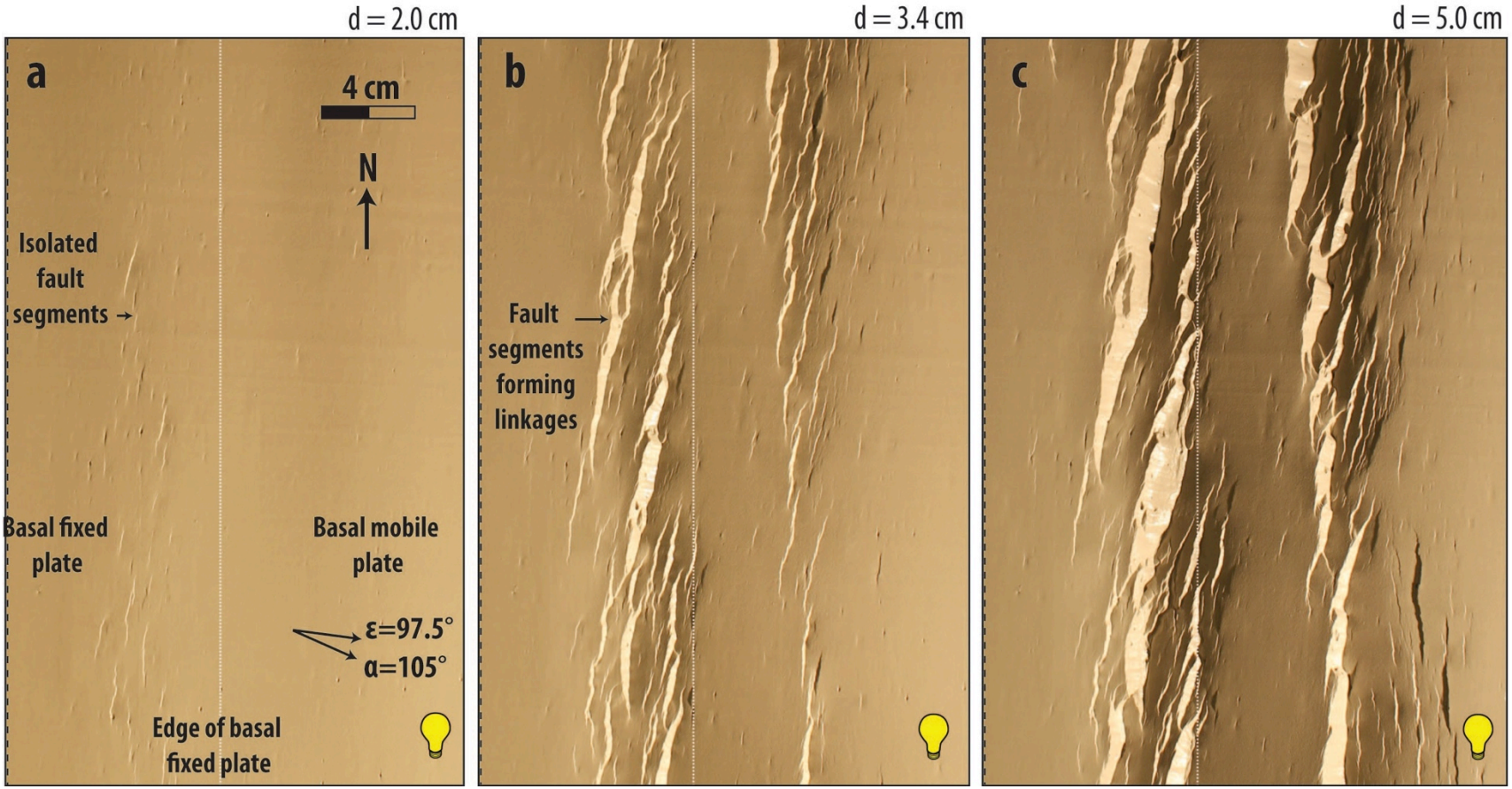

Figure 46. Evolution of faults during single phase of oblique extension in Model F1. a), b), and c) Map-view photographs of top surface at 2.0 cm, 3.4 cm, and 5 cm of displacement, respectively. Fault scarps dipping toward light appear bright; fault scarps dipping away from light appear dark. Their strike is 175° to 205° relative to the long axis of deformation. Sides of photographs are above outer edges of silicone polymer.

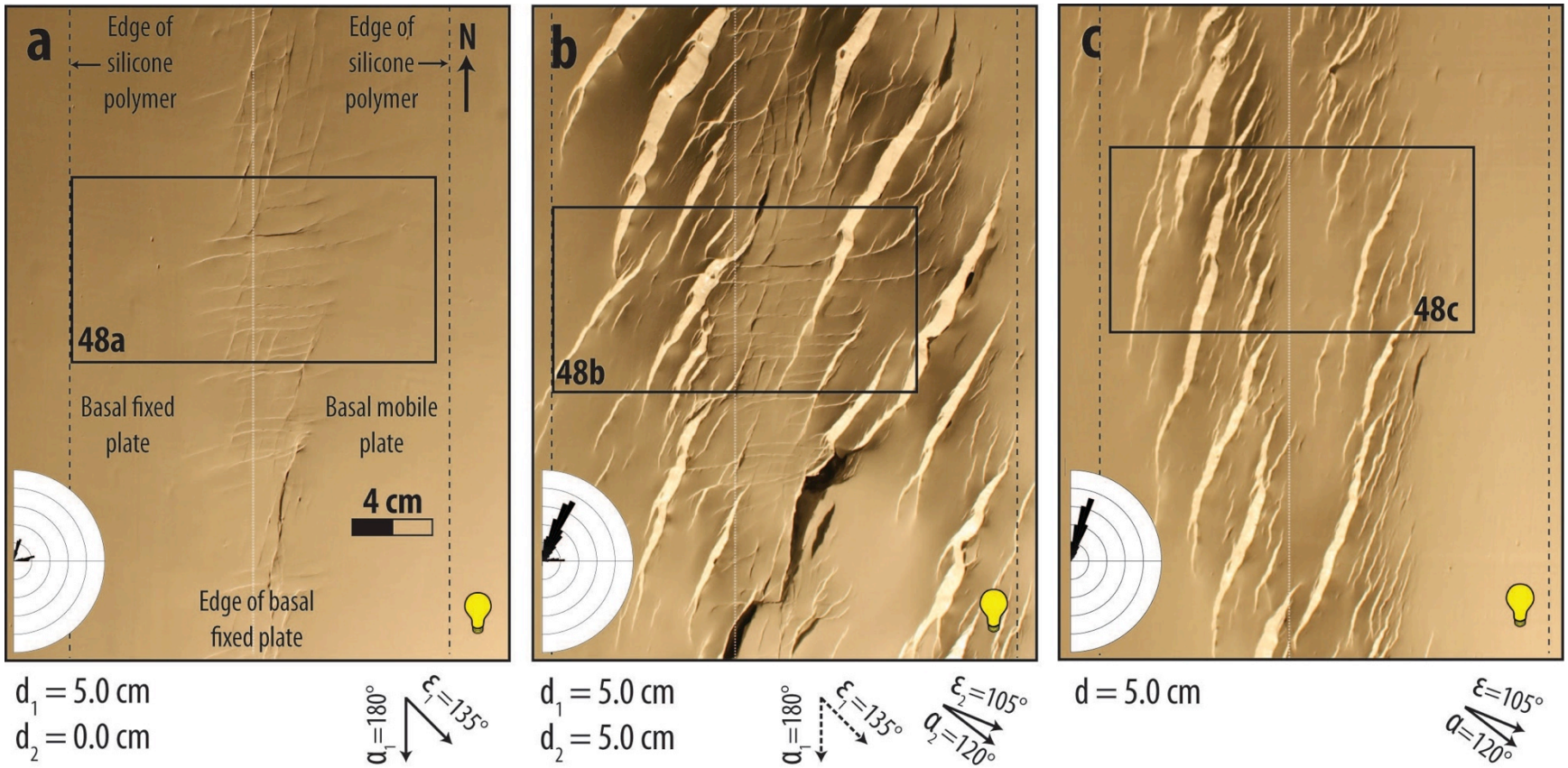

Figure 47. Map-view photographs of top surface of clay layer of Model G and Model G1. a) Model G at end of strike-slip phase of deformation. b) Model G at end of second phase of deformation. c) Model G1 at end of single phase of oblique extension. Fault scarps dipping toward light appear bright; fault scarps dipping away from light appear dark. Rose diagram shows trends of fault segments; bin size for rose diagram is 5°; outside circle of rose diagram is 120 cm. Rectangles show areas enlarged in Fig. 48.

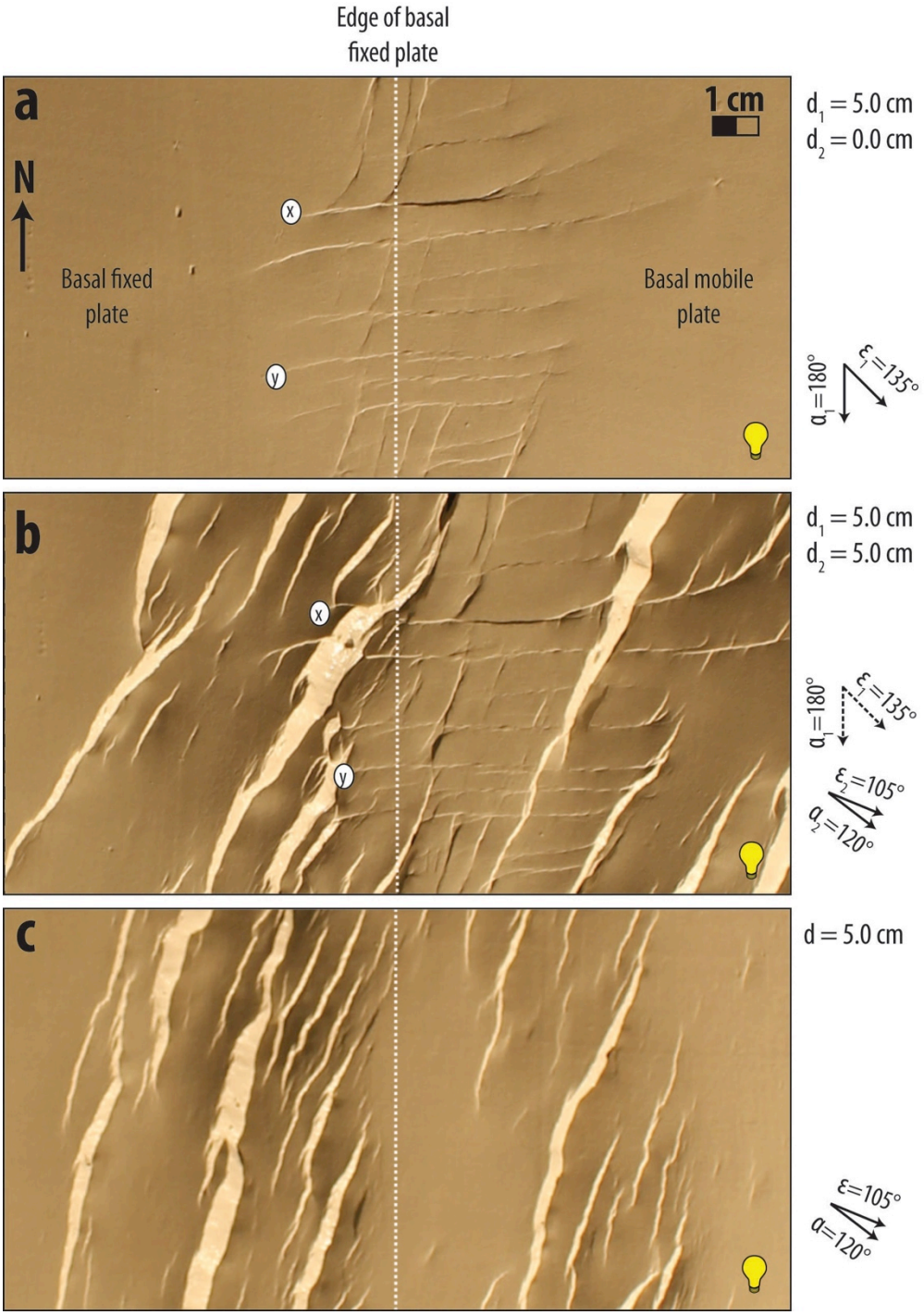

Figure 48. Close-up photographs of parts of Models G and G1 (for location, see Figure 47). a) Riedel shears present at the end of strike-slip phase of deformation in Model G. b) Fault pattern at end of Model G. Strike of new faults resembles those of pre-existing R-shears. New faults are deflected after cutting across pre-existing R'-shears. Faults x and y in part a are Faults x and y in part b. c) Fault pattern at end of deformation in G1. This model has fewer faults than Model G. Faults have more displacement than those in Model G. They strike subperpendicular to maximum extension direction. Fault scarps dipping toward light appear bright; fault scarps dipping away from light appear dark.

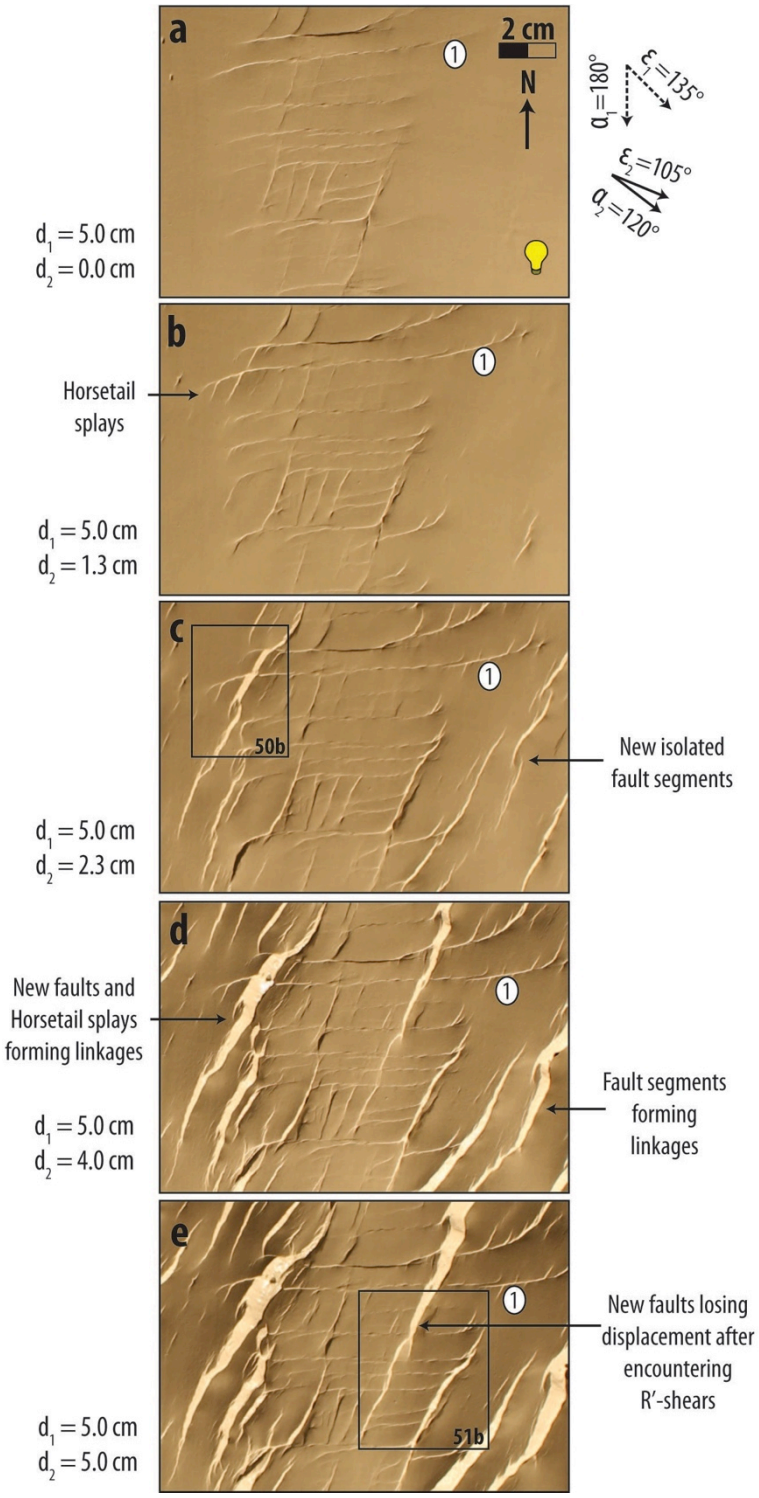

Figure 49. Evolution of new faults formed during second phase of deformation in Model G. a), b), c), d), and e) Photographs of part of top surface at 0.0 cm, 1.3 cm, 2.3 cm, 4.0 cm, and 5.0 cm of displacement, respectively. During second phase of deformation, pre-existing faults move southward and rotate clockwise relative to the long axis of deformation zone (e.g., Fault 1). Horsetail splays on pre-existing R'-shears (e.g., Fault 1) suggest that faults reactivate with left-lateral strike-slip. New faults later cut across R'-shears and die out. Fault scarps dipping toward light appear bright; fault scarps dipping away from light appear dark. Rectangles show areas enlarged in Figs. 50 and 51.

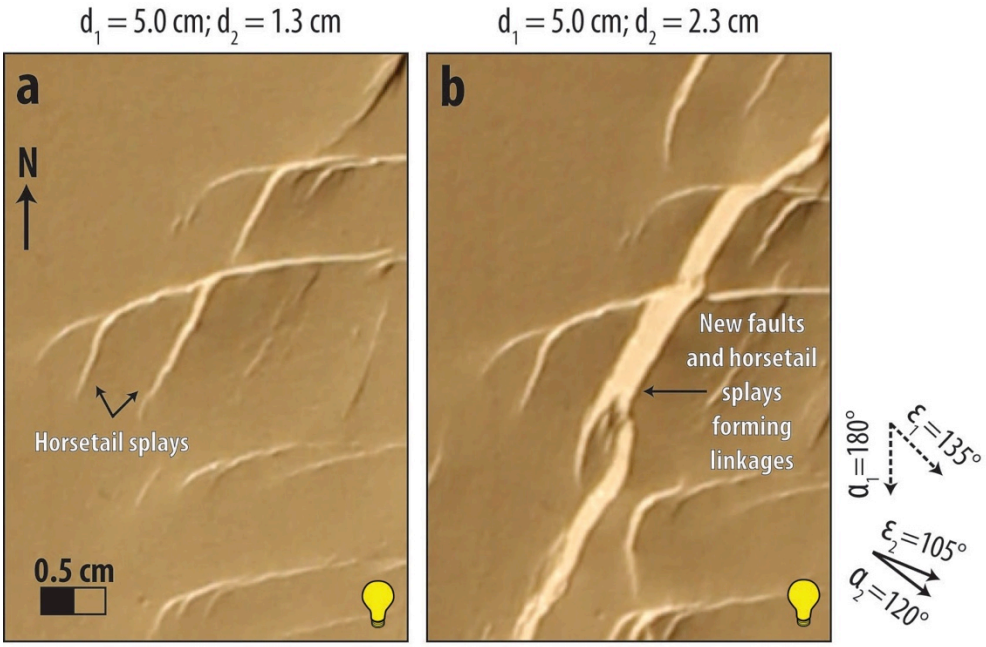

Figure 50. Example of fault reactivation during second phase of deformation in Model G (for location, see Figure 49). a) and b) Photographs of part of top surface of Model G at 1.3 cm and 2.3 cm of displacement, respectively, showing that horsetail splays form on pre-existing R'-shears, indicating reactivation with left-lateral strike-slip. The R'-shears with horsetail splays become inactive once new faults cut them. Fault scarps dipping toward light appear bright; fault scarps dipping away from light appear dark.

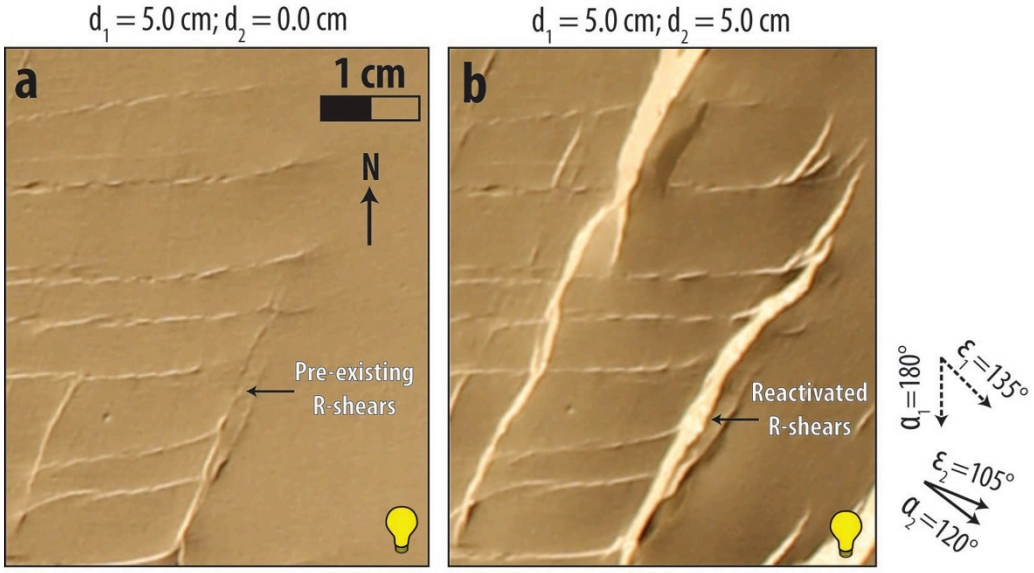

Figure 51. Reactivation of pre-existing R-shears during second phase of deformation in Model G (for location, see Figure 49). a) and b) Photographs of part of top surface at 0 cm and 5.0 cm of displacement, respectively. R-shears reactivate with greater dip-slip component of as experiment progresses. Fault scarps dipping toward light appear bright; fault scarps dipping away from light appear dark.

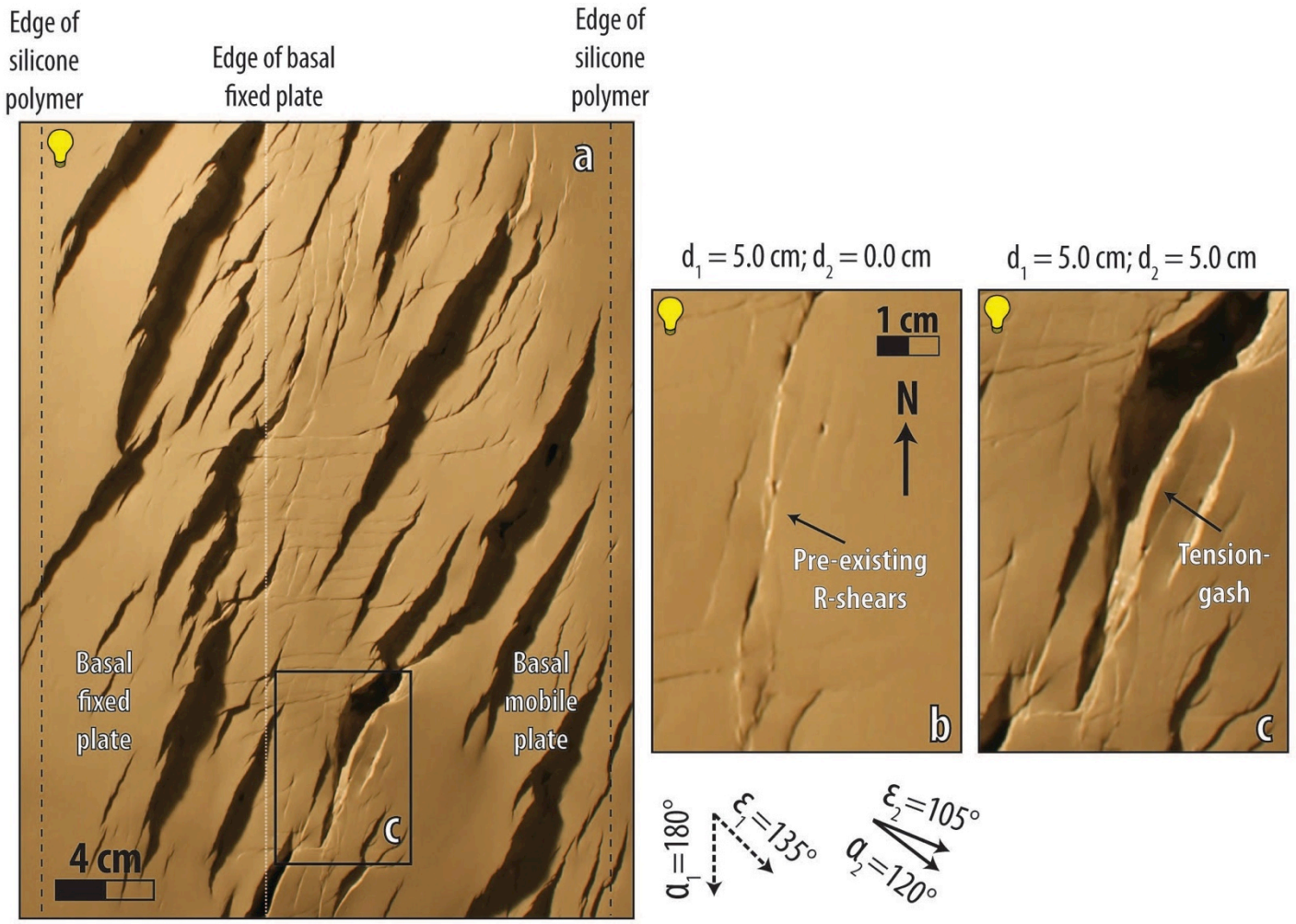

Figure 52. Formation of tension gashes during second phase of deformation in Model G. a) Photograph of part of top surface at 5 cm of displacement. Rectangle shows area enlarged in Figure c. b) and c) Photographs of part of top surface of Model G at 0 cm and 5.0 cm of displacement. R-shears pull apart and form tension gashes as experiment progresses. Fault scarps dipping toward light appear bright; fault scarps dipping away from light appear dark.

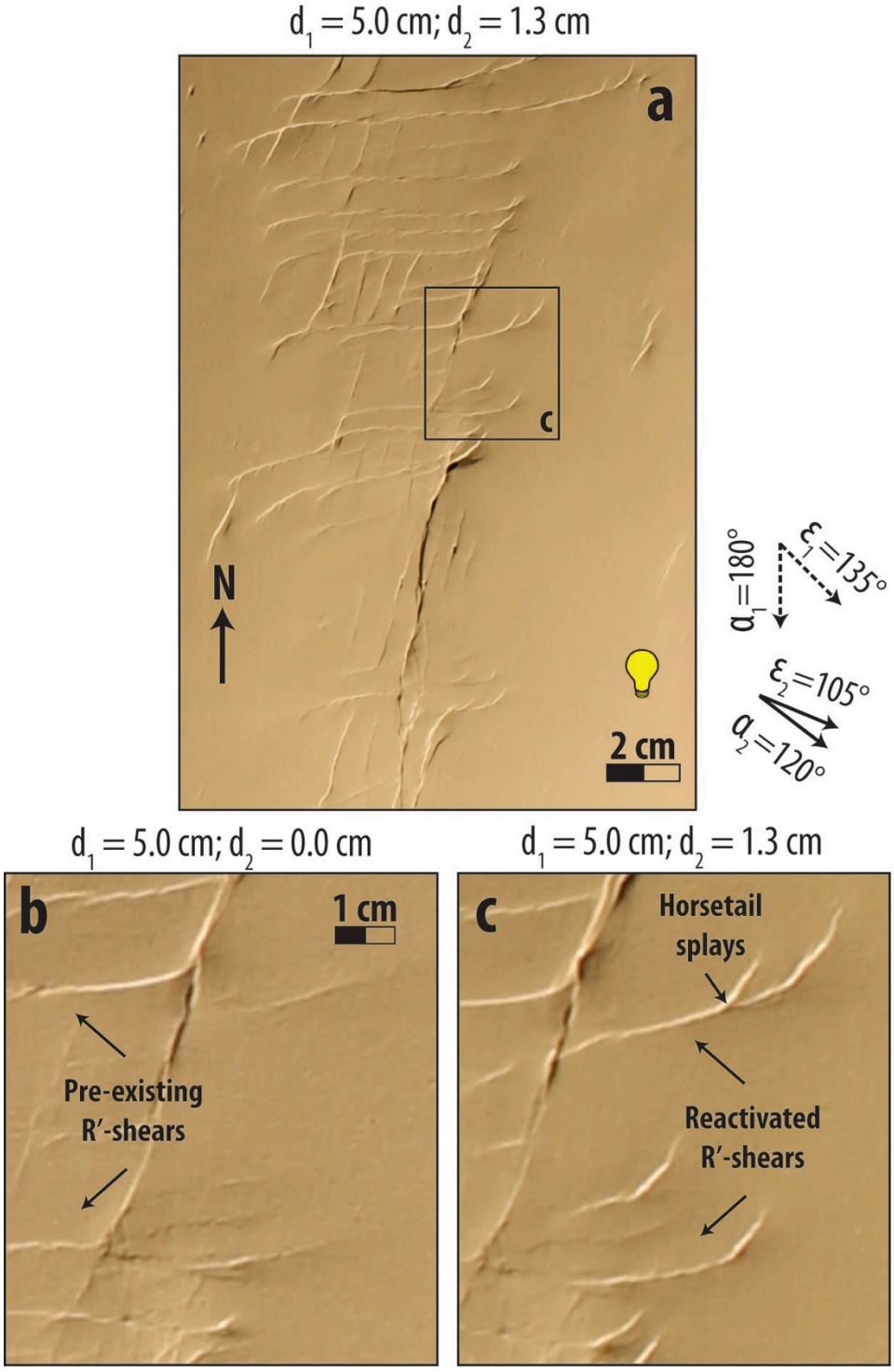

Figure 53. Reactivation of pre-existing R'-shears during second phase of deformation in Model G. a) Photograph of part of top surface at 1.3 cm of displacement. Rectangle shows area enlarged in Figure c. b) and c) Photographs of part of top surface at 0.0 cm and 1.3 cm of displacement, respectively. Length and dip-slip component of pre-existing R'-shears increase as experiment progresses. Horsetail splays on R'-shears suggest that they also reactivate with left-lateral strike-slip. Fault scarps dipping toward light appear bright; fault scarps dipping away from light appear dark.

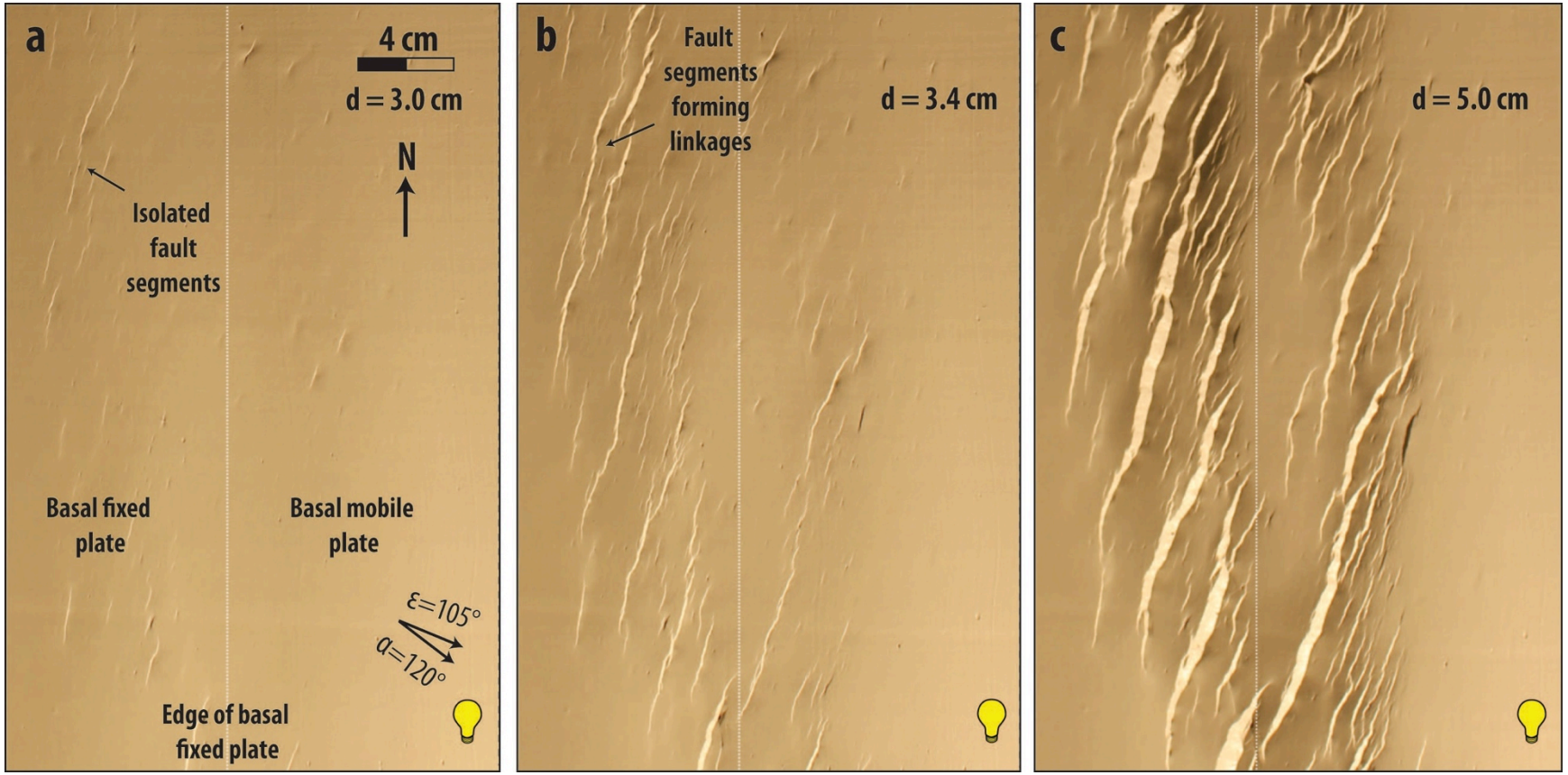

Figure 54. Evolution of faults during single phase of oblique extension in Model G1. a), b), and c) Map-view photographs of top surface at 3.0 cm, 3.4 cm, and 5 cm of displacement, respectively. Fault scarps dipping toward light appear bright; fault scarps dipping away from light appear dark. Their strike is 5° to 25° relative to the long axis of deformation. Sides of photographs are above outer edges of silicone polymer.

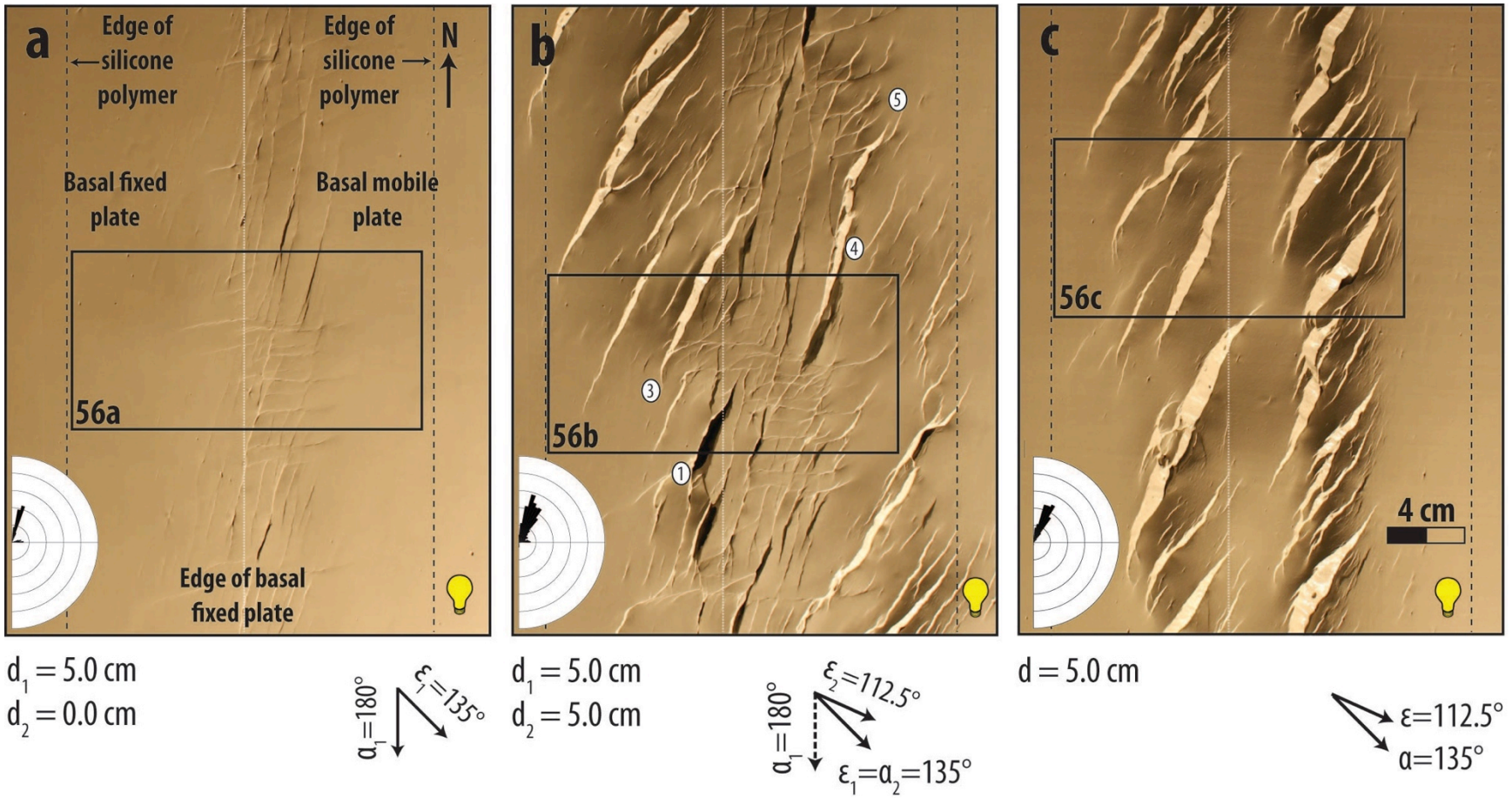

Figure 55. Map-view photographs of top surface of clay layer of Model H and Model H1. a) Model H at end of strike-slip phase of deformation. b) Model H at end of second phase of deformation. Faults 1, 3, 4, and 5 are referenced in subsequent figures. c) Model H1 at end of single phase of oblique extension. Fault scarps dipping toward light appear bright; fault scarps dipping away from light appear dark. Rose diagram shows trends of fault segments; bin size for rose diagram is 5°; outside circle of rose diagram is 120 cm. Rectangles show areas enlarged in Fig. 56.

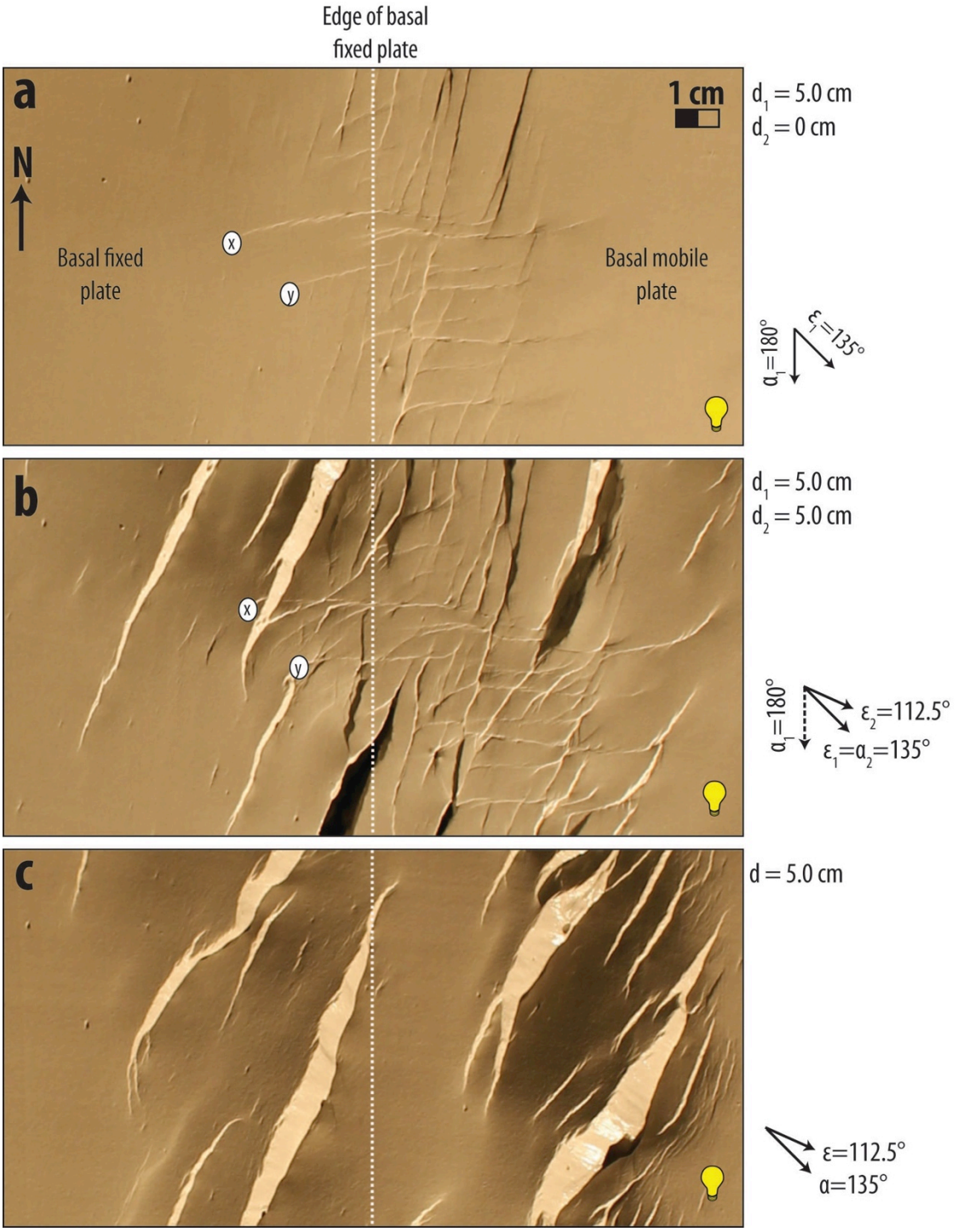

Figure 56. Close-up photographs of parts of Models H and H1 (for location, see Figure 55). a) Riedel shears present at the end of strike-slip phase of deformation in Model H. b) Fault pattern at end of second phase of deformation in Model H. New faults strike 160° to 190° clockwise relative to the long axis of deformation zone. They die out as they encounter zone where pre-existing R'-shears population is better developed. Faults x and y in part a are Faults x and y in part b. c) Fault pattern at end of deformation in H1. These faults strike subperpendicular to maximum extension direction. Fault scarps dipping toward light appear bright; fault scarps dipping away from light appear dark.

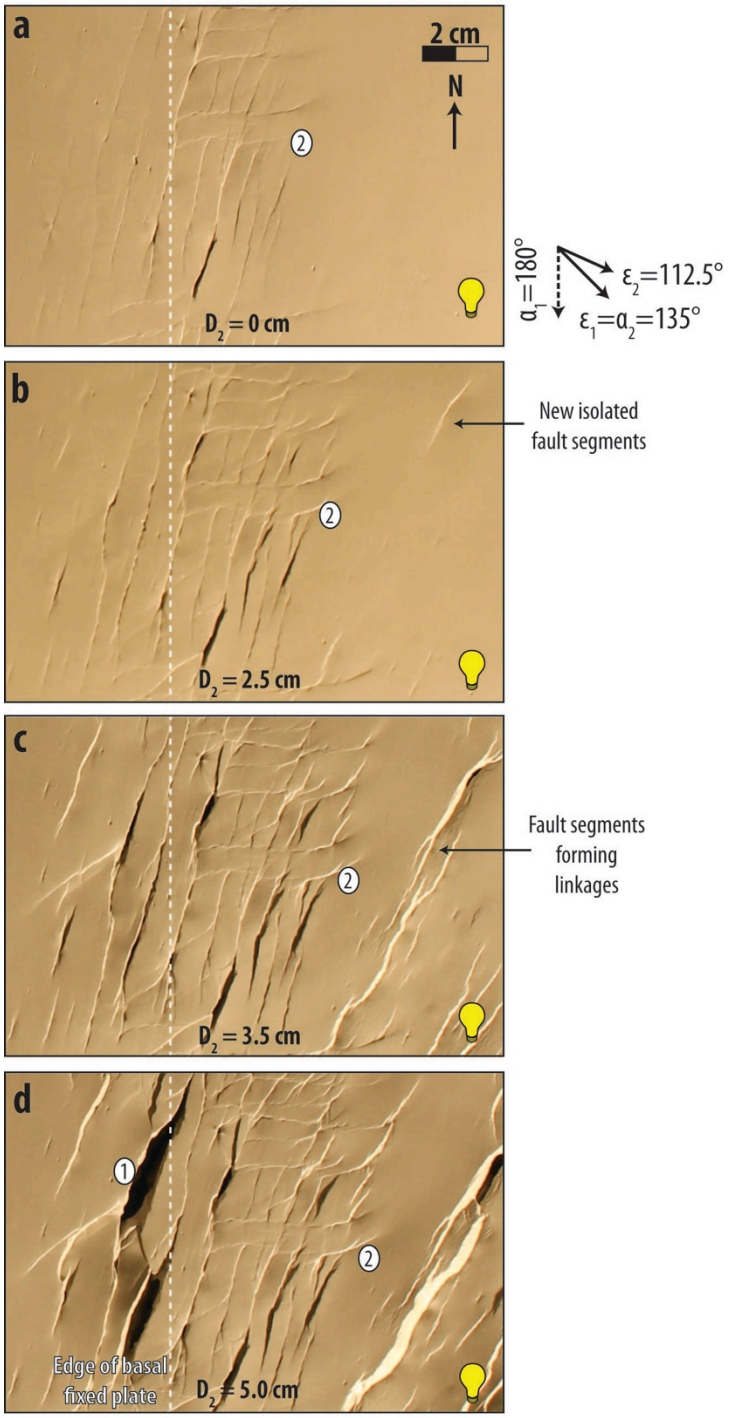

Figure 57. Evolution of faults during second phase of deformation in Model H (for location, see Fault 1 in Figure 55b). a) to d) Photographs of part of top surface of Model H at 0 cm, 2.5 cm, 3.5 cm, and 5.0 cm of displacement, respectively. During second phase of deformation, pre-existing faults move southward and rotate clockwise (e.g., Fault 2). Many R-shears pull apart and form tension gashes (Fault 1). Horsetail splays on R'-shears indicate reactivation (see details in Figure 58). Fault scarps dipping toward light appear bright; fault scarps dipping away from light appear dark.

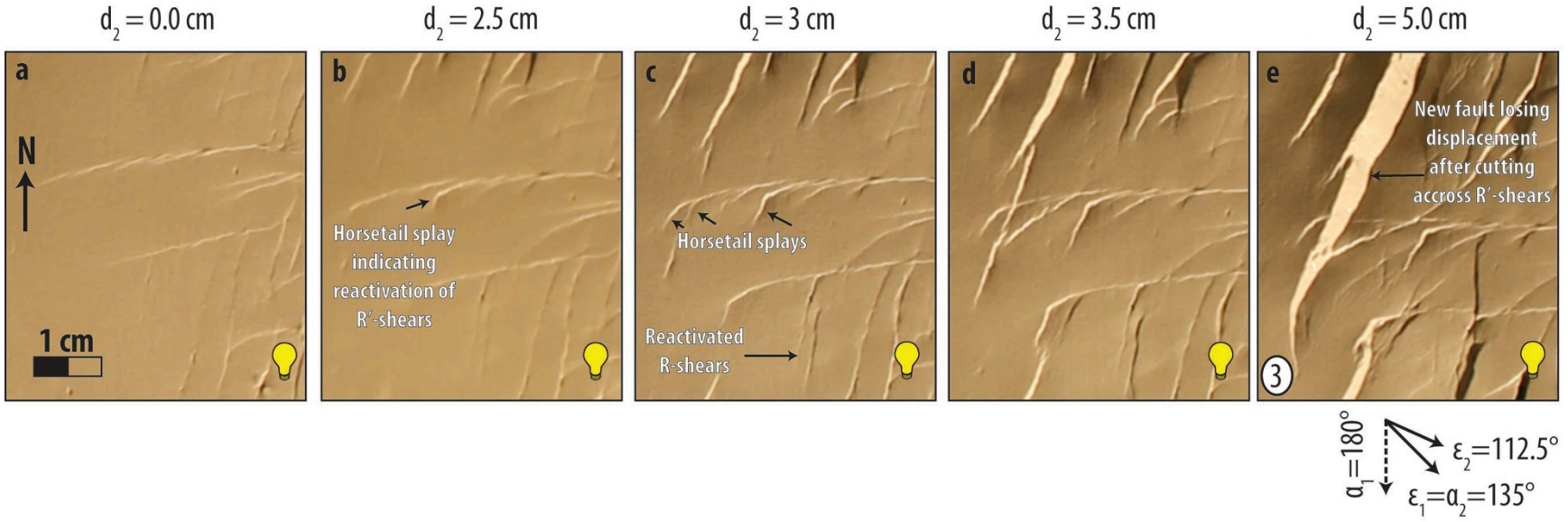

Figure 58. Example of fault interaction and reactivation during second phase of deformation in Model H (for location, see Fault 3 in Figure 55b). a) to e) Photographs of part of top surface of Model H at 0 cm, 2.5 cm, 3 cm, 3.5 cm, and 5.0 cm of displacement, respectively. Many new faults nucleate at pre-existing R'-shears and propagate away from them. Some pre-existing R-shears become more pronounced with slightly greater dip-slip component of displacement as experiment progresses, suggesting reactivation of these faults. Fault scarps dipping toward light appear bright; fault scarps dipping away from light appear dark.

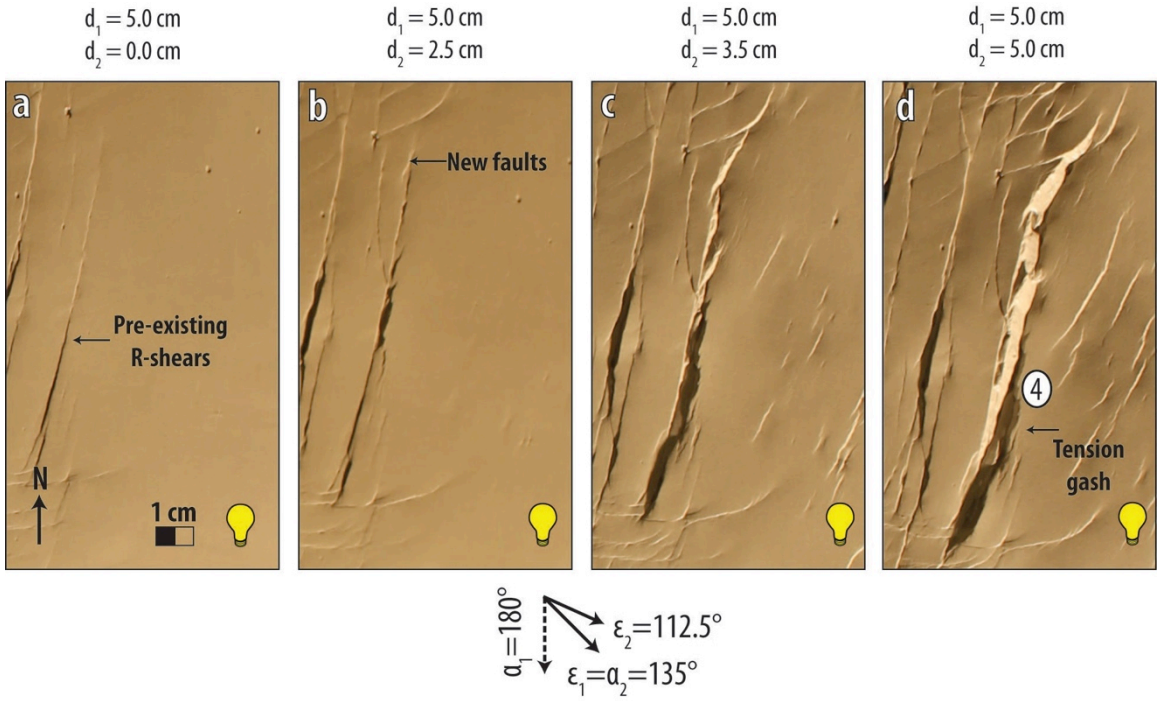

Figure 59. Formation of tension gash during second phase of deformation in Model H (for location, see Fault 4 in Figure 55b). a) to d) Photographs of part of top surface of Model H at 0 cm, 2.5 cm, 3.5 cm, and 5.0 cm of displacement, respectively, showing that R-shears pull apart and form tension gashes of as experiment progresses. Fault scarps dipping toward light appear bright; fault scarps dipping away from light appear dark.

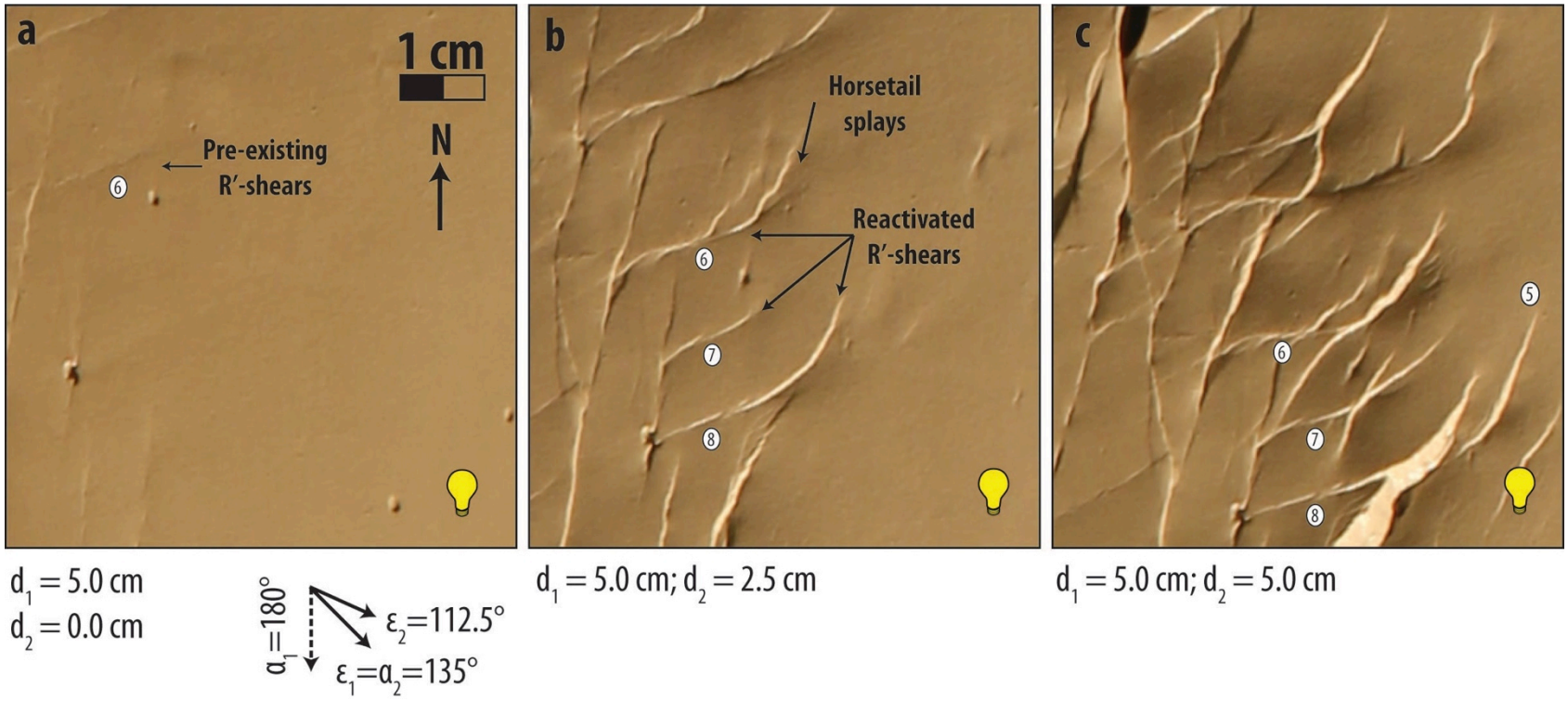

Figure 60. Reactivation of pre-existing R'-shears during second phase of deformation in Model H (for location, see Fault 5 in Figure 55b). a) to c) Photographs of part of top surface of Model H at 0 cm, 2.5 cm, and 5.0 cm of displacement, respectively. Fault 6 is an example of a pre-existing R'-shear becoming more pronounced with slightly greater dip-slip component. Horsetail splays on this fault also indicate reactivation with left-lateral strike-slip. Faults 7 and 8, which did not reach clay surface at end of first phase, presumably propagate to surface during second phase of deformation. Fault scarps dipping toward light appear bright; fault scarps dipping away from light appear dark.

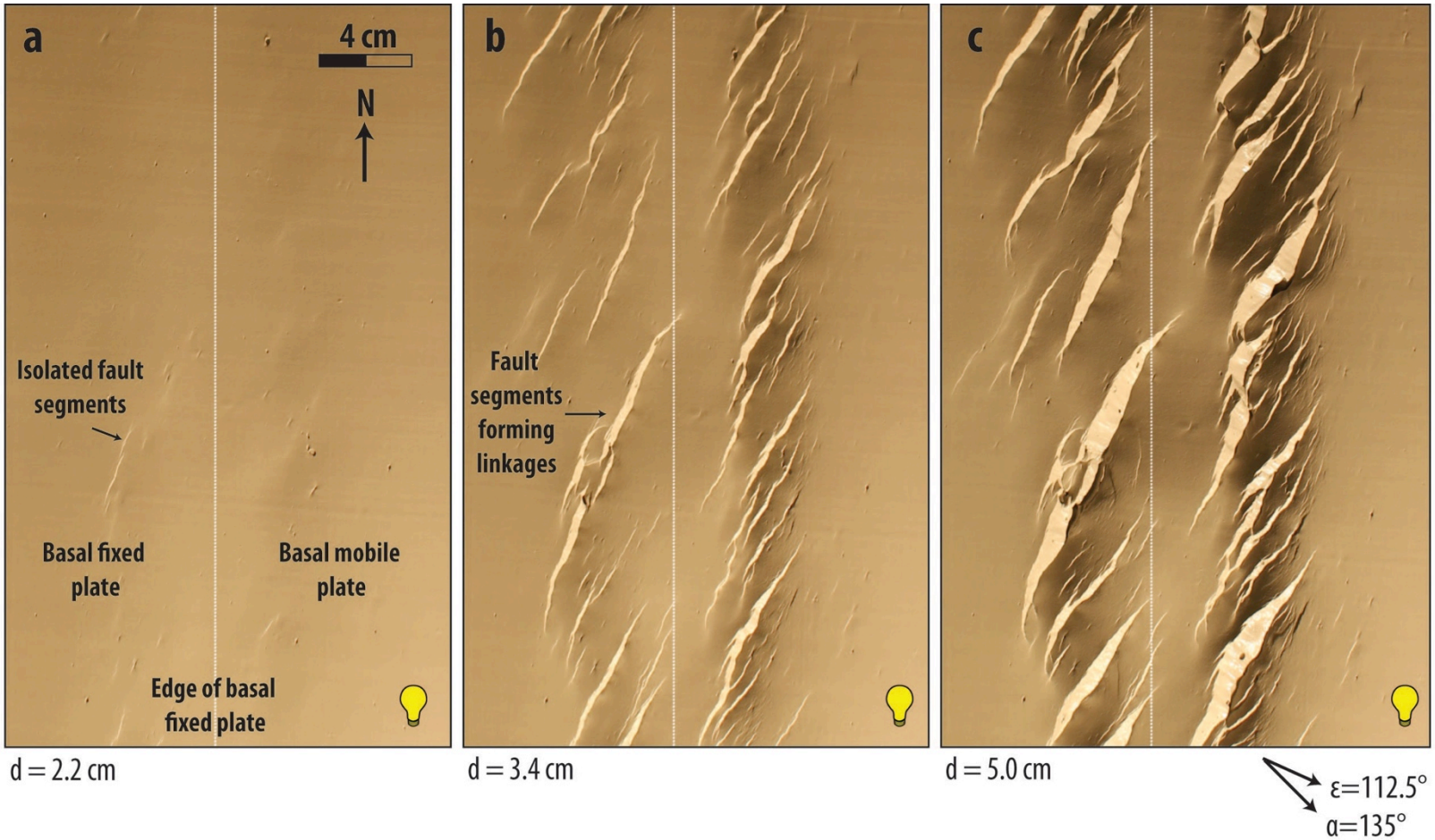

Figure 61. Evolution of faults during single phase of oblique extension in Model H1. a), b), and c) Map-view photographs of top surface at 2.2 cm, 3.4 cm, and 5 cm of displacement, respectively. Fault scarps dipping toward light appear bright; fault scarps dipping away from light appear dark. Their strike is 10° to 40° relative to the long axis of deformation. Sides of photographs are above outer edges of silicone polymer.

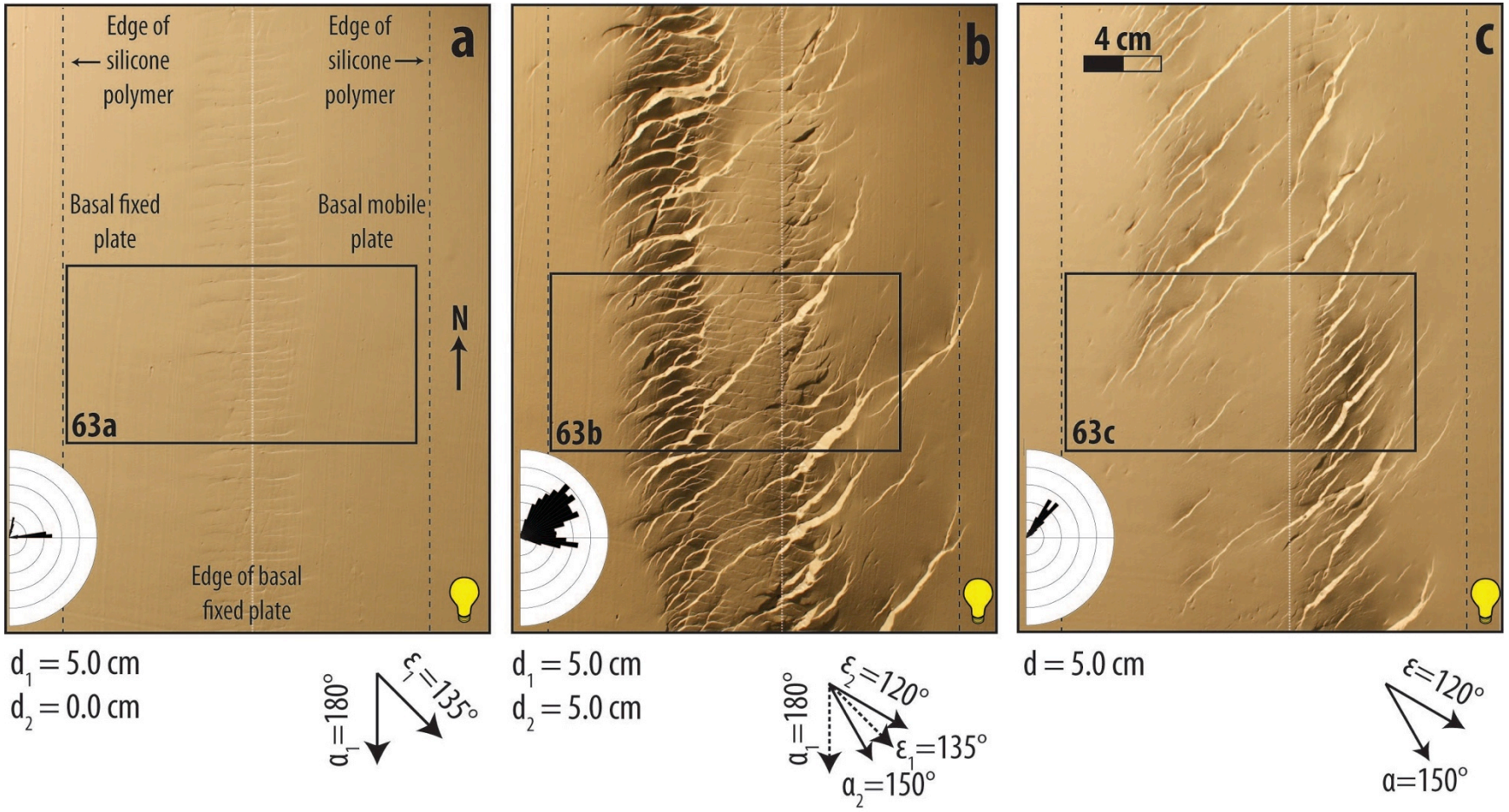

Figure 62. Map-view photographs of top surface of clay layer of Model I and Model I1. a) Model I at end of strike-slip phase of deformation. b) Model I at end of second phase of deformation. c) Model I1 at end of single phase of oblique extension. Fault scarps dipping toward light appear bright; fault scarps dipping away from light appear dark. Rose diagram shows trends of fault segments; bin size for rose diagram is 5°; outside circle of rose diagram is 120 cm. Rectangles show areas enlarged in Fig. 63.

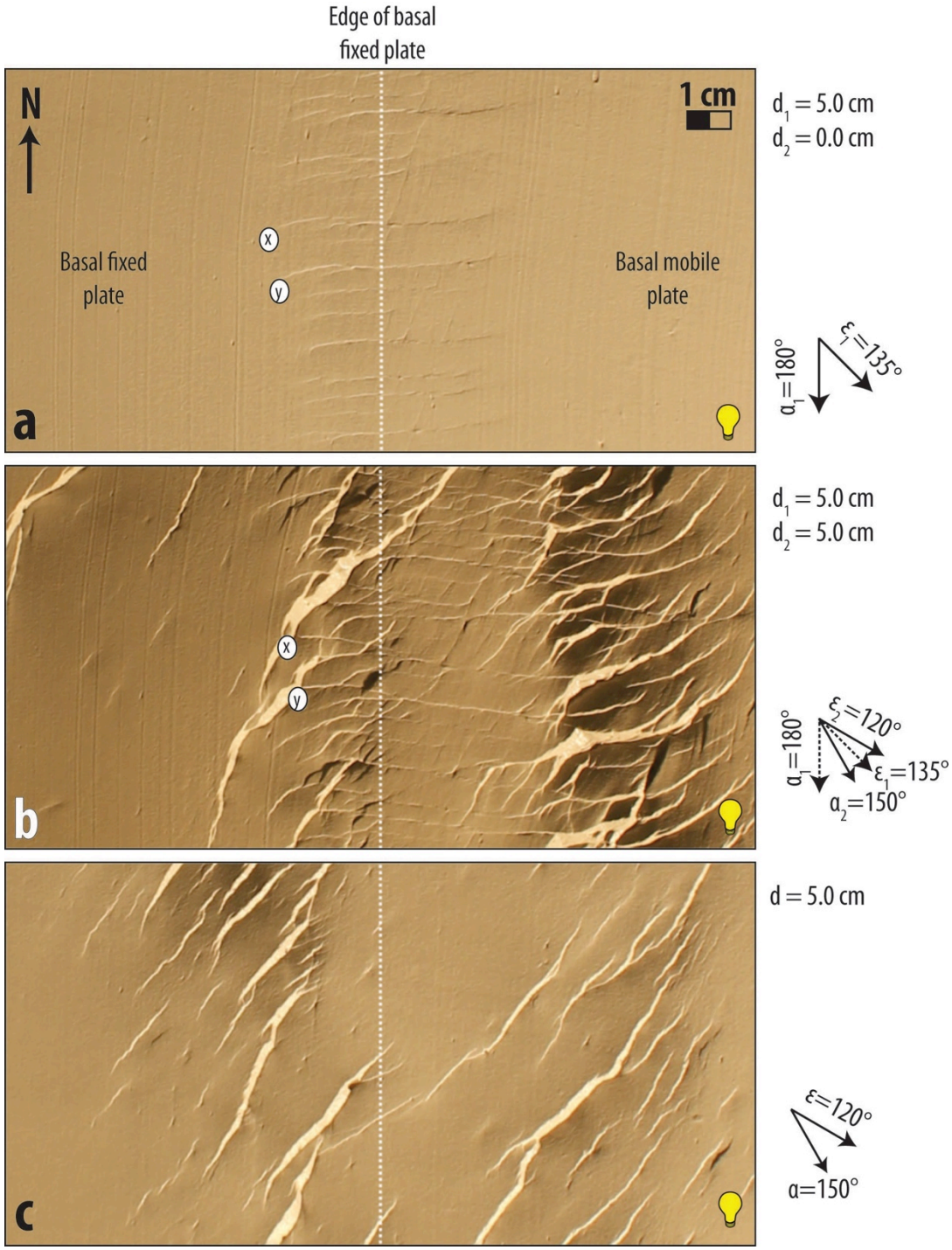

Figure 63. Close-up photographs of parts of Models I and I1 (for location, see Figure 62). a) Riedel shears present at the end of strike-slip phase of deformation in Model I. b) Fault pattern at end of second phase of deformation in Model I. Strike of all faults during second phase of deformation ranges widely from 15° to 110° clockwise relative to long axis of deformation zone. New faults lose displacement after cutting across pre-existing R'-shears. Faults x and y in part a are Faults x and y in part b. c) Fault pattern at end of deformation in Model I1. Faults strike 25° to 55° clockwise relative to the long axis of deformation zone. They have slightly less displacement than those that develop in Model I. Fault scarps dipping toward light appear bright; fault scarps dipping away from light appear dark.

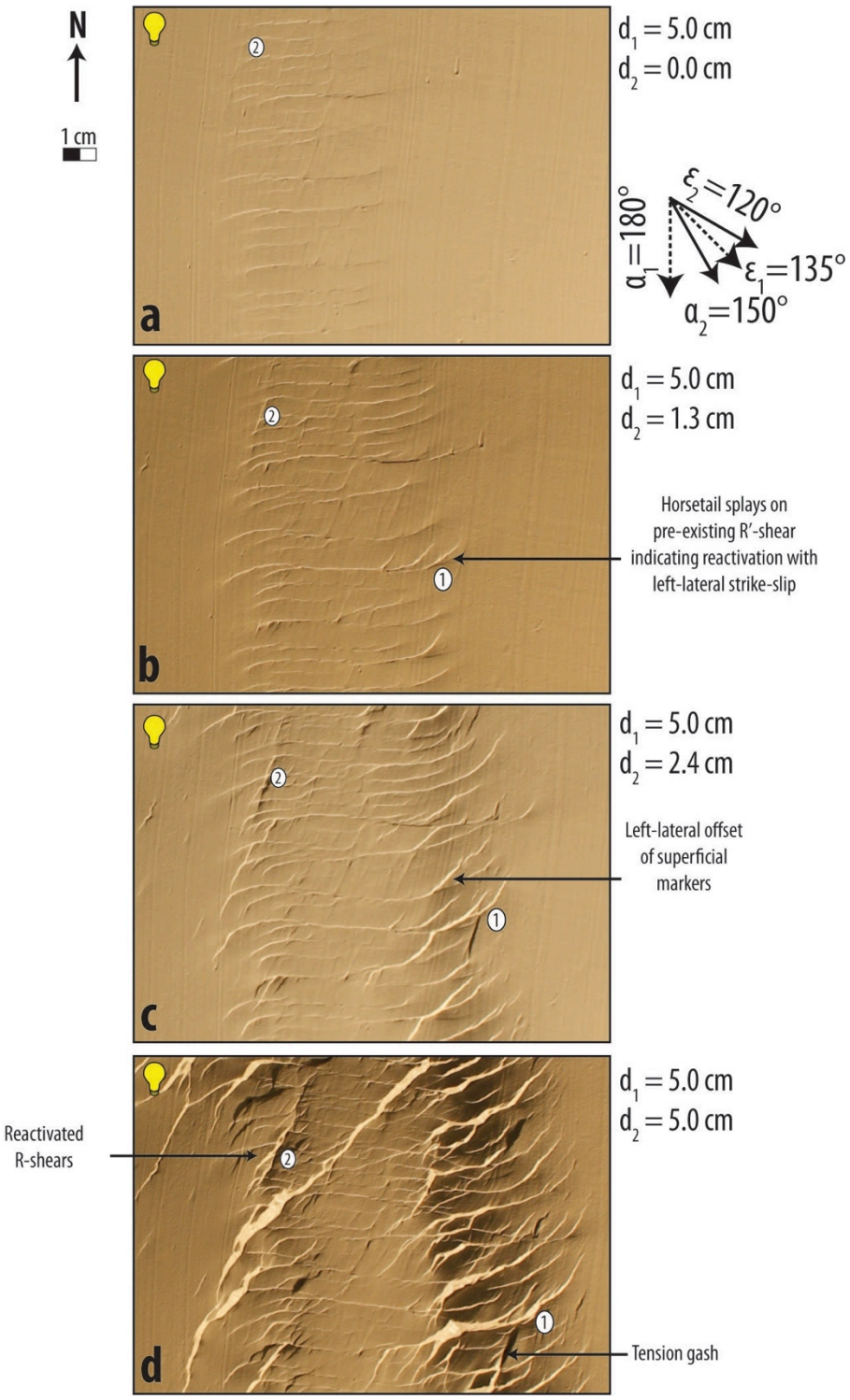

Figure 64. Evolution of faults during second phase of deformation in Model I. a) to d) Photographs of part of top surface at 0 cm, 1.3 cm, 2.4 cm, and 5.0 cm of displacement, respectively. Offset of superficial markers and horsetail splays on pre-existing R'-shears indicate that R'-shears are reactivated with left-lateral strike-slip (e.g., Fault 1). Fault 2 is an example of pre-existing R-shear becoming more pronounced with slightly greater dip-slip component. New faults lose displacement as they encounter first-phase deformed zone. Fault scarps dipping toward light appear bright; fault scarps dipping away from light appear dark.

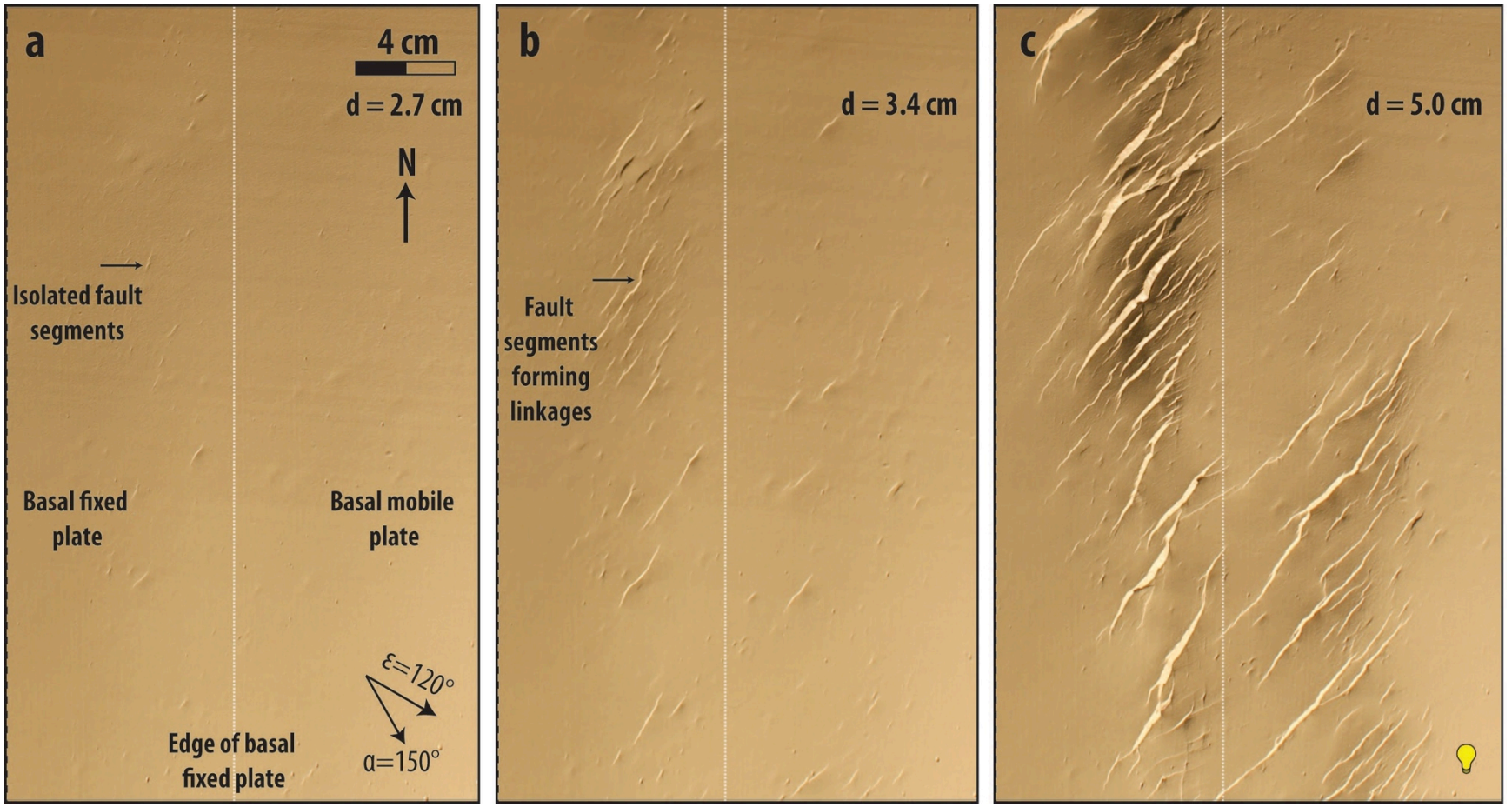

Figure 65. Evolution of faults during single phase of oblique extension in Model I1. a), b), and c) Map-view photographs of top surface of Model I1 at 2.7 cm, 3.4 cm, and 5 cm of displacement, respectively. Fault scarps dipping toward light appear bright; fault scarps dipping away from light appear dark. Their strike is 25° to 55° relative to long axis of deformation. Sides of photographs are above outer edges of silicone polymer.

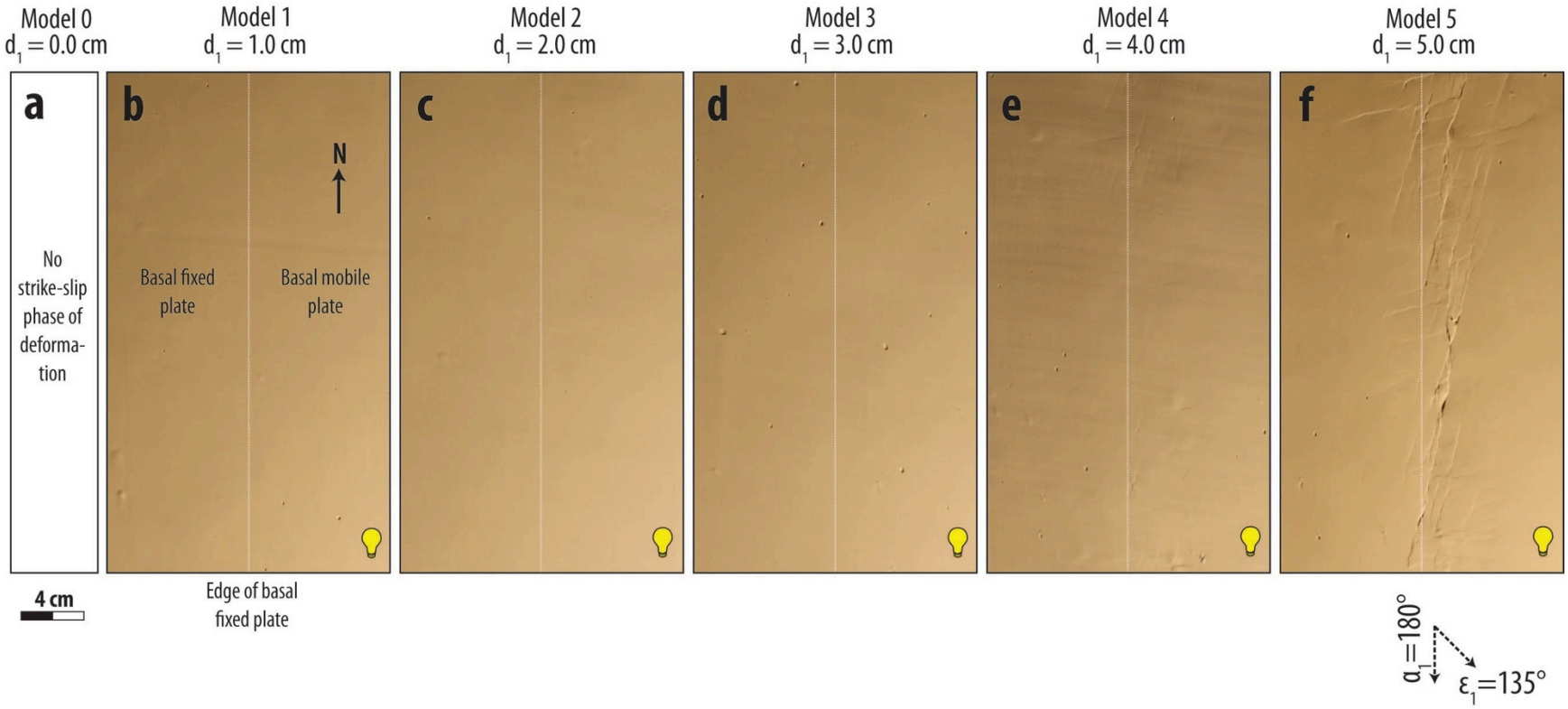

Figure 66. First-phase deformation pattern in all Series 2 models. a) Model 0 does not undergo initial strike-slip deformation. b) to f) Photographs of top surface of Models 1 to 5 at end of strike-slip phase of deformation. In Models 1 to 3 (d_1 = 1 to 3 cm), the clay surface is deformed but not faulted. In Model 4 (d_1 = 4 cm), a few R- and R'-shears develop at the edge of the model. In Model 5 (d_1 = 5 cm), numerous R- and R'-shears develop above the silicone polymer and the edges of the overlapping plates. The R- and R'-shears in Models 4 and 5 strike 10°-20° and 80°-90° clockwise relative to the long axis of deformation zone. Fault scarps dipping toward light appear bright; fault scarps dipping away from light appear dark. Dotted white line represents edge of basal fixed plate. Sides of photographs are the edges of silicone polymer beneath the clay layer.

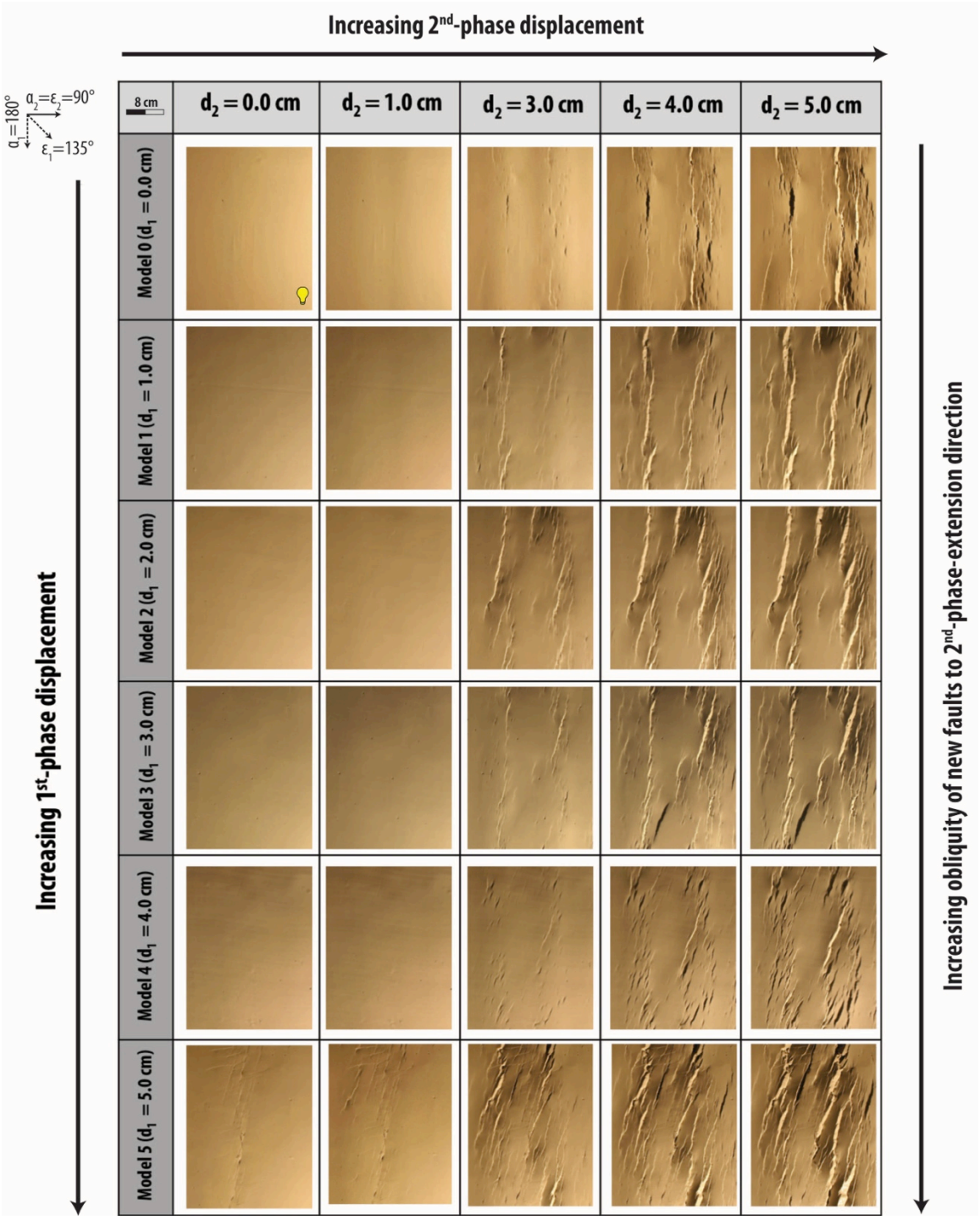

Figure 67. Evolution of fault patterns during second phase of deformation (orthogonal extension) for increasing magnitudes of displacement. As the displacement magnitude of the first phase increases, the strike of most faults in the second phase of deformation becomes more oblique to the second-phase extension direction and more subparallel to the R-shear orientation. Fault scarps dipping toward light appear bright; fault scarps dipping away from light appear dark. Lighting directions are identical in all photographs.

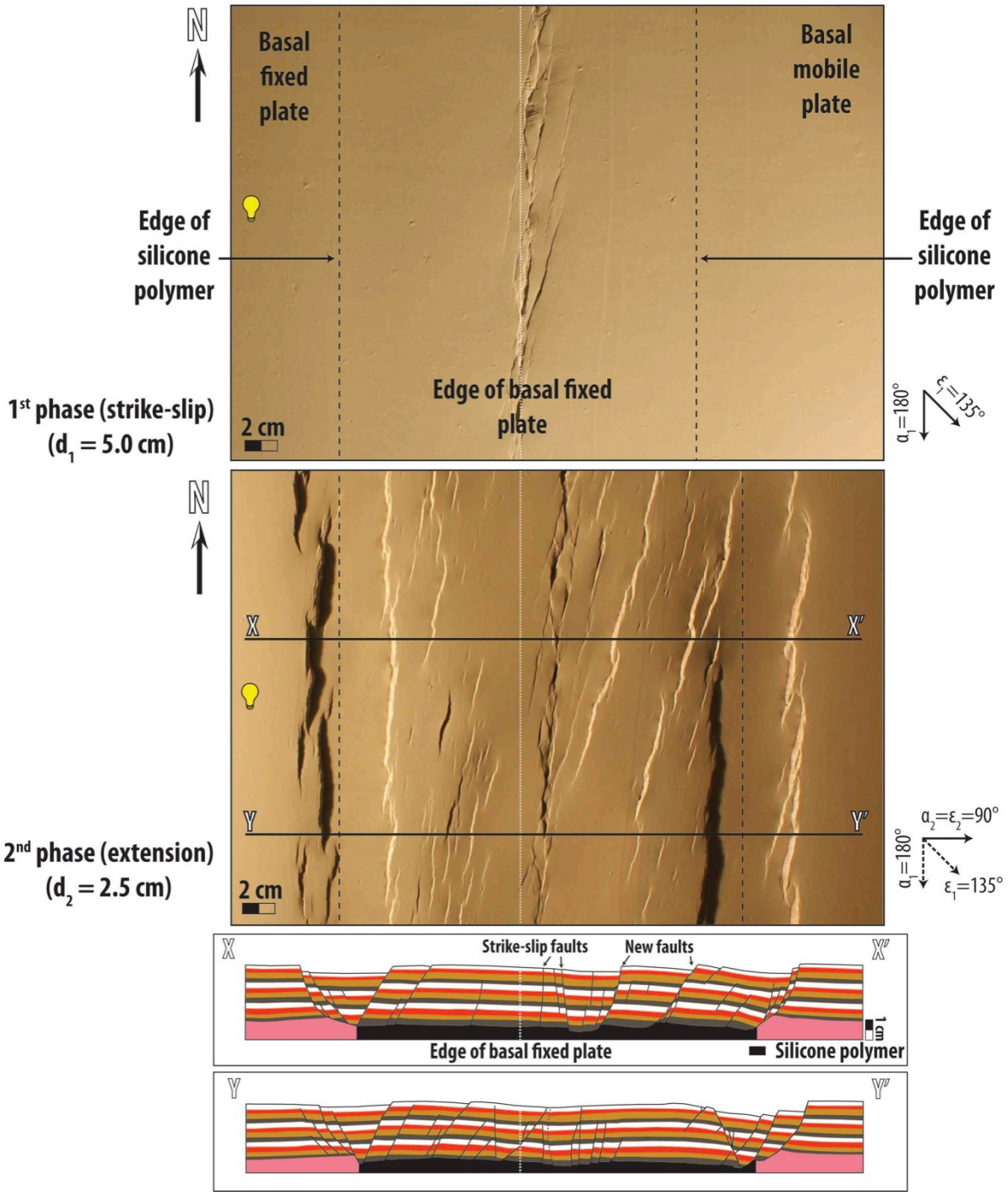

Figure 68. Map-view photographs of top surface of layered clay model after: a) strike-slip phase of deformation, and b) second phase of extension. Fault scarps dipping toward light appear bright; fault scarps dipping away from light appear dark. Cross sections X-X' (c) and Y-Y' (d) are from the central part of the model (see part b). Strike-slip faults have very steep dip, but are not necessarily vertical. New faults have relatively moderate to steep dip. More faults are present at the base of the clay than at the top of the clay.

Figure 69. Summary of modeling results for Series 1 models. Photos in left column show fault patterns at end of first phase of deformation (strike-slip); photos in right column show fault patterns at end of second phase of deformation (extensional). Both fault reactivation and the formation of new faults (also see Figure 2) occur during the second phase of deformation in all models. Fault scarps dipping toward light appear bright; fault scarps dipping away from light appear dark. Circled letters highlight the same faults in both phases. Rose diagrams show strikes of fault segments; bin size for rose diagram is 5°; outside circle of rose diagram is 120 cm. Arrows indicate maximum extension direction (ε) and displacement direction (α). Dotted white lines represent edge of basal fixed plate.

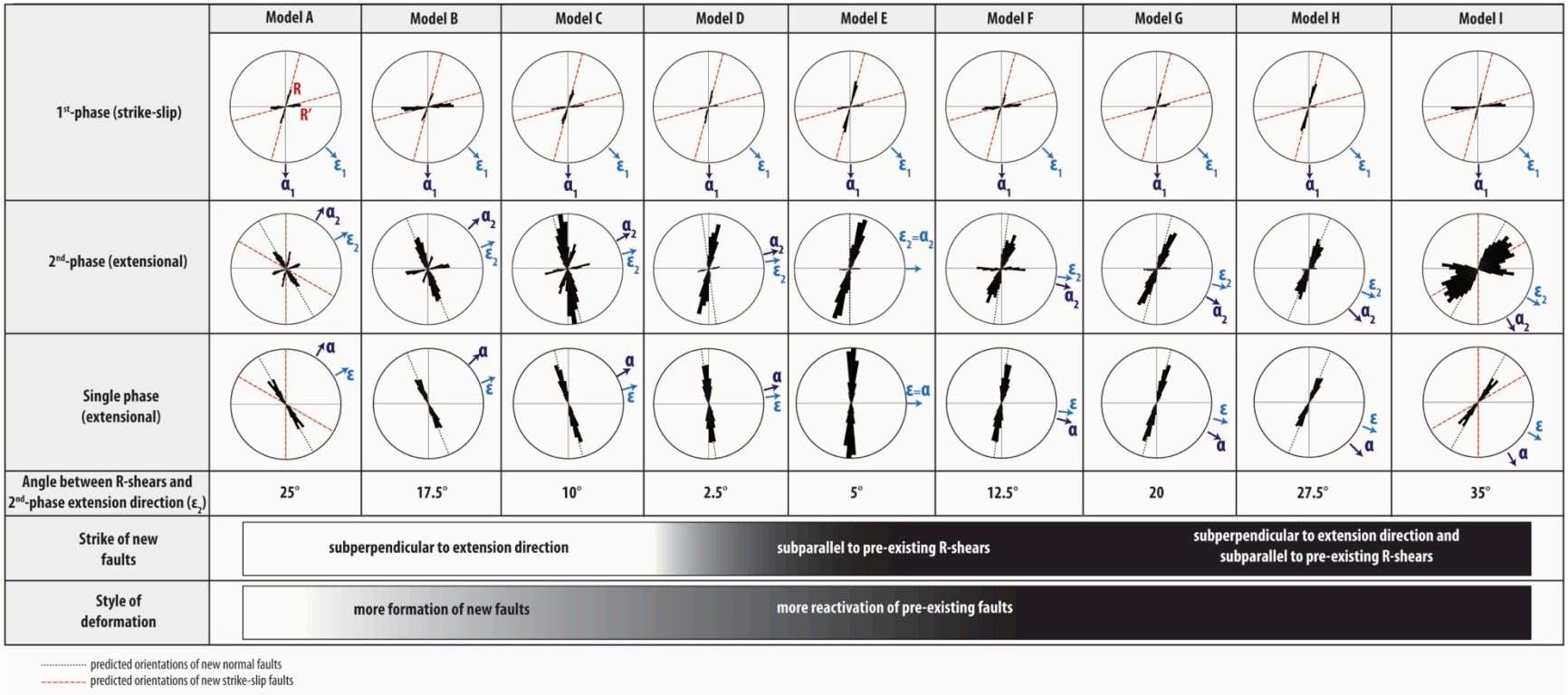

Figure 70. Summary of fault strikes for all Series 1 models. Rose diagrams show strikes of fault segments at end of strike-slip phase of deformation (top row) and at end of second phase of deformation (bottom row); bin size for rose diagram is 5°; outside circle of rose diagram is 120 cm. Dotted line shows predicted strike of new normal faults (perpendicular to ε_2 direction) in all models. Dashed line shows predicted strike of new strike-slip faults in Models A and I (ε_2 direction bisects the obtuse angle between the conjugate fault strikes). During the second phase of deformation in Models A and I, either σ_1 or σ_2 could be vertical (Withjack & Jamison, 1986); thus, two possible stress states (normal or strike-slip faulting) may occur. σ_1 is vertical in Models B to H; thus, only a normal-faulting stress state exists. New faults that develop during the second phase of deformation fall into three categories based on their orientation: 1) new faults that strike subperpendicular to the maximum extension direction in Models A to C, 2) new faults that are subparallel to the strike of the pre-existing R-shears in Models D to F, and 3) new faults that are subparallel to the strike of the pre-existing R-shears and/or subperpendicular to the second-phase extension direction in Models G to I. Formation of new faults mostly occurs in models in which $\alpha_2<60°$ ($\varepsilon_2<75°$; Models A to C). In models in which $\alpha_2>60°$ ($\varepsilon_2>75°$), reactivation of pre-existing R- and/or R'-shears accommodate most deformation

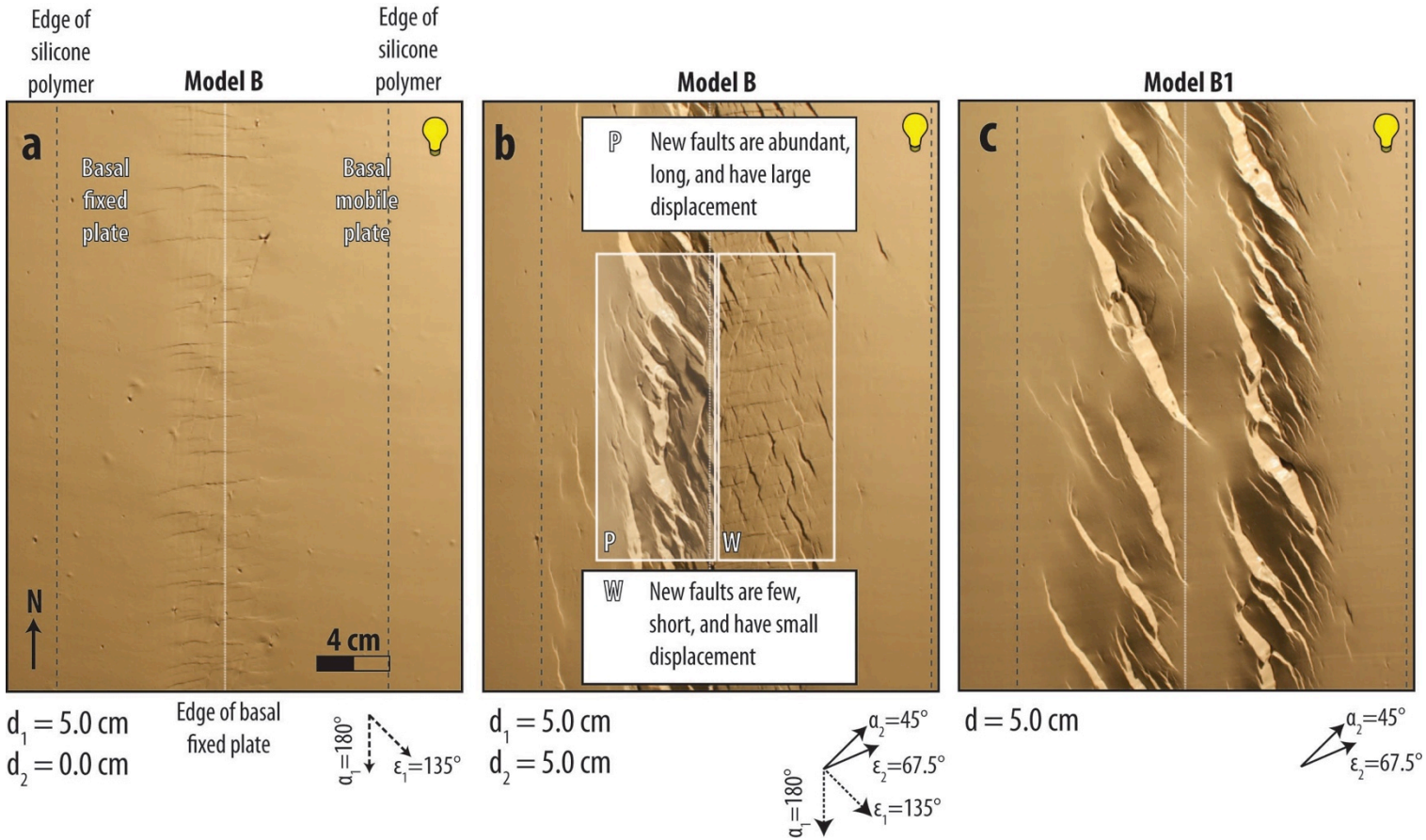

Figure 71. Influence of pre-existing high-angle fault population on the distribution of new faults. a) Photograph of top surface of Model B at end of strike-slip phase of deformation. Pre-existing high-angle fault population develop above edge of basal fixed plate. b) Photograph of top surface of Model B at end of second phase of deformation. A well-developed, pre-existing high-angle fault population inhibits development of new faults, perhaps by serving as lateral obstacles. Where pre-existing faults are less developed, new faults are abundant, long, and have large displacements. Where pre-existing faults are better developed, new faults are fewer, shorter, and have less displacement than those that develop where pre-existing faults are better developed. c) Photograph of top surface of Model B1. Faults in this model are geometrically similar to those that develop where the pre-existing fault population is poorly developed in Model B.

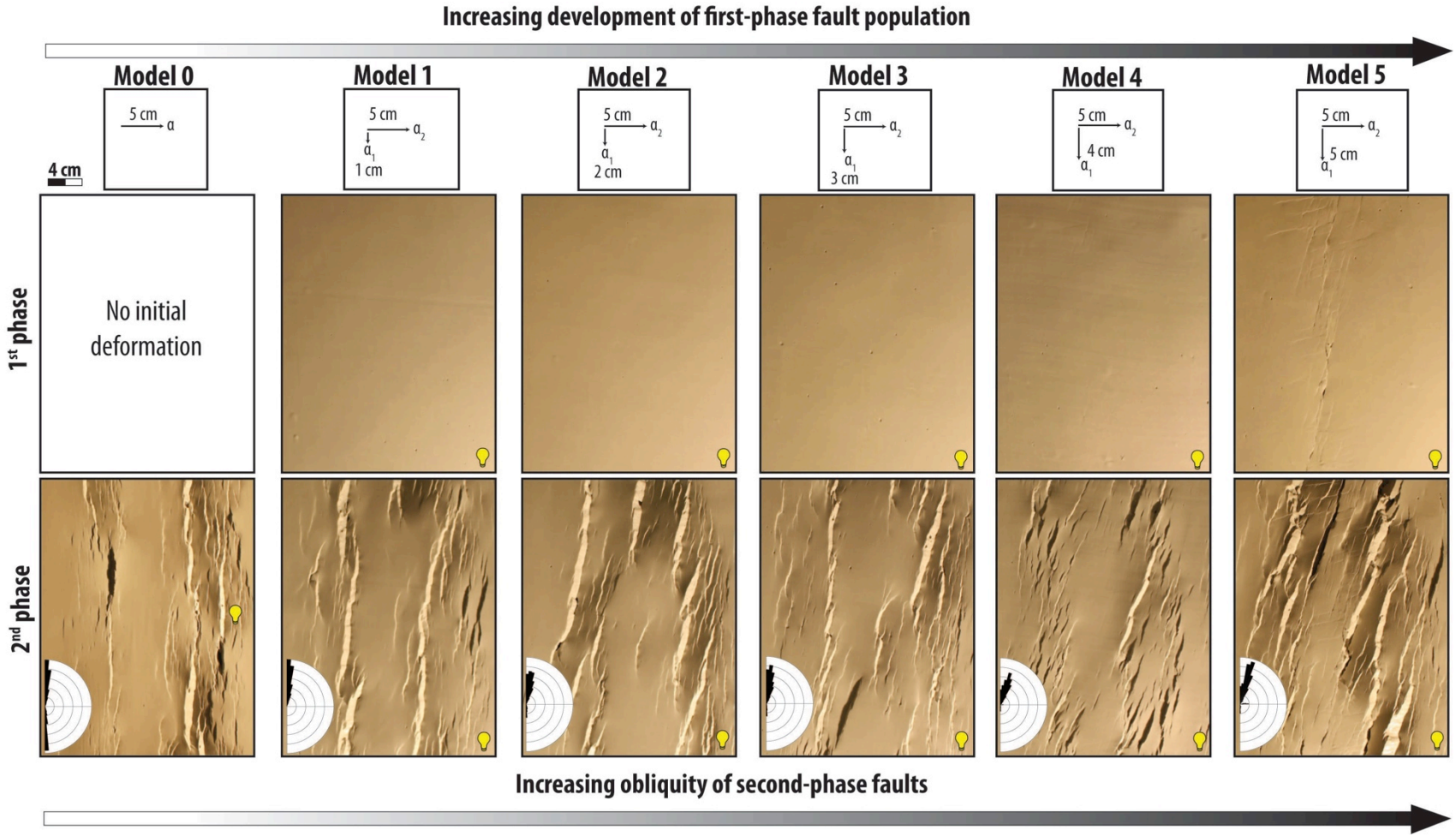

Figure 72. Summary of modeling results for Series 2 models showing that new faults increasingly become parallel to the orientation of R-shears as the first-phase fault population becomes better developed. Top row of photos shows fault pattern after the strike-slip phase of deformation; bottom row of photos shows fault pattern after second phase of extensional deformation. Fault scarps dipping toward light appear bright; fault scarps dipping away from light appear dark. Rose diagram shows trends of fault segments; bin size for rose diagram is 5°; outside circle of rose diagram is 120 cm.

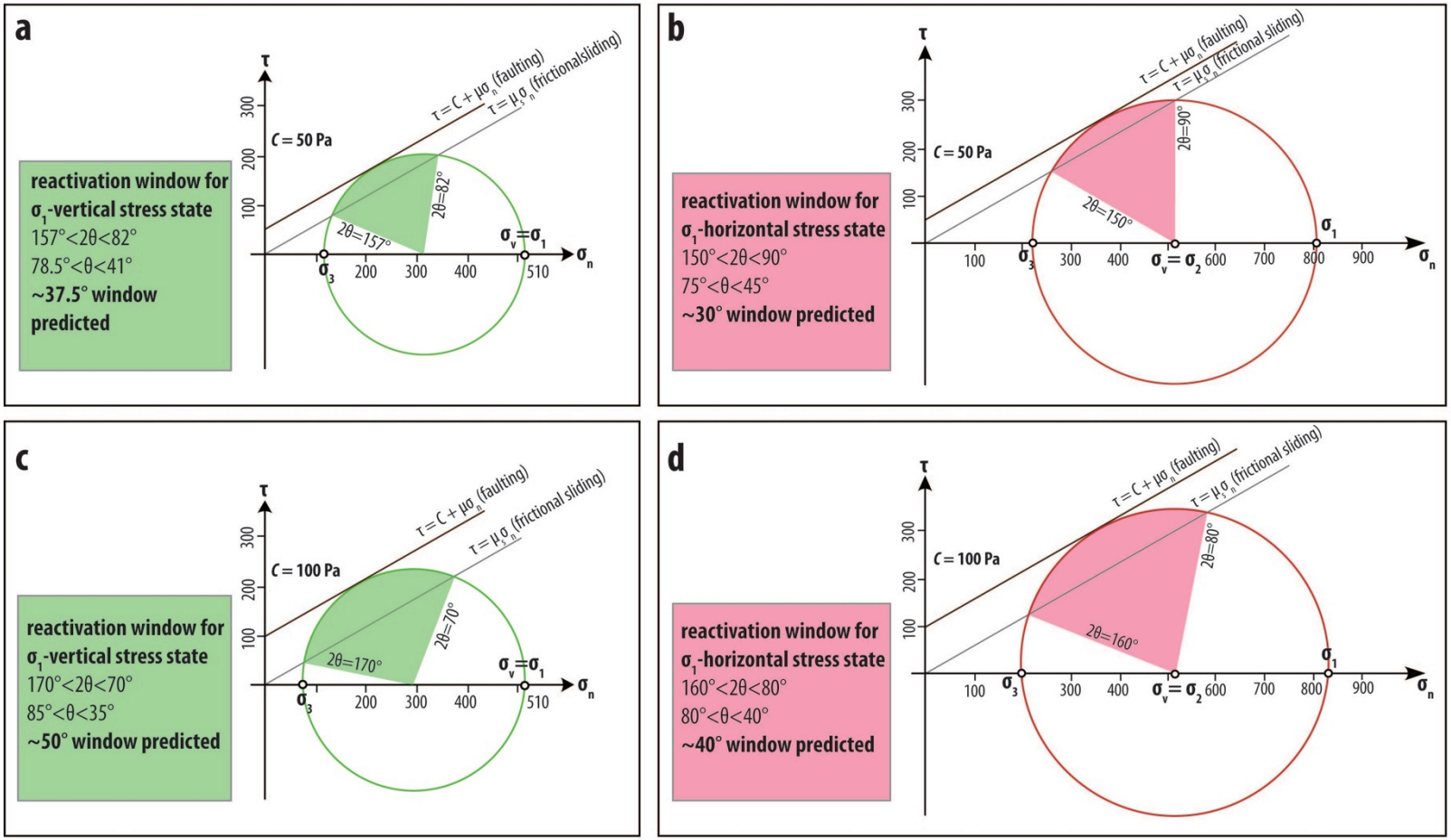

Figure 73. Mohr-circle diagram showing predicted range of fault orientations (specified by θ, the angle between σ_1 and the normal to the fault plane) for reactivation in a) σ_1-vertical stress state (green shading) and b) σ_1-horizontal stress state (pink shading). The value for the coefficient of sliding friction for clay is unknown but, like Henza et al. (2010), I assume that the frictional-sliding envelop parallels the Mohr-Coulomb failure envelop for undeformed clay ($\mu \sim 0.6$ and $C \sim 50$ Pa). τ and σ_n are, respectively, shear and normal stress on a potential fault surface. C is cohesive strength. μ is coefficient of internal friction. μ_s is coefficient of sliding friction along fault plane (once a fault surface develops). The value C is not well constrained, so I also show the Mohr diagrams for $C \sim 100$ Pa (c and d), which produces a larger reactivation window and is used in subsequent figures. For the σ_1-vertical stress state, the value for σ_v (σ_1) is 510 Pa; I draw the largest Mohr circle that is tangent to the Mohr-Coulomb (faulting) failure envelop. For the σ_1-horizontal stress state, $\sigma_v = \sigma_2 = 510$ Pa, and I assume that σ_2 lies midway between σ_1 and σ_3; I draw the largest circle that satisfies these constraints and is tangent to the Mohr-Coulomb (faulting) failure envelop. Note that the reactivation window (defined by where the Mohr circle intersects the frictional sliding failure envelop) for a σ_1-vertical stress state is larger than for a σ_1-horizontal stress state. I only show failure envelopes and reactivation windows for positive shear stresses.

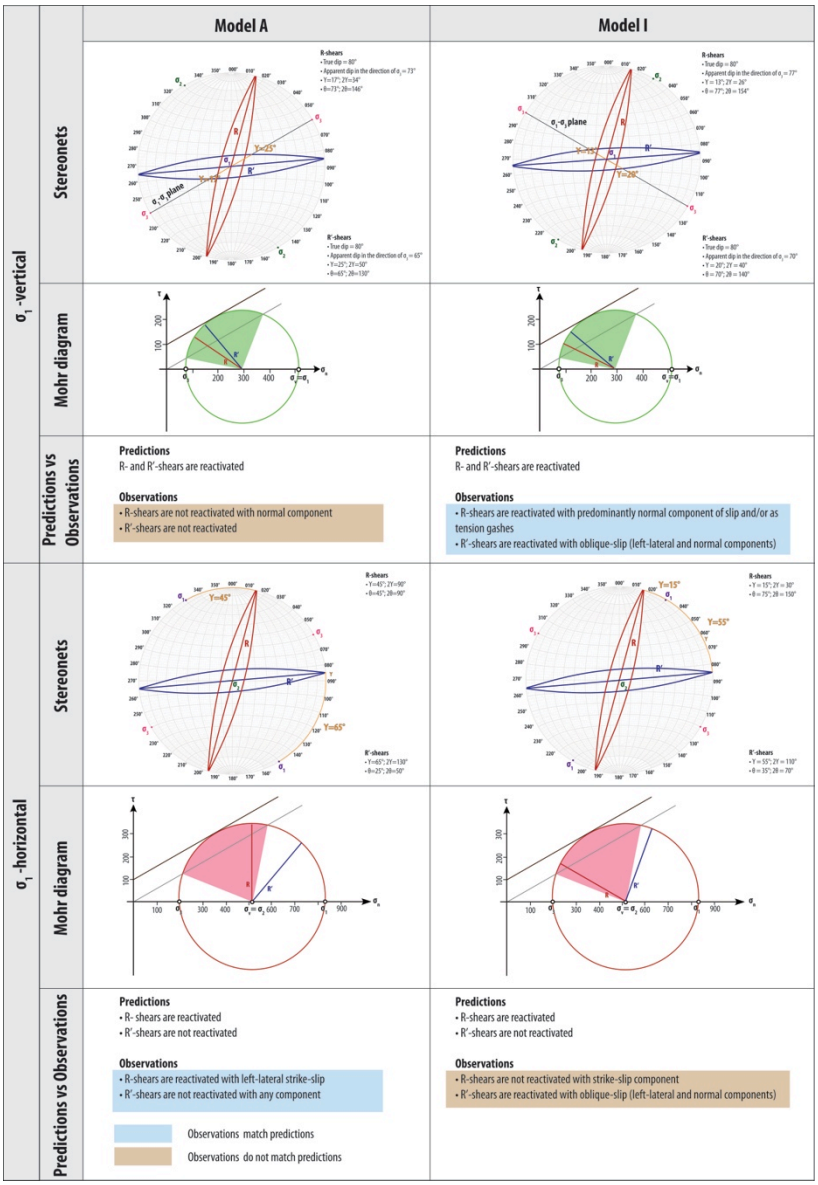

Figure 74. Prediction of fault reactivation for Models A and I for which two stress states (σ_1-vertical and σ_1-horizontal) are possible (Withjack & Jamison, 1986). The top row shows stereographic plots of the principal stresses for a σ_1 vertical stress state and the average orientation of R-shears (striking 015° and dipping 80°, based on cross sections of the layered model) and R'-shears (striking 085° and dipping 80°). The angle θ is measured in the plane containing σ_1 and σ_3, and is therefore related to the apparent dip of the faults and the complimentary angle, γ, the angle between σ_1 and the fault plane. The second row shows the calculated values of θ for the average R- and R'-shear doubled to 2θ and plotted on a Mohr circle (using the parameters from Figure 73c). Note that both R- and R'-shears fall into the reactivation window (green) for the σ_1 stress state for both Models A and I. The fourth row shows stereographic plots of the principal stresses for a σ_1-horizontal stress state and the average orientation of R- and R'-shears. γ is the angle between σ_1 and the fault strike measured in the σ_1-σ_3 plane, the perimeter of the stereonet; θ=90°- γ. The fifth row shows the calculated values of θ for the average R- and R'-shear doubled to 2θ and plotted on a Mohr circle (using the parameters from Figure 73d). The predictions of σ_1-horizontal stress state better matches the observations from Model A than do the predictions of the σ_1=vertical stress state. The predictions of σ_1-vertical stress state better matches the observations from Model I than do the predictions of the σ_1 horizontal stress state.

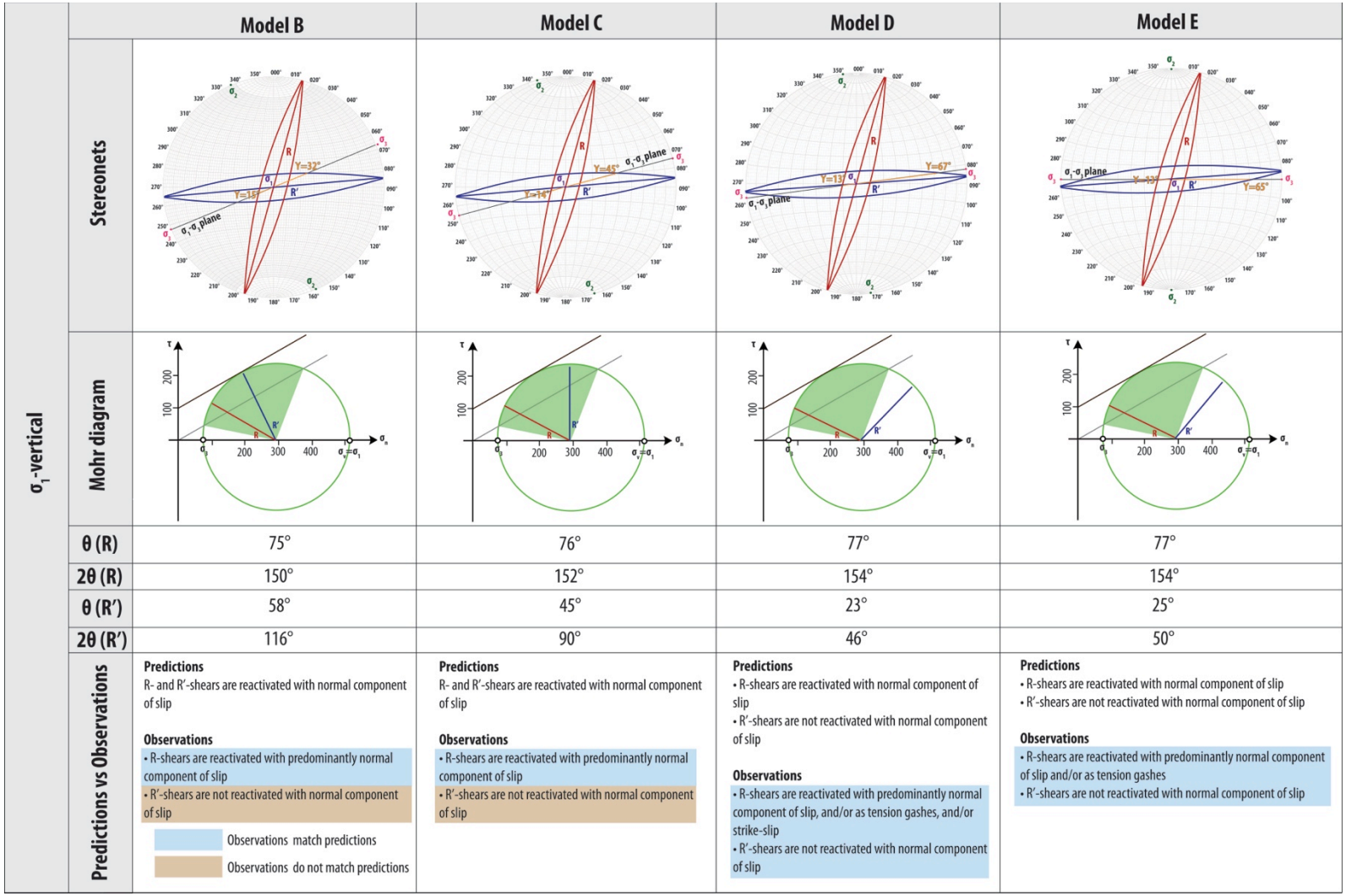

Figure 75. Caption is on next page

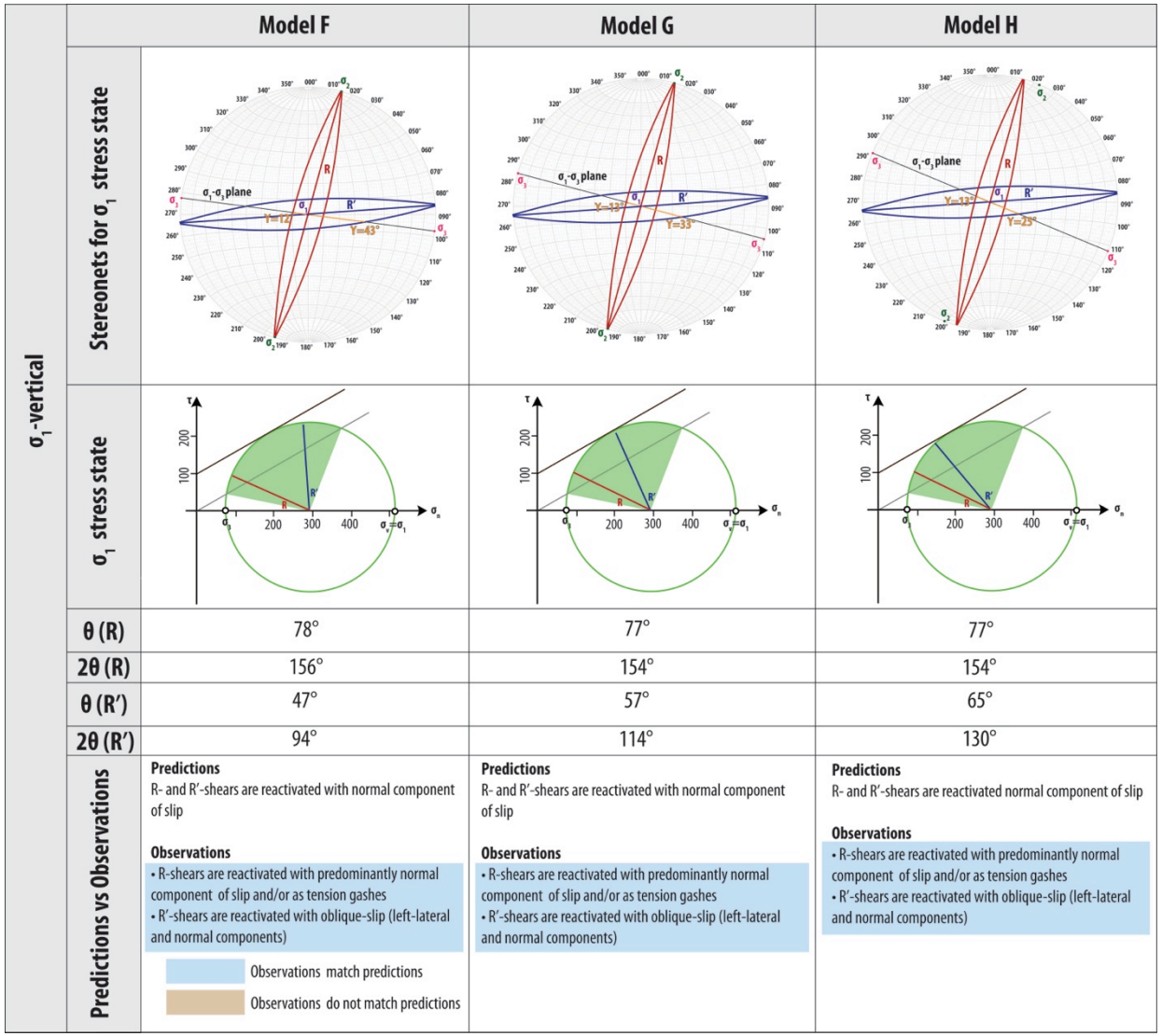

Figure 75. Prediction of fault reactivation for Models B to H. Top row shows stereographic plots of the principal stresses and the average orientation of R-shears (striking 015° and dipping 80°, based on cross sections of the layered model) and R'-shears (striking 085° and dipping 80°). The angle θ is measured in the plane containing σ_1 and σ_3, and is, therefore, related to the apparent dip of the faults and the complimentary angle, γ, the angle between σ_1 and the fault plane. Second row shows the calculated values of θ for the average R- and R'-shears doubled to 2θ and plotted on a Mohr circle (using the parameters from Figure 73c). Note that the R-shears fall into the predicted reactivation window (green) for all models. The R'-shears fall into the predicted reactivation window (green) for all models except D and E. Observations corroborate predictions for all cases except for the R'-shears in Models B and C.

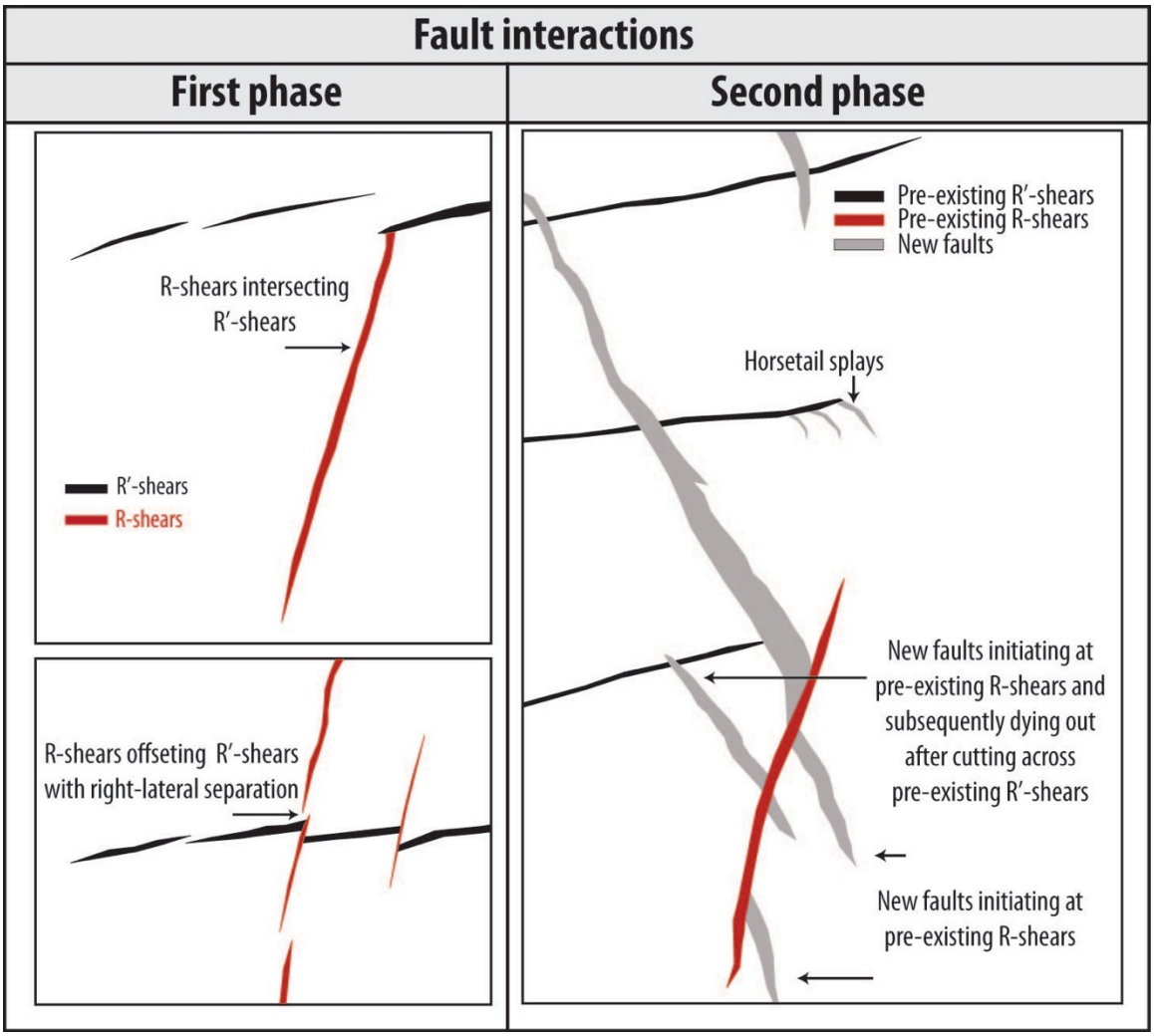

Figure 76. Fault interactions during first phase (strike-slip) and second phase (extension) of deformation. During the first phase of deformation (strike-slip), the R-shears offset the R'-shears with right-lateral separation. They also intersect the R'-shears. During the second phase of deformation (extension), new faults may initiate at R- and/or R'-shears and propagate away from them. New faults that nucleate at the pre-existing faults, however, are usually short. The new faults may also lose displacement after cutting across the pre-existing high-angle faults

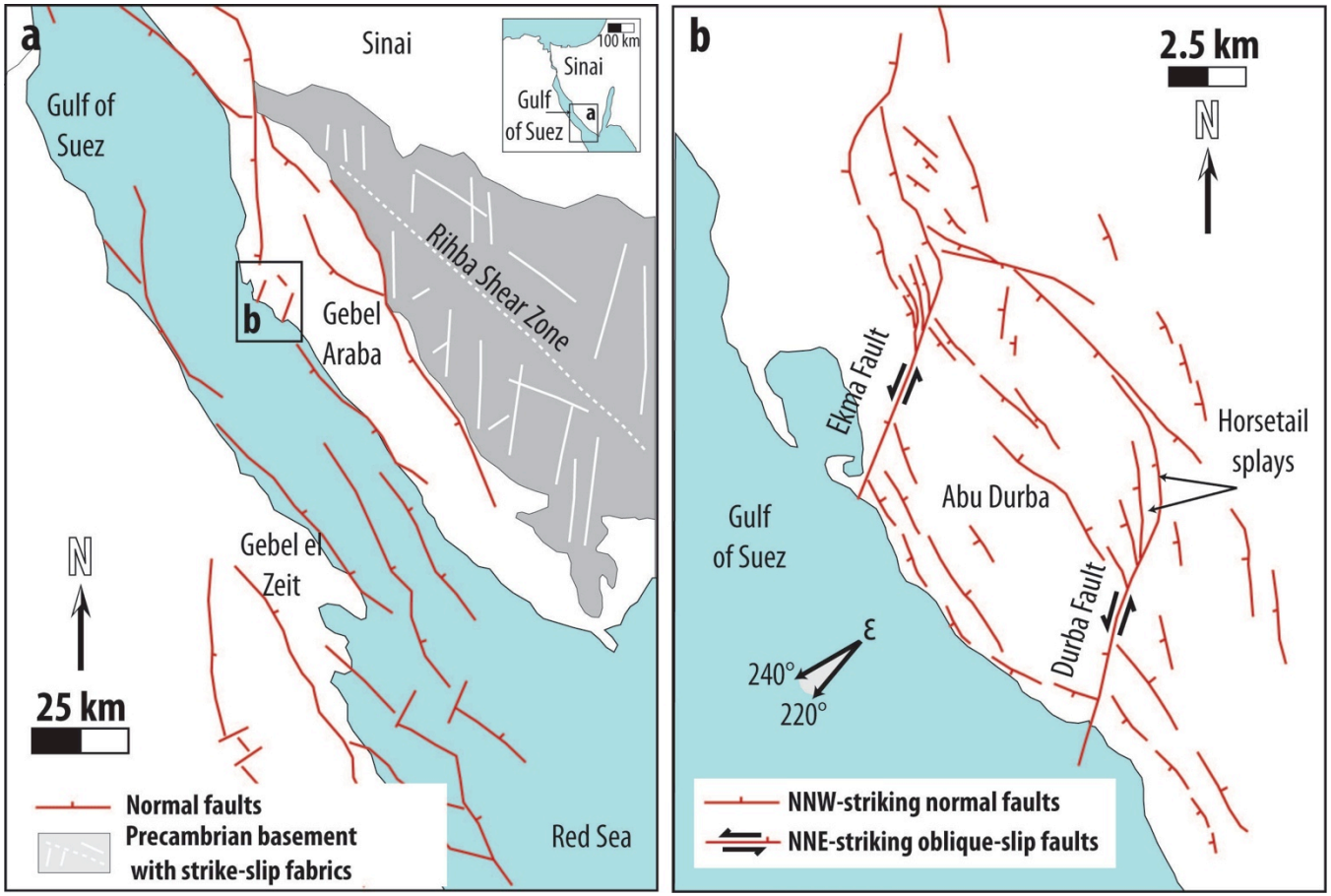

Figure 77. Fault pattern (a) from the Gulf of Suez showing major faults and shear zone (see inset map for location) and (b) Abu Durba area of the southern part of the Suez rift (see inset map in part a for location) (modified from McClay and Khalil, 1998; Younes and McClay, 2002). Part a shows strike-slip faults with two dominant orientations (NNE and WNW) developed in Rihba shear zone during Precambrian. Part b shows that new faults developed during Oligocene-Miocene rifting. These faults strike subparallel to Precambrian WNW-striking faults in part a. Durba and Ekma faults were reactivated during rifting with oblique-slip (left-lateral and normal) component. Extension direction (ε) range is given by largest petal of rose diagram of "coastal faults" in figure 10 of Younes and McClay (2002).

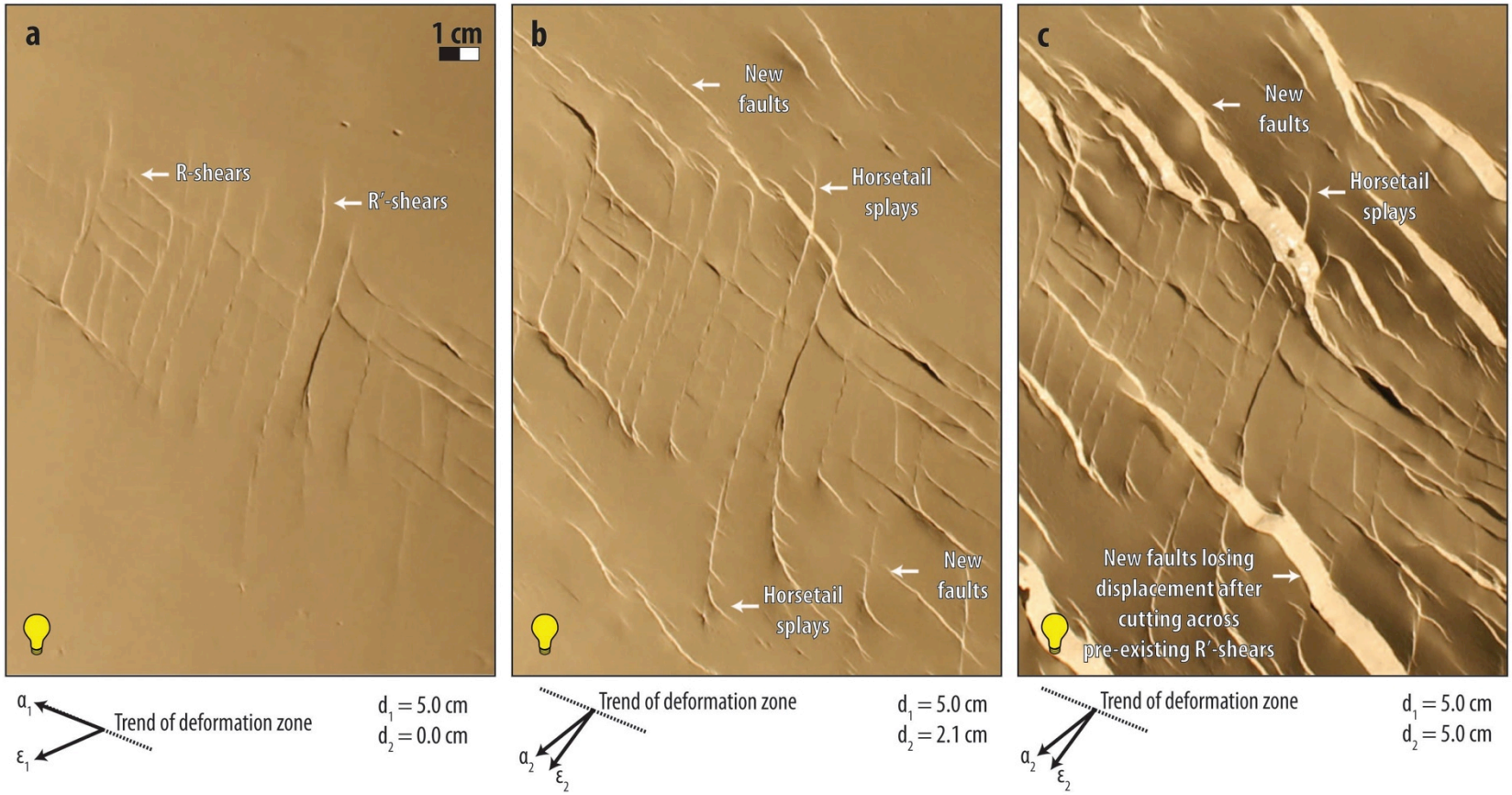

Figure 78. Map-view photographs of top surface of clay layer of Model G (reoriented to match the fault orientations from the Suez rift) at: a) end of strike-slip phase of deformation, b) 2.1 cm of displacement during second phase of deformation, and c) end of second phase of defomation. In Model G, pre-existing high-angle R'-shears are reactivated as oblique-slip faults with normal and left-lateral strike-slip during the second phase of deformation (oblique extension, ε_2=120°, relative to the trend of deformation zone). These reactivated high-angle R-shears impede the propagation of new normal faults. The new faults lose their displacement after they encounter the reactivated high-angle R'-shears. Horsetail splays at the termination of the R'-shears also form linkages with the new faults. Fault scarps dipping toward light appear bright; fault scarps dipping away from light appear dark.

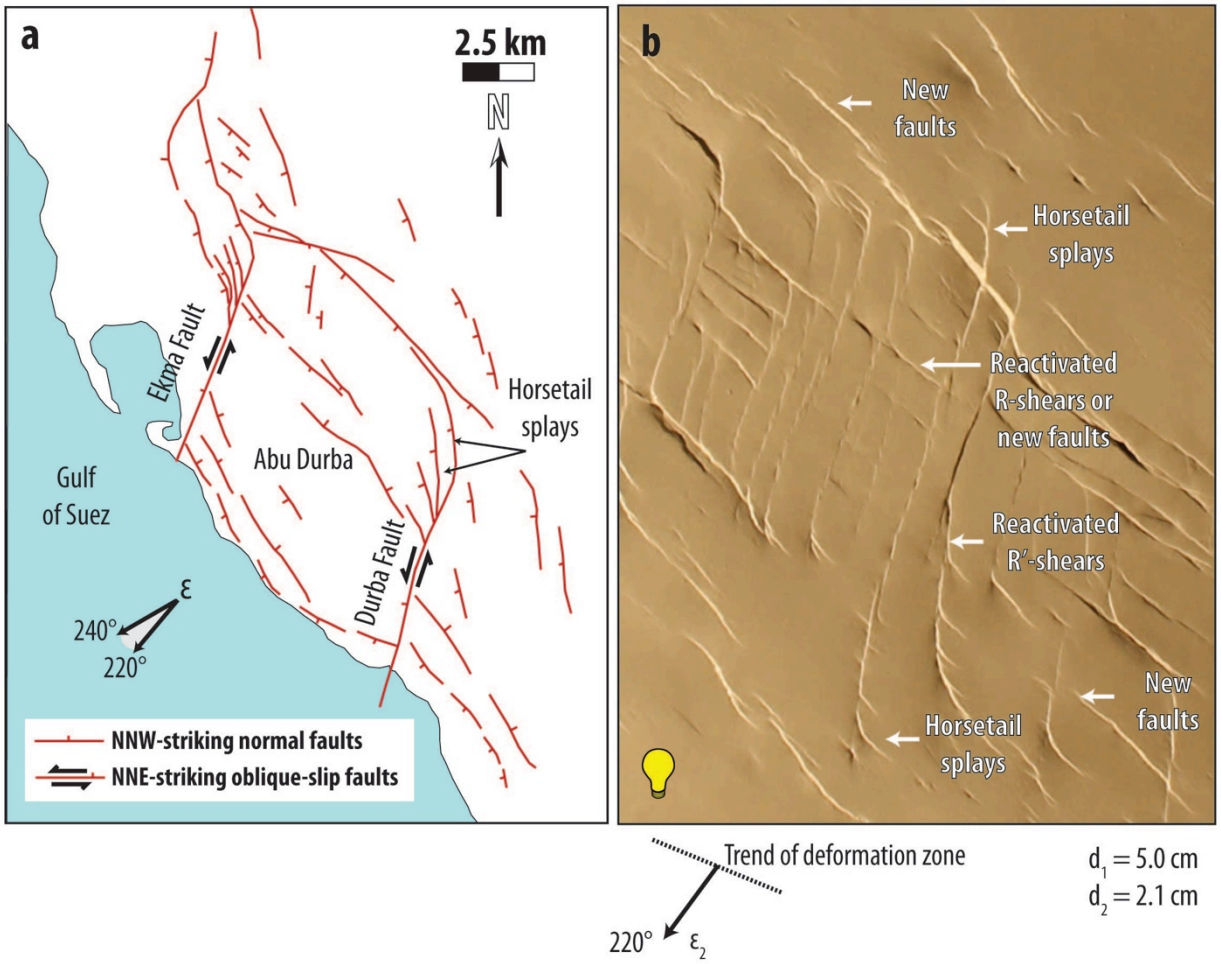

Figure 79. Fault pattern (a) from the Abu Durba area of the southern part of the Suez rift (see inset map for location) (modified from McClay and Khalil, 1998) and (b) from Model G (reoriented to match the fault orientations from the Suez rift). The reactivated pre-existing R'-shears and new normal faults in Model G, particularly at a moderate stage of development, are comparable to reactivated NNE-striking oblique-slip faults and newly formed NNW-striking normal faults in the Abu Durba area of the southern Suez rift system. Fault scarps dipping toward light appear bright; fault scarps dipping away from light appear dark.

Appendix 1. File directory

Series 1						
Model	**α_1**	**α_2**	**d_1**	**d_2**	**Date**	**File directory**
A	180°	30°	5 cm	5 cm	03/29/2012	Desktop>Modeling lab photo archive>Christian Putra>a1-180_a2-30_D1-5cm-D2-5cm
B	180°	45°	5 cm	5 cm	05/03/2012	Desktop>Modeling lab photo archive>Christian Putra>a1-180_a2-45_D1-5cm-D2-5cm
C	180°	60°	5 cm	5 cm	05/10/2012	Desktop>Modeling lab photo archive>Christian Putra>a1-180_a2-60_D1-5cm-D2-5cm
D	180°	75°	5 cm	5 cm	03/27/2012	Desktop>Modeling lab photo archive>Christian Putra>a1-180_a2-75_D1-5cm-D2-5cm
E	180°	90°	5 cm	5 cm	03/08/2012	Desktop>Modeling lab photo archive>Christian Putra>a1-180_a2-90_D1-5cm-D2-5cm
F	180°	105°	5 cm	5 cm	03/20/2012	Desktop>Modeling lab photo archive>Christian Putra>a1-180_a2-105_D1-5cm-D2-5cm
G	180°	120°	5 cm	5 cm	03/05/2012	Desktop>Modeling lab photo archive>Christian Putra>a1-180_a2-120_D1-5cm-D2-5cm
H	180°	135°	5 cm	5 cm	03/01/2012	Desktop>Modeling lab photo archive>Christian Putra>a1-180_a2-135_D1-5cm-D2-5cm
I	180°	150°	5 cm	5 cm	08/02/2012	Desktop>Modeling lab photo archive>Christian Putra>a1-180_a2-150_D1-5cm-D2-5cm
Layered	180°	90°	5 cm	2.5 cm	08/21/2012	Desktop>Modeling lab photo archive>Christian Putra>a1-180_a2-90_D1-5cm-D2-2.5cm
A1	-	30°	5 cm	5 cm	07/09/2012	Desktop>Modeling lab photo archive>Christian Putra>a-30_D-5cm
B1	-	45°	5 cm	5 cm	06/28/2012	Desktop>Modeling lab photo archive>Christian Putra>a-45_D-5cm
C1	-	60°	5 cm	5 cm	07/02/2012	Desktop>Modeling lab photo archive>Christian Putra>a-60_D-5cm
D1	-	75°	5 cm	5 cm	07/03/2012	Desktop>Modeling lab photo archive>Christian Putra>a-75_D-5cm
E1	-	90°	5 cm	5 cm	11/01/2011	Desktop>Modeling lab photo archive>Christian Putra>a-90_D-5cm
F1	-	105°	5 cm	5 cm	07/03/2012	Desktop>Modeling lab photo archive>Christian Putra>a-105_D-5cm
G1	-	120°	5 cm	5 cm	07/02/2012	Desktop>Modeling lab photo archive>Christian Putra>a-120_D-5cm
H1	-	135°	5 cm	5 cm	06/28/2012	Desktop>Modeling lab photo archive>Christian Putra>a-135_D-5cm
I1	-	150°	5 cm	5 cm	07/09/2012	Desktop>Modeling lab photo archive>Christian Putra>a-150_D-5cm

Series 2						
Model	**α_1**	**α_2**	**d_1**	**d_2**	**Date**	**File directory**
0	180°	90°	0 cm	5 cm	11/01/2011	Desktop>Modeling lab photo archive>Christian Putra>a-90_D-5cm
1	180°	90°	1 cm	5 cm	11/22/2011	Desktop>Modeling lab photo archive>Christian Putra>a1-180_a2-90_D1-1cm-D2-5cm
2	180°	90°	2 cm	5 cm	11/18/2011	Desktop>Modeling lab photo archive>Christian Putra>a1-180_a2-90_D1-2cm-D2-5cm

3	180°	90°	3 cm	5 cm	11/11/2011	Desktop>Modeling lab photo archive>Christian Putra>a1-180_a2-90_D1-3cm-D2-5cm
4	180°	90°	4 cm	5 cm	11/08/2011	Desktop>Modeling lab photo archive>Christian Putra>a1-180_a2-90_D1-4cm-D2-5cm
5	180°	90°	5 cm	5 cm	03/08/2012	Desktop>Modeling lab photo archive>Christian Putra>a1-180_a2-90_D1-5cm-D2-5cm

Appendix 2. Statistical analysis

1. Use Adobe Illustrator to fit fault segments with straight lines (as described in section 2.4)
2. Use Adobe Illustrator to export file with segments only as AutoCAD Interchangeable File (.dxf)
3. Use Ilwis software to retrieve the summed length of fault segments for every 1° increment
4. Use Excel to bin the summed length of fault segments to 5°
5. Use Stereostat to build rose diagrams for each phase of the models. Rose diagram is scaled so that the outer circle corresponds to the binned summed lengths for the model with the largest overall petal (120 cm).